High harmonics generation in solids with Berry curvature's effects

by

LÊ HỮU THÔNG

THESIS

Submitted in partial fulfillment of the requirements
for the degree of Bachelor of Science in Physics
in the University of Science, VNU-HCM

July, 2020

High harmonics generation in solids with Berry curvature's effects

by

LÊ HỮU THÔNG

THESIS

Submitted in partial fulfillment of the requirements
for the degree of Bachelor of Science in Physics
in the University of Science, VNU-HCM

Student ID: 1613189

Sub-major: Theoretical Physics

Supervisor: Dr. Huỳnh Thanh Đức - Ho Chi Minh city Institute of Physics, Vietnam Academy of Science and Technology

Dr. Nguyễn Hữu Nhã - University of Science Ho Chi Minh City

July, 2020, Ho Chi Minh City, Vietnam

Abstract

In the past ten years, high harmonics generation in solids has been under extensive study, both for its novel applications and interesting mechanism. In its theoretical models, the transition dipole's phase is believed to encompass crystals' symmetries, and to be responsible for subtle effects, albeit has rarely been addressed due to computational difficulties. This work overcomes that problem by using a parallel transport gauge of Bloch functions to acquire the complex-valued dipole, then performs a microscopic analysis to give good agreement with experiments. The method is general and can be applied to arbitrary band structures, provided the Bloch eigenvectors are known. Besides, while most of the high harmonics signal polarizes parallel to the driving laser and is dominated by odd harmonics, the component with perpendicular polarization with even harmonics prevailing is believed to originate from the crystal's Berry curvature. Recent experiments have given the conjecture based on the semiclassical theory but there is still a lack of microscopic studies, again maybe due to the dipole's phase. We perform investigations to show that Berry curvature's contribution is the origin of the below-band-gap spectrum. This suggests future experiments to utilize high harmonic signal to probe crystals' Berry curvature, which plays important roles in the field of topological matter.

Acknowledgments

To my childhood

Contents

List of Tables

List of Figures

List of Abbreviations

BZ Brillouine zone

c.c complex conjugate

C_1,C_2,... First, second,... conduction bands

EM Electromagnetism

HHG High harmonics generation

SBE Semiconductor Bloch equation

SO,LH,HH Split-off, light hole, and heavy hole bands

SVD Singular value decomposition

List of Symbols

G Reciprocal lattice vector

Ω Volume of the crystal's unit cell

R Real lattice vector

$\mathbf{a}_i, (i \in \{1, 2, 3\})$ Bravais lattice vectors

V Volume of the macroscopic crystal

$e(< 0)$ electron's charge

Chapter 1

Introduction

1.1 Background and motivation

High harmonics generation(HHG) is a phenomenon first discovered in atomic and molecular gases. When impacted with a laser field, the gaseous media can re-emit photons with energy multiple times the original laser's. In the emitted spectrum, this is represented by sharp peaks at multiples of the driving frequency, hence the name harmonics. With intense laser field strengths, comparable to the ionization level, novel non-perturbative phenomena take place. The high-order peaks have intensities comparable to the lower ones, together form a plateau that can run up to ultraviolet and soft X-rays region. This phenomenon was discovered in the 1980s and has been well studied ever since. Its applications have laid the foundation for attosecond science. [13, 27]

Recently, since 2010 [14], HHG has also been reported in bulk solids, for a wide range of materials, from large band gap insulators to graphene, caused by near-infrared and terahertz lasers.*The phenomenon opens the realization of compact ultrafast sources for coherent light in the extreme violet region, among other novel applications [13]. Although the mechanisms for HHG in solids remain a debated topic, the microscopic analysis using semiconductor Bloch equations (SBE), which give explanations based on the intraband currents and interband polarization, has been able to quantitatively describe the HHG-related phenomena in various experiments [13, 17, 24, 32]. One of the remaining challenges is the inclusion of complex-valued transition dipole when solving the SBE. The dipole's phase is believed to encompass the crystal's symmetry and is responsible for even harmonics [19]. However, due to computational difficulties, one may have access to the absolute value [32].

In the past few years, when investigating polarimetry of solid HHG, experiments have

---

*This should be differentiated with perturbative second harmonics generation in solid, which occurs in crystals with broken inversion symmetry, and is possible under weaker field strength. The phenomenon has been applied in the production of lasers for a long time and can be explained by the second-order nonlinear optical susceptibility [2, chapter 1]

reported the signal's component whose polarization is perpendicular to that of the laser [20, 22]. In this thesis it will be referred to as *transverse HHG*, to be contrasted with *ordinary HHG*, whose polarization is parallel to the driving field. While ordinary HHG is dominated by odd-order harmonics, the transverse signal is mainly composed of even-order ones. The Berry curvature of electronic Bloch states, which plays important roles in the field of topological materials, is believed to be the source for transverse HHG. Moreover, it was even proposed that HHG processes could be utilized to extract Berry curvature of materials. However, there is a lack of microscopic studies to ultimately resolve that role of Berry curvature, the reason of which may again comes from the failure to include the complex-valued transition dipole.

1.2 Methods and Main results

The main accomplishment of this thesis is applying some techniques to obtain a smooth gauge for Bloch functions, following the paper by Virk and Sipe [28]. This solves the long-standing problem of incorporating the dipole phase when describing solid HHG and related phenomena. The method is general and can be applied to arbitrary band structure, provided the Bloch eigenvectors are known.

The material chosen for study is GaAs, a typical semiconductor whose electronic and optical properties are well documented, with broken inversion symmetry available. Its band structure is calculated from the 30-band $\mathbf{k} \cdot \mathbf{p}$ method [23], which has the valid region over the full Brillouin zone and cover the range of 10 eV around the band gap (1.5 eV), enough to describe strong field excitation.

To study HHG, we solve the semiconductor Bloch equation in one-dimensional k-grid, along the laser's polarization. Then the photoexcited current is calculated by tracing the full quantum velocity operator with the density matrix. It is this electronic dynamics that emits radiation, therefore the HHG signal is evaluated as proportional to the current's spectral profile. Despite the 1D SBE, HHG signals in other directions can be studied thanks to the 3D velocity operator.

As for ordinary HHG, the results are in good agreement with experimental data reported in [30]. Further, it is demonstrated that broken inversion symmetry is responsible for even harmonics, which can only be described with the complex-valued dipole. If only dipole's amplitude is used to solve the SBE, it would result in deceptive even harmonics, which is caused by the bias towards positive values and unphysical kinks of the dipole as a function in reciprocal space.

Regarding transverse HHG, its spectrum is indeed dominated by even harmonics. The contribution originating from Berry curvature is extracted via the so-called anomalous velocity formula [31], and has predominance in the spectral region below the bandgap. It

is found that Berry curvature's effects could be enhanced by lowering excitation frequency and increasing the laser's field strength.

1.3   Thesis overview

The rest of this thesis is organized as follows. Chapter 2 presents the theoretical model for solid HHG, including semiconductor Bloch equation, 30-band $\mathbf{k} \cdot \mathbf{p}$ method, and an introduction to the concept of Berry curvature in solids. Therein, the procedure for obtaining a smooth gauge for Bloch functions is also introduced. Chapter 3 discusses our main findings and give exposition on the importance of complex-valued transition dipole as well as the effects caused by Berry curvature in HHG. Finally, chapter 4 concludes our presented results and gives prospects for future developments of the theoretical methods.

The data and figure in this thesis were calculated for the material GaAs. Three important symmetric direction of GaAs' Brillouin zone are ΓX [100], ΓK [110] and ΓL [111]. The SI unit system is used throughout, unless otherwise specified. The constant e (electron's charge) takes on the negative value.

Chapter 2

Theoretical model

2.1 The dynamical equation for HHG

2.1.1 The Hamiltonian

Using the Bloch basis[*], we are going to deal with the HHG problem by adding light-matter interaction. Under length gauge[†], the laser field in HHG experiments can be inserted to the one-electron Hamiltonian via

$$H_{1e} = \frac{\mathbf{p}^2}{2m} + U(\mathbf{r}) - e\mathbf{E} \cdot \mathbf{r}. \tag{2.1}$$

where $e < 0$ is the electron's charge and $\varepsilon_{\lambda\mathbf{k}}$ the eigenenergy obtained after diagonalizing the ground-state Hamiltonian.

To deal with the electronics system as a whole, it is useful to write the Hamiltonian in occupation number representation[‡]

$$H = \frac{\mathbf{V}}{(2\pi)^3} \sum_\lambda \int_{\text{BZ}} \varepsilon_{\lambda\mathbf{k}} a^\dagger_{\lambda\mathbf{k}} a_{\lambda\mathbf{k}} d\mathbf{k} - \frac{\mathbf{V}^2}{(2\pi)^6} e\mathbf{E}(t) \cdot \sum_{\lambda\lambda'} \int_{\text{BZ}} \mathbf{r}_{\lambda\mathbf{k}\lambda'\mathbf{k}'} a^\dagger_{\lambda\mathbf{k}} a_{\lambda'\mathbf{k}'} d\mathbf{k}d\mathbf{k}'. \tag{2.2}$$

Here we derive the position operator's representation in Bloch basis for later use, especially when dealing with light-matter interaction.

$$\mathbf{r}_{\lambda\mathbf{k}\lambda'\mathbf{k}'} = \langle\psi_{\lambda\mathbf{k}}|\,\mathbf{r}\,|\psi_{\lambda'\mathbf{k}'}\rangle = \int_{\text{all}} \psi^*_{\lambda\mathbf{k}}\mathbf{r}\psi_{\lambda'\mathbf{k}'}d\mathbf{r} = \int_{\text{all}} \mathbf{r}u^*_{\lambda\mathbf{k}}u_{\lambda'\mathbf{k}'}e^{i(\mathbf{k}'-\mathbf{k})\cdot\mathbf{r}}d\mathbf{r} \tag{2.3}$$

---

[*]See appendix A
[†]See appendix B
[‡]In occupation-number representation, the Hamiltonian is always many-particle. What differentiates it from a single particle system is the initial condition for, e.g. $\langle a^\dagger_{\lambda\mathbf{k}} a_{\lambda\mathbf{k}}\rangle$. It is also understood that the dynamics is contained in these operators, while the state is static (Heisenberg picture).

$$= \int_{\text{all}} u^*_{\lambda\mathbf{k}} u_{\lambda'\mathbf{k}'}(-i\nabla_{\mathbf{k}'})e^{i(\mathbf{k}'-\mathbf{k})\cdot\mathbf{r}}d\mathbf{r} \tag{2.4}$$

$$= -i\nabla_{\mathbf{k}'}\int_{\text{all}}\psi^*_{\lambda\mathbf{k}}\psi_{\lambda'\mathbf{k}'}d\mathbf{r} + \int_{\text{all}}u^*_{\lambda\mathbf{k}}i\nabla_{\mathbf{k}'}(u_{\lambda'\mathbf{k}'})e^{i(\mathbf{k}'-\mathbf{k})\cdot\mathbf{r}}d\mathbf{r} \tag{2.5}$$

$$= (-i\nabla_{\mathbf{k}'})\frac{(2\pi)^3\delta(\mathbf{k}'-\mathbf{k})}{\Omega}\delta_{\lambda\lambda'} + \frac{(2\pi)^3\delta(\mathbf{k}'-\mathbf{k})}{\Omega}\int_{\Omega}u^*_{\lambda\mathbf{k}}i\nabla_{\mathbf{k}'}u_{\lambda'\mathbf{k}'}d\mathbf{r} \tag{2.6}$$

$$= \frac{(2\pi)^3\delta(\mathbf{k}'-\mathbf{k})}{\Omega}\left[\delta_{\lambda\lambda'}i\nabla_{\mathbf{k}'} + \langle u_{\lambda\mathbf{k}}|i\nabla_{\mathbf{k}}u_{\lambda'\mathbf{k}}\rangle\right]. \tag{2.7}$$

Therefore,

$$\mathbf{r}_{\lambda\mathbf{k}\lambda'\mathbf{k}'} = \frac{(2\pi)^3\delta(\mathbf{k}'-\mathbf{k})}{\Omega}\left[\delta_{\lambda\lambda'}i\nabla_{\mathbf{k}'} + \boldsymbol{\xi}^{\mathbf{k}}_{\lambda\lambda'}\right] \tag{2.8}$$

with

$$\boldsymbol{\xi}^{\mathbf{k}}_{\lambda\lambda'} \equiv \langle u_{\lambda\mathbf{k}}|i\nabla_{\mathbf{k}}u_{\lambda'\mathbf{k}}\rangle = \int_{\Omega}u^*_{\lambda\mathbf{k}}i\nabla_{\mathbf{k}}u_{\lambda'\mathbf{k}}d\mathbf{r}. \tag{2.9}$$

Applying the matrix elements of $\mathbf{r}$ in equation (2.8)[*], the Hamiltonian becomes

$$H = \frac{\mathbf{V}}{(2\pi)^3}\sum_{\lambda}\int_{\text{BZ}}\varepsilon_{\lambda\mathbf{k}}a^\dagger_{\lambda\mathbf{k}}a_{\lambda\mathbf{k}}d\mathbf{k} - \frac{\mathbf{V}}{(2\pi)^3}e\mathbf{E}(t)\cdot\sum_{\lambda}\int_{\text{BZ}}a^\dagger_{\lambda\mathbf{k}}i\nabla_{\mathbf{k}}a_{\lambda\mathbf{k}}d\mathbf{k}$$
$$- \frac{\mathbf{V}}{(2\pi)^3}e\mathbf{E}(t)\cdot\sum_{\lambda\lambda'}\int_{\text{BZ}}\boldsymbol{\xi}^{\mathbf{k}}_{\lambda\lambda'}a^\dagger_{\lambda\mathbf{k}}a_{\lambda\mathbf{k}}d\mathbf{k}. \tag{2.10}$$

In the above, we have used the integral of $\mathbf{k}$ instead of the discrete sum dictated by the periodic boundary condition[†]. It is considered a good approximation when the k-grid is dense enough, or equivalently, when working with macroscopic crystals. Hereinafter, for brevity, the integral of $\mathbf{k}$ in the BZ is replaced by the corresponding discrete sum.

$$\frac{\mathbf{V}}{(2\pi)^3}\int_{\text{BZ}}d\mathbf{k} \mapsto \sum_{\mathbf{k}}^{\text{BZ}} \tag{2.11}$$

However, the notion of continuity, which becomes important when working with the functional $\delta(\mathbf{k})$, is kept implicit. The Hamiltonian then is rewritten

$$H = \sum_{\lambda\mathbf{k}}\varepsilon_{\lambda\mathbf{k}}a^\dagger_{\lambda\mathbf{k}}a_{\lambda\mathbf{k}} - e\mathbf{E}(t)\cdot\sum_{\lambda\mathbf{k}}a^\dagger_{\lambda\mathbf{k}}i\nabla_{\mathbf{k}}a_{\lambda\mathbf{k}} - e\mathbf{E}(t)\cdot\sum_{\lambda\lambda'\mathbf{k}}\boldsymbol{\xi}^{\mathbf{k}}_{\lambda\lambda'}a^\dagger_{\lambda\mathbf{k}}a_{\lambda'\mathbf{k}}. \tag{2.12}$$

It should be noted that this Hamiltonian ignores the electron-phonon scattering and the Coulomb interaction among electrons. However, for strong field excitations, these effects could later be considered phenomenologically as a dephasing term (2.22) to the dynamical equation.

---

[*]See appendix A.4 for Bloch functions' normalization convention.
[†]See appendix A.3

2.1.2 Semiconductor Bloch equation

In occupation number representation, the expectation value of a one-particle operator $\mathbf{A}$ is given by[*]

$$\langle \mathbf{A} \rangle (t) = \sum_{\lambda\lambda'\mathbf{k}\mathbf{k}'} \left\langle a^\dagger_{\lambda\mathbf{k}} a_{\lambda'\mathbf{k}'} \right\rangle (t) \mathbf{A}_{\lambda\lambda'\mathbf{k}\mathbf{k}'}. \tag{2.13}$$

Therefore, the evolution of $\left\langle a^\dagger_{\lambda\mathbf{k}} a_{\lambda\mathbf{k}} \right\rangle (t)$ tells us almost everything about the investigated phenomenon. Particularly, since the operators we are dealing with, a $\mathbf{v} \equiv \dot{\mathbf{r}}$ is diagonal w.r.t. the $\mathbf{k}$ quantum number, that sum is reduced to

$$\langle \mathbf{v} \rangle (t) = \sum_{\lambda\lambda'\mathbf{k}} \left\langle a^\dagger_{\lambda\mathbf{k}} a_{\lambda'\mathbf{k}} \right\rangle (t) \mathbf{v}^{\mathbf{k}}_{\lambda\lambda'}. \tag{2.14}$$

To determine the equation for $x^{\mathbf{k}}_{\lambda\lambda'}$, we apply the Heisenberg equation for operator dynamics [†]

$$\frac{d}{dt} a^\dagger_{\lambda\mathbf{k}} a_{\lambda'\mathbf{k}} = \frac{-i}{\hbar} \left[a^\dagger_{\lambda\mathbf{k}} a_{\lambda'\mathbf{k}}, H \right] = - (\varepsilon_{\lambda\mathbf{k}} - \varepsilon_{\lambda'\mathbf{k}}) a^\dagger_{\lambda\mathbf{k}} a_{\lambda'\mathbf{k}} - e\mathbf{E}(t) \cdot i\nabla_{\mathbf{k}} \left(a^\dagger_{\lambda\mathbf{k}} a_{\lambda'\mathbf{k}} \right)$$
$$- e\mathbf{E}(t) \cdot \sum_{\mu} \left(a^\dagger_{\lambda\mathbf{k}} a_{\mu\mathbf{k}} \boldsymbol{\xi}^{\mathbf{k}}_{\lambda'\mu} - a^\dagger_{\mu\mathbf{k}} a_{\lambda'\mathbf{k}} \boldsymbol{\xi}^{\mathbf{k}}_{\mu\lambda} \right). \tag{2.15}$$

Taking the expectation value for both sides, and let $x^{\mathbf{k}}_{\lambda\lambda'} = \left\langle a^\dagger_{\lambda\mathbf{k}} a_{\lambda'\mathbf{k}} \right\rangle$, the final equation that needs to be solved is

$$\frac{d}{dt} x^{\mathbf{k}}_{\lambda\lambda'} = \frac{i}{\hbar} (\varepsilon_{\lambda\mathbf{k}} - \varepsilon_{\lambda'\mathbf{k}}) x^{\mathbf{k}}_{\lambda\lambda'} - \frac{1}{\hbar} e\mathbf{E}(t) \cdot \nabla_{\mathbf{k}} x^{\mathbf{k}}_{\lambda\lambda'} + \frac{i}{\hbar} e\mathbf{E}(t) \cdot \sum_{\mu} \left(x^{\mathbf{k}}_{\lambda\mu} \boldsymbol{\xi}^{\mathbf{k}}_{\lambda'\mu} - x^{\mathbf{k}}_{\mu\lambda'} \boldsymbol{\xi}^{\mathbf{k}}_{\mu\lambda} \right).$$
$$\tag{2.16}$$

This equation is called the semiconductor Bloch equation (SBE)[‡], which in recent years has proven itself to be able to describe high harmonics generation in solids [17, 21, 24, 32]. The equation can be rewritten if we instead consider the one-particle density matrix[§]

$$\rho^{\mathbf{k}}_{\lambda\lambda'} = \left(x^{\mathbf{k}}_{\lambda\lambda'} \right)^*$$

$$\frac{d\rho^{\mathbf{k}}_{\lambda\lambda'}}{dt} = -\frac{i}{\hbar} (\varepsilon_{\lambda\mathbf{k}} - \varepsilon_{\lambda'\mathbf{k}}) \rho^{\mathbf{k}}_{\lambda\lambda'} - \frac{1}{\hbar} e\mathbf{E}(t) \cdot \nabla_{\mathbf{k}} \rho^{\mathbf{k}}_{\lambda\lambda'} - \frac{i}{\hbar} e\mathbf{E}(t) \cdot \left[\rho^{\mathbf{k}}, \boldsymbol{\xi}^{\mathbf{k}} \right]_{\lambda\lambda'}. \tag{2.17}$$

---

[*]See, for example, [6], equation (10.1).
[†]See appendix C for the commutation relations.
[‡]See [6], chapter 12 for a comprehensive analysis of the equation.
[§]$\rho^{\mathbf{k}}_{\lambda\lambda'}$ is called reduced density matrix, while $x^{\mathbf{k}}_{\lambda\lambda'}$ bears the name correlation function, for example as in [6].

Then, the expectation value is calculated via

$$\langle \mathbf{v} \rangle (t) = \sum_{\lambda\lambda'\mathbf{k}} x^{\mathbf{k}}_{\lambda\lambda'}(t)\mathbf{v}^{\mathbf{k}}_{\lambda\lambda'} = \sum_{\lambda\lambda'\mathbf{k}} \rho^{\mathbf{k}}_{\lambda\lambda'}(t)\mathbf{v}^{\mathbf{k}}_{\lambda'\lambda} = \sum_{\mathbf{k}} \mathrm{Tr}\{\rho^{\mathbf{k}}\mathbf{v}^{\mathbf{k}}\} = \mathrm{Tr}\{\rho\mathbf{v}\}. \qquad (2.18)$$

In matrix form, the new SBE reads

$$\frac{d\rho^{\mathbf{k}}}{dt} = -\frac{i}{\hbar}\left[H^{\mathbf{k}}, \rho^{\mathbf{k}}\right] - \frac{1}{\hbar}e\mathbf{E}(t) \cdot \nabla_{\mathbf{k}}\rho^{\mathbf{k}} - \frac{i}{\hbar}e\mathbf{E}(t) \cdot \left[\rho^{\mathbf{k}}, \boldsymbol{\xi}^{\mathbf{k}}\right] \qquad (2.19)$$

$$= -\frac{i}{\hbar}\left[H^{\mathbf{k}} - e\mathbf{E}(t) \cdot \boldsymbol{\xi}^{\mathbf{k}}, \rho^{\mathbf{k}}\right] - \frac{1}{\hbar}e\mathbf{E}(t) \cdot \nabla_{\mathbf{k}}\rho^{\mathbf{k}} \qquad (2.20)$$

$$= -\frac{i}{\hbar}\left[H^{\mathbf{k}}, \rho^{\mathbf{k}}\right] - \frac{1}{\hbar}e\mathbf{E}(t) \cdot \left\{\nabla_{\mathbf{k}}\rho^{\mathbf{k}} - i\left[\boldsymbol{\xi}^{\mathbf{k}}, \rho^{\mathbf{k}}\right]\right\}. \qquad (2.21)$$

Note: by looking through our derivation, the above SBE is correct only in a smooth gauge of Bloch functions.

Phenomenological damping

In strong field dynamics, the Coulomb and electron-phonon scattering can be describe phenomenologically by a relaxation time approximation [18]

$$\frac{\mathrm{d}\rho_{\lambda\lambda'}}{\mathrm{d}t}\bigg|_{\mathrm{scatt}} = -\frac{\rho_{\lambda\lambda'}}{T_2}, \quad \lambda \neq \lambda' \qquad (2.22)$$

For GaAs, it was suggested that T_2 is density-dependent and can take the approximation [10, 29].

$$\frac{1}{T_2} = \frac{1}{T_2^0} + \frac{1}{T_2'}n^{0.3}. \qquad (2.23)$$

where T_2^0 and T_2' represent damping caused by phonon and Coulomb interaction, respectively. T_2^0 was reported to be about 300 fs at room temperature [25], and T_2 can be lowered to the order of femtosecond under strong fields [10].

2.1.3 Electronic transport

The velocity operator is defined

$$\mathbf{v} \equiv \frac{d\mathbf{r}}{dt} = \frac{-i}{\hbar}[\mathbf{r}, H] = \frac{-i}{\hbar}[\mathbf{r}, H_0] = \mathbf{v}_0. \qquad (2.24)$$

Note that $m\mathbf{v}$ is the kinetic momentum, not the canonical one $\mathbf{p} = m\mathbf{v} + e\mathbf{A}$ (B.12). In the Bloch basis, there is a simple, direct relation between $\mathbf{v}^{\mathbf{k}}$ and $H^{\mathbf{k}}$

$$\begin{cases} H^{\mathbf{k}} & \equiv e^{-i\mathbf{k}\cdot\mathbf{r}}He^{i\mathbf{k}\cdot\mathbf{r}} \\ \mathbf{v}^{\mathbf{k}} & \equiv e^{-i\mathbf{k}\cdot\mathbf{r}}\mathbf{v}e^{i\mathbf{k}\cdot\mathbf{r}}. \end{cases} \qquad (2.25)$$

Considering $\nabla_\mathbf{k} H_\mathbf{k}$, we obtain

$$\nabla_\mathbf{k} H^\mathbf{k} = e^{-i\mathbf{k}\cdot\mathbf{r}}\left(-i\mathbf{r}H + iH\mathbf{r}\right)e^{i\mathbf{k}\cdot\mathbf{r}} = -ie^{-i\mathbf{k}\cdot\mathbf{r}}[\mathbf{r}, H]e^{i\mathbf{k}\cdot\mathbf{r}} = \hbar\mathbf{v}^\mathbf{k}. \tag{2.26}$$

Thus, all matrix elements of $\mathbf{v}^\mathbf{k}$ is known as long as an analytic expression for $H^\mathbf{k}$ is available

$$\mathbf{v}^\mathbf{k}_{\lambda\lambda'} = \frac{1}{\hbar}\langle u_{\lambda\mathbf{k}}|\left(\nabla_\mathbf{k} H^\mathbf{k}\right)|u_{\lambda'\mathbf{k}}\rangle. \tag{2.27}$$

Explicitly,

$$\begin{aligned}
\mathbf{v}^\mathbf{k}_{\lambda\lambda'} &= \frac{1}{\hbar}\langle u_{\lambda\mathbf{k}}|\left(\nabla_\mathbf{k} H^\mathbf{k}|u_{\lambda'\mathbf{k}}\rangle\right) - \frac{1}{\hbar}\langle u_{\lambda\mathbf{k}}|H^\mathbf{k}\nabla_\mathbf{k}|u_{\lambda'\mathbf{k}}\rangle \\
&= \frac{1}{\hbar}\langle u_{\lambda\mathbf{k}}|\left(\nabla_\mathbf{k}\varepsilon_{\lambda'\mathbf{k}}|u_{\lambda'\mathbf{k}}\rangle\right) - \frac{1}{\hbar}\langle u_{\lambda\mathbf{k}}|\varepsilon_{\lambda\mathbf{k}}\nabla_\mathbf{k}|u_{\lambda'\mathbf{k}}\rangle \\
&= \frac{1}{\hbar}\left(\varepsilon_{\lambda'\mathbf{k}} - \varepsilon_{\lambda\mathbf{k}}\right)\langle u_{\lambda\mathbf{k}}|\nabla_\mathbf{k}|u_{\lambda'\mathbf{k}}\rangle + \frac{1}{\hbar}\delta_{\lambda'\lambda}\nabla_\mathbf{k}\varepsilon_{\lambda'\mathbf{k}}. \tag{2.28}
\end{aligned}$$

This is again related to the quantity $\boldsymbol{\xi}^\mathbf{k}$, which appeared in the representation for $\mathbf{r}^\mathbf{k}$ [*]

$$\mathbf{v}^\mathbf{k}_{\lambda\lambda'} = \frac{-i}{\hbar}\left(\varepsilon_{\lambda'\mathbf{k}} - \varepsilon_{\lambda\mathbf{k}}\right)\boldsymbol{\xi}^\mathbf{k}_{\lambda\lambda'} + \frac{1}{\hbar}\delta_{\lambda'\lambda}\nabla_\mathbf{k}\varepsilon_{\lambda\mathbf{k}}. \tag{2.29}$$

After solving the SBE, total current density is calculated straightforwardly by taking the trace with density matrix.

$$\mathbf{j} \propto e\,\mathrm{Tr}[\mathbf{v}\rho] = e\sum_\lambda(\mathbf{v}^\mathbf{k}\rho^\mathbf{k})_{\lambda\lambda} = e\sum_{\lambda\lambda'}\mathbf{v}^\mathbf{k}_{\lambda\lambda'}\rho^\mathbf{k}_{\lambda'\lambda}. \tag{2.30}$$

Within ultrafast processes in quantum optics, the electric current oscillates rapidly and emits radiation, whose intensity is measured in HHG experiments. That signal is usually the reflected one (in contrast to transmitted signal) in order to avoid propagation effects when the radiation passes through the bulk solid. HHG intensity is calculated via with the assumption that some kind of current sheet is the source for reflected HHG. While an oscillating point charge's radiation is proportional to its acceleration, that of a current sheet is proportional to the current itself [†]

$$I_{\mathrm{HHG}}(\omega) \propto |\mathbf{j}(\omega)|^2. \tag{2.31}$$

---

[*]By derivation, this relation is correct only in a smooth gauge for Bloch functions, in the same way as the SBE.

[†][See 5, chapter 11.]. This formula is also widely used in the literature [17, 21, 24].

2.2 The 30-band $\mathbf{k} \cdot \mathbf{p}$ method

To be able to solve the SBE describing HHG for particular material, we need the following information

- The band energy $\varepsilon_{\lambda \mathbf{k}}$

- The quantity $\boldsymbol{\xi}_{\lambda \lambda'}^{\mathbf{k}} = \langle u_{\lambda \mathbf{k}} | i \nabla_{\mathbf{k}} u_{\lambda' \mathbf{k}} \rangle$, which appeared in the representation of $\mathbf{r}$ (2.8)

- The velocity operator $\mathbf{v}^{\mathbf{k}} = \dfrac{1}{\hbar} \nabla_{\mathbf{k}} H^{\mathbf{k}}$ to calculate the electric current and HHG signal, which could also be obtained via $\varepsilon_{\lambda \mathbf{k}}$ and $\boldsymbol{\xi}^{\mathbf{k}}$ by (2.29).
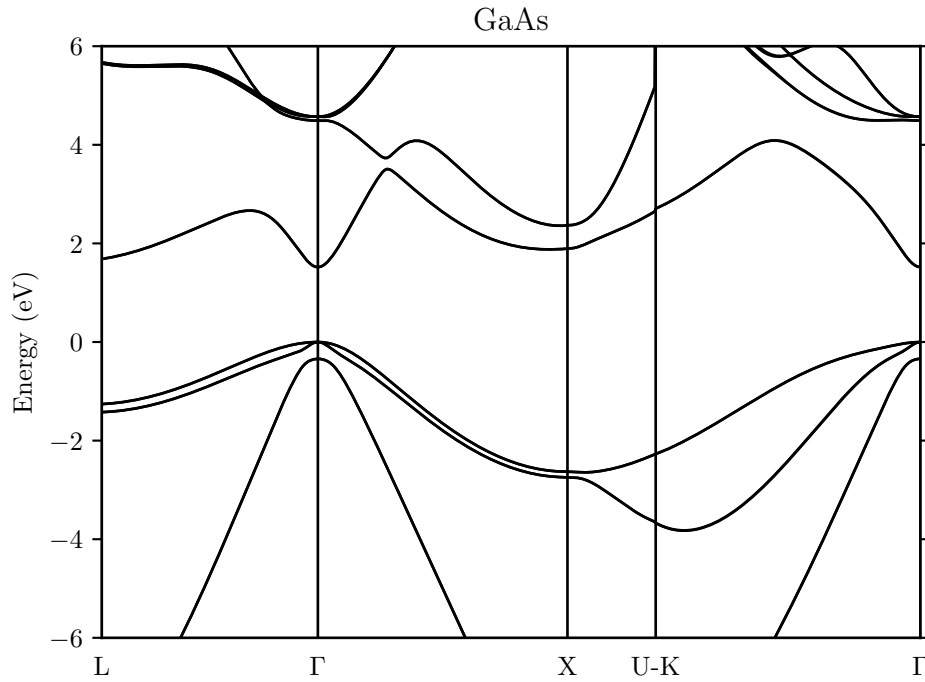
Figure 2.1: Band structure of GaAs at $T = 0K$, using 30-band $\mathbf{k} \cdot \mathbf{p}$ method. The parameters are listed in table D.1.

While the energy $\varepsilon_{\lambda \mathbf{k}}$ is provided by any kind of band structure calculation[*], the important $\boldsymbol{\xi}^{\mathbf{k}}$ and $\mathbf{v}^{\mathbf{k}}$ have to be calculated from an analytic expression of $H^{\mathbf{k}}$ or though special techniques where such an expression is unavailable, one of which is presented in section 2.3. The 30-band $\mathbf{k} \cdot \mathbf{p}$ method, devised by Guy Fishman's group [23], serves well for our purposes. Some of its characteristics are

- It is a non-perturbative $\mathbf{k} \cdot \mathbf{p}$ method, describing bands till the BZ boundary.

- An analytic expression for $H^{\mathbf{k}}$ is provided.

- It is suitable for zinc-blende type crystal, e.g. Si, Ge, GaAs.

---

[*]For a general overview on band structure calculation, see [9], chapter 2.

- It needs about 10 adjustable parameters.

- The valid region is large enough to cover strong field excitation in HHG: 5 eV above and 6 eV under the top of the valence band.

- Spin-orbit coupling is taken into account.

- The basis states are fairly complete, with no resort to remote bands.

2.2.1 The Hamiltonian

To describe electrons in crystals, we use this one-particle Hamiltonian taking into account spin-orbit interaction:

$$H = \frac{\mathbf{p}^2}{2m} + V(\mathbf{r}) + \frac{\hbar}{4m^2c^2}(\nabla V \times \mathbf{p}) \cdot \sigma \quad \text{(Gaussian unit)}. \tag{2.32}$$

$$H_{\mathbf{k}} = e^{-i\mathbf{kr}}He^{i\mathbf{kr}} = H_{\mathbf{k}=0} + \frac{\hbar^2k^2}{2m} + \frac{\hbar}{m}\mathbf{k}\cdot\mathbf{p} + \frac{\hbar^2}{4m^2c^2}(\nabla V \times \mathbf{k}) \cdot \boldsymbol{\sigma}$$

$$\approx H_{\mathbf{k}=0} + \frac{\hbar^2k^2}{2m} + \frac{\hbar}{m}\mathbf{k}\cdot\mathbf{p}. \tag{2.33}$$

where the $\mathbf{k}$-dependent spin-orbit term $\dfrac{\hbar^2}{4m^2c^2}(\nabla V \times \mathbf{k}) \cdot \sigma$ has been ignored relatively to $\dfrac{\hbar^2}{4m^2c^2}(\nabla V \times \mathbf{p}) \cdot \sigma$, since $\hbar\mathbf{k}$ is usually much smaller than the maximum matrix element of $\mathbf{p}$. The Pauli matrices acting on the spin degrees of freedom are given by

$$\boldsymbol{\sigma} = \langle \sigma_x, \sigma_y, \sigma_z \rangle, \quad \sigma_x = \begin{bmatrix} 0 & 1 \\ 1 & 0 \end{bmatrix}, \sigma_y = \begin{bmatrix} 0 & -i \\ i & 0 \end{bmatrix}, \sigma_z = \begin{bmatrix} 1 & 0 \\ 0 & -1 \end{bmatrix}. \tag{2.34}$$

2.2.2 The basis states

Finding the band structure of a material involves calculating the eigenvalues $\varepsilon_{\lambda\mathbf{k}}$ and eigenstates $|u_{\lambda\mathbf{k}}\rangle$ of $H^{\mathbf{k}}$ in the first Brillouin zone of the lattice's reciprocal space. Even though $H^{\mathbf{k}}$ has an infinite number of eigenlevels, in practical calculation, we first need to select a finite basis of states, usually near the band gap region, then represent $H_{\mathbf{k}}$ and $|u_{\lambda\mathbf{k}}\rangle$ as a matrix and vectors in that basis' space. The 30×30 $\mathbf{k} \cdot \mathbf{p}$ Hamiltonian [23] uses 30 states based on the those of the 15×15 $\mathbf{k} \cdot \mathbf{p}$ Hamiltonian in table 2.1.

After including spin effects, the number of states doubles (table 2.2). This new set of basis states are formed by coupling the spinless state with the spinor representation of

Table 2.1: The basis states in the 15×15 $\mathbf{k} \cdot \mathbf{p}$ Hamiltonian (without spin) [12]. The $^+$ and $^-$ signs respectively indicate bonding and anti-bonding atomic states.

T_d group's notation	Wave vector	Atomic property	Basis states
Γ_{1q}	[200]	s^-	$\lvert S_q \rangle$
Γ_{5d}	[200]	d^+	$\lvert X_d \rangle, \lvert Y_d \rangle, \lvert Z_d \rangle$
Γ_3	[200]	d^-	$\lvert D_x \rangle, \lvert D_z \rangle$
Γ_{1u}	[111]	s^+	$\lvert S_u \rangle$
Γ_{5c}	[111]	p^-	$\lvert X_c \rangle, \lvert Y_c \rangle, \lvert Z_c \rangle$
Γ_1	[111]	s^-	$\lvert S \rangle$
Γ_5	[111]	p^+	$\lvert X \rangle, \lvert Y \rangle, \lvert Z \rangle$
Γ_{1v}	[000]	s^+	$\lvert S_v \rangle$

one-half spin. The states $\lvert S_i \rangle$ and $\lvert D_i \rangle$ are constructed trivially, e.g.

$$
\begin{cases}
\lvert S_q \uparrow \rangle & \equiv \lvert S_q \rangle \otimes \lvert \uparrow \rangle = \begin{bmatrix} \lvert S_q \rangle \\ 0 \end{bmatrix} \\[2ex]
\lvert S_q \downarrow \rangle & \equiv \lvert S_q \rangle \otimes \lvert \uparrow \rangle = \begin{bmatrix} 0 \\ \lvert S_q \rangle \end{bmatrix}.
\end{cases}
\tag{2.35}
$$

The triplets $\{\lvert X_i \rangle, \lvert Y_i \rangle, \lvert Z_i \rangle\}$ are constructed in the same way as finding the eigenstate of total angular momemtum $\mathbf{J} = \mathbf{L} + \mathbf{S}$ for electrons with angular momentum $l = 1$. For example, we first define

$$
\begin{cases}
\lvert 1, 1 \rangle & = \dfrac{-i}{\sqrt{2}} \left(\lvert X \rangle + i \lvert Y \rangle \right) \\[1ex]
\lvert 1, 0 \rangle & = i \lvert Z \rangle \\[1ex]
\lvert 1, -1 \rangle & = \dfrac{i}{\sqrt{2}} \left(\lvert X \rangle - i \lvert Y \rangle \right),
\end{cases}
\tag{2.36}
$$

then,

$$
\begin{cases}
\lvert v'_{1/2} \rangle & = \left\lvert \dfrac{1}{2}, \dfrac{1}{2} \right\rangle = \sqrt{\dfrac{1}{3}} \lvert 1, 0 \rangle \otimes \lvert \uparrow \rangle - \sqrt{\dfrac{2}{3}} \lvert 1, 1 \rangle \otimes \lvert \downarrow \rangle = \begin{bmatrix} \sqrt{\frac{1}{3}} i \lvert Z \rangle \\ \frac{i}{\sqrt{3}} \left(\lvert X \rangle + i \lvert Y \rangle \right) \end{bmatrix} \\[3ex]
\lvert v'_{-1/2} \rangle & = \left\lvert \dfrac{1}{2}, \dfrac{-1}{2} \right\rangle = \sqrt{\dfrac{2}{3}} \lvert 1, -1 \rangle \otimes \lvert \uparrow \rangle - \sqrt{\dfrac{1}{3}} \lvert 1, 0 \rangle \otimes \lvert \downarrow \rangle = \begin{bmatrix} \frac{i}{\sqrt{3}} \left(\lvert X \rangle - i \lvert Y \rangle \right) \\ -\sqrt{\frac{1}{3}} i \lvert Z \rangle \end{bmatrix}
\end{cases}
$$

and

$$
\begin{cases}
\left|v_{3/2}\right\rangle &= \left|\dfrac{3}{2},\dfrac{3}{2}\right\rangle = |1,1\rangle \otimes |\uparrow\rangle = \begin{bmatrix} \frac{-i}{\sqrt{2}}\left(|X\rangle + i\,|Y\rangle\right) \\ 0 \end{bmatrix} \\[2em]
\left|v_{1/2}\right\rangle &= \left|\dfrac{3}{2},\dfrac{1}{2}\right\rangle = \sqrt{\dfrac{2}{3}}\,|1,0\rangle \otimes |\uparrow\rangle + \sqrt{\dfrac{1}{3}}\,|1,1\rangle \otimes |\downarrow\rangle = \begin{bmatrix} \sqrt{\frac{2}{3}}\,i\,|Z\rangle \\ \frac{-i}{\sqrt{6}}\left(|X\rangle + i\,|Y\rangle\right) \end{bmatrix} \\[2em]
\left|v_{-1/2}\right\rangle &= \left|\dfrac{3}{2},\dfrac{-1}{2}\right\rangle = \sqrt{\dfrac{1}{3}}\,|1,-1\rangle \otimes |\uparrow\rangle + \sqrt{\dfrac{2}{3}}\,|1,0\rangle \otimes |\downarrow\rangle = \begin{bmatrix} \frac{i}{\sqrt{6}}\left(|X\rangle - i\,|Y\rangle\right) \\ \sqrt{\frac{2}{3}}\,i\,|Z\rangle \end{bmatrix} \\[2em]
\left|v_{-3/2}\right\rangle &= \left|\dfrac{3}{2},\dfrac{-3}{2}\right\rangle = |1,-1\rangle \otimes |\downarrow\rangle = \begin{bmatrix} 0 \\ \frac{i}{\sqrt{2}}\left(|X\rangle - i\,|Y\rangle\right) \end{bmatrix}.
\end{cases}
$$

Table 2.2: The basis states in 30-band $\mathbf{k}\cdot\mathbf{p}$ Hamiltonian [23].

15 $\mathbf{k}\cdot\mathbf{p}$ states	30 $\mathbf{k}\cdot\mathbf{p}$ states	Double group	$E_\Gamma = \langle u|\, H_\Gamma \,|u\rangle$
$|S_q\rangle$	$|S_q \uparrow\rangle, |S_q \downarrow\rangle$	Γ_{6q}	E_q
$|X_d\rangle, |Y_d\rangle, |Z_d\rangle$	$\left|d_{3/2}\right\rangle, \left|d_{1/2}\right\rangle, \left|d_{-1/2}\right\rangle, \left|d_{-3/2}\right\rangle$	Γ_{8d}	$E_{8d} = E_{5d} + \Delta_d/3$
	$\left|d'_{1/2}\right\rangle, \left|d'_{-1/2}\right\rangle$	Γ_{7d}	$E_{7d} = E_{5d} - 2\Delta_d/3$
$|D_x\rangle, |D_z\rangle$	$|D_x \uparrow\rangle, |D_x \downarrow\rangle$ $|D_z \uparrow\rangle, |D_z \downarrow\rangle$	Γ_{8-3}	E_{3d}
$|S_u\rangle$	$|S_u \uparrow\rangle, |S_u \downarrow\rangle$	Γ_{6u}	E_{6u}
$|X_c\rangle, |Y_c\rangle, |Z_c\rangle$	$\left|c_{3/2}\right\rangle, \left|c_{1/2}\right\rangle, \left|c_{-1/2}\right\rangle, \left|c_{-3/2}\right\rangle$	Γ_{8c}	$E_{8c} = E_{5c} + \Delta_c/3$
	$\left|c'_{1/2}\right\rangle, \left|c'_{-1/2}\right\rangle$	Γ_{7c}	$E_{7c} = E_{5c} - 2\Delta_c/3$
$|S\rangle$	$|S \uparrow\rangle, |S \downarrow\rangle$	Γ_{6c}	E_{6c}
$|X\rangle, |Y\rangle, |Z\rangle$	$\left|v_{3/2}\right\rangle, \left|v_{1/2}\right\rangle, \left|v_{-1/2}\right\rangle, \left|v_{-3/2}\right\rangle$	Γ_{8v}	$E_{8v} = E_{5v} + \Delta/3$
	$\left|v'_{1/2}\right\rangle, \left|v'_{-1/2}\right\rangle$	Γ_{7v}	$E_{7v} = E_{5v} - 2\Delta/3$
$|S_v\rangle$	$|S_v \uparrow\rangle, |S_v \downarrow\rangle$	Γ_{6v}	E_{6v}

2.2.3 Momentum matrix elements as parameters

After specifying the basis, the next thing to do is finding the explicit matrix form of $H_{\mathbf{k}}$. Since $H_{\mathbf{k}} \approx H_{\mathbf{k}=0} + \dfrac{\hbar^2 k^2}{2m} + \dfrac{\hbar}{m}\mathbf{k}\cdot\mathbf{p}$ and $H_{\mathbf{k}=0}$ is almost known, it is crucial to find the matrix elements of $\mathbf{p}$ and $\nabla V \times \mathbf{p}$. These matrix elements become adjustable parameters in the 30-band $\mathbf{k}\cdot\mathbf{p}$ model.

The basis chosen almost diagonalizes $H_{\mathbf{k}=0}$, except for some off-diagonal elements caused spin-orbit coupling among different Γ_5 levels or between Γ_5 and Γ_3 levels, e.g., $\langle \Gamma_3 |\, \frac{\hbar}{4m^2c^2}(\nabla V \times \mathbf{p}) \cdot \sigma \,| \Gamma_{5d}\rangle \neq 0$. The energy of these states are mostly taken from experiments. Otherwise, they are estimated using pseudopotential method, as suggested by [12]. The independent spin-orbit matrix elements that contribute to $H_{\mathbf{k}=0}$ are specified

below

$$\Delta = \frac{3\hbar}{4m^2c^2} \langle X | \left(\nabla V \times \mathbf{p} \right)_z | iY \rangle, \quad \Delta' = \frac{3\hbar}{4m^2c^2} \langle X_c | \left(\nabla V \times \mathbf{p} \right)_z | iY \rangle,$$

$$\Delta_c = \frac{3\hbar}{4m^2c^2} \langle X_c | \left(\nabla V \times \mathbf{p} \right)_z | iY_c \rangle, \quad \Delta'_{dc} = \frac{3\hbar}{4m^2c^2} \langle X_c | \left(\nabla V \times \mathbf{p} \right)_z | iY_c \rangle,$$

$$\Delta_d = \frac{3\hbar}{4m^2c^2} \langle X_d | \left(\nabla V \times \mathbf{p} \right)_z | iY_d \rangle, \quad \Delta'_{3d} = \frac{\hbar}{4\sqrt{2}m^2c^2} \langle D_z | \left(\nabla V \times \mathbf{p} \right)_x | iX_d \rangle,$$

$$\Delta_{dZ} = \frac{3\hbar}{4m^2c^2} \langle Y_d | \left(\nabla V \times \mathbf{p} \right)_x | iZ \rangle, \quad \Delta'_{3X} = \frac{\hbar}{4\sqrt{2}m^2c^2} \langle D_z | \left(\nabla V \times \mathbf{p} \right)_x | iX \rangle,$$

$$\Delta_{3c} = \frac{\hbar}{4\sqrt{2}m^2c^2} \langle D_z | \left(\nabla V \times \mathbf{p} \right)_x | iX_c \rangle.$$

Note that the 3 parameters $\Delta, \Delta_c, \Delta_d$ have been absorbed into the energy levels at Γ.

Due to the parity of $\mathbf{p}$ and the basis states, most of $\mathbf{p}$'s matrix-elements are null or related to one another. For example, $\langle S_q | p_x | iX_d \rangle = \langle S_q | p_y | iY_d \rangle = \langle S_q | p_z | iZ_d \rangle$, while $\langle S_q | p_x | iY_d \rangle = 0$. The original paper specified that $|X\rangle, |Y\rangle, |Z\rangle$ are chosen to transform like yz, zx, xy under spacial symmetry operations, while $|D_z\rangle, |D_x\rangle$ like $\sqrt{3}(y^2 - z^2), 3x^2 - r^2$. The non-zero, independent elements are listed below, where the i is inserted to make the parameters real.

$$P_{qd} = \frac{\hbar}{m} \langle S_q | p_x | iX_d \rangle, \quad P_{qX} = \frac{\hbar}{m} \langle S_q | p_x | iX \rangle, \quad P'_{qc} = \frac{\hbar}{m} \langle S_q | p_x | iX_c \rangle$$

$$P_{dc} = \frac{\hbar}{m} \langle X_d | p_y | iZ_c \rangle, \quad P'_{uX} = \frac{\hbar}{m} \langle S_u | p_x | iX \rangle, \quad P'_{dZ} = \frac{\hbar}{m} \langle X_d | p_y | iZ \rangle,$$

$$P_{uc} = \frac{\hbar}{m} \langle S_u | p_x | iX_c \rangle, \quad P'_{ud} = \frac{\hbar}{m} \langle S_u | p_x | iX_d \rangle$$

$$P_{3d} = \frac{\hbar}{m} \langle D_z | p_x | iX_d \rangle, \quad P_{3X} = \frac{\hbar}{m} \langle D_z | p_x | iX \rangle, \quad P'_{3c} = \frac{\hbar}{m} \langle D_z | p_x | iX_c \rangle,$$

$$P_{vc} = \frac{\hbar}{m} \langle S_v | p_x | iX_c \rangle, \quad P'_{vd} = \frac{\hbar}{m} \langle S_v | p_x | iX_d \rangle, \quad P'_{vX} = \frac{\hbar}{m} \langle S_v | p_x | iX \rangle,$$

$$P_X = \frac{\hbar}{m} \langle X_c | p_y | iZ_c \rangle,$$

$$P = \frac{\hbar}{m} \langle S | p_x | iX \rangle, \quad P_{sd} = \frac{\hbar}{m} \langle S | p_x | iX_d \rangle, \quad P' = \frac{\hbar}{m} \langle S | p_x | iX_c \rangle.$$

All in all, the structure of $\mathbf{k} \cdot \mathbf{p}$ 30 Hamiltonian with all coupling parameters is summarized in table 2.3.

Equipped with all necessary matrix elements, the explicit form of $H^{\mathbf{k}}$ is obtained straightforwardly. For example

$$\langle S_q \uparrow | H^{\mathbf{k}} | d_{3/2} \rangle = \begin{bmatrix} |S_q\rangle \\ 0 \end{bmatrix}^\dagger \left(H_{\mathbf{k}=0} + \frac{\hbar^2 k^2}{2m} + \frac{\hbar}{m} \mathbf{k} \cdot \mathbf{p} \right) \begin{bmatrix} \frac{-i}{\sqrt{2}} \left(|X\rangle + i |Y\rangle \right) \\ 0 \end{bmatrix}$$

$$= \frac{-i}{\sqrt{2}} \frac{\hbar}{m} \mathbf{k} \cdot \left(\langle S_q | \mathbf{p} | X \rangle + i \langle S_q | \mathbf{p} | Y \rangle \right)$$

$$= \frac{-1}{\sqrt{2}} \mathbf{k} \cdot \left(P_{qd} \hat{\mathbf{x}} + i P_{qd} \hat{\mathbf{y}} \right)$$

Table 2.3: Structure of the 30-band $\mathbf{k}\cdot\mathbf{p}$ Hamiltonian

	$\lvert S_q\rangle$	$\lvert XYZ_d\rangle$	$\lvert D_{x,z}\rangle$	$\lvert S_u\rangle$	$\lvert XYZ_c\rangle$	$\lvert S\rangle$	$\lvert XYZ\rangle$	$\lvert S_v\rangle$
$\langle S_q\rvert$	E_{6q}	P_{qd}	0	0	P'_{qc}	0	P_{qX}	0
$\langle XYZ_d\rvert$		$E_{8d,7d}$	P_{3d},Δ'_{3d}	P'_{ud}	P'_{dc},Δ'_{dc}	P_{sd}	P_{dZ},Δ_{dZ}	P'_{vd}
$\langle D_{x,z}\rvert$			E_3	0	P'_{3c},Δ'_{3c}	0	P_{3X},Δ_{3X}	0
$\langle S_u\rvert$				E_u	P_{uc}	0	P'_{uX}	0
$\langle XYZ_c\rvert$					$E_{8c,7c}$	P'	P_X,Δ'	P_{vc}
$\langle S\rvert$			c.c.			E_{6c}	P	0
$\langle XYZ\rvert$							$E_{8v,7v}$	P'_{vX}
$\langle S_v\rvert$								E_{6c}

$$=\frac{-1}{\sqrt{2}}P_{qd}\left(k_x+ik_y\right)\equiv\frac{-1}{\sqrt{2}}P_{qd}^+. \tag{2.37}$$

All matrix elements can also be found in the book (in French) by Guy Fishnman [3]. The appendix D serves as a quick reference, wherein the matrix $H^{\mathbf{k}}$ is tabulated.

2.3 A continuous gauge for Bloch functions

Under length gauge, the SBE equation (2.17) involves a derivative term in k-space, which necessitates the use of a smooth gauge for Bloch functions $\lvert u_{\lambda\mathbf{k}}\rangle$. However, in traditional band structure calculation, numerical diagonalization results in Bloch states with random phases and subspace mixing. For that reason, as a prerequisite step, we need to apply some techniques to make the dipole $\boldsymbol{\xi}^{\mathbf{k}}_{\lambda\lambda'}$ smooth.*The simplest remedy is just ignoring the phase and only using the averaged absolute value $\left\lvert\boldsymbol{\xi}^{\mathbf{k}}_{\lambda\lambda'}\right\rvert$.

However, the information contained in the dipole's phase is believed to be crucial for describing even harmonics caused by crystal's broken inversion symmetry [19]. The main accomplishment of this thesis is using special techniques to obtain a smooth gauge for Bloch functions, following the paper by Virk and Sipe [28]. A simpler exposition for the method could also be found in [8, section 3.6].

---

*Although the *dipole* may be defined by $\mathbf{d}=e\mathbf{r}$, this thesis also uses that term for $\boldsymbol{\xi}^{\mathbf{k}}_{\lambda\lambda'}$ for its resemblance and significance. The word *transition dipole* is also used interchangeably.

2.3.1 Averaging the dipole

Suppose we are calculating the inter-block matrix element for an operator d between 2 subspaces $\{|1\rangle, |2\rangle\}$ and $\{|3\rangle, |4\rangle\}$, while all the states $|1\rangle, |2\rangle, |3\rangle, |4\rangle$ are subjected to random phases and subspace mixing. The basic idea is that each subspace is still invariant, so we consider the matrix elements between subspaces instead of states. As an example, the projection of the vector $\hat{d}|1\rangle$ onto $\{|3\rangle, |4\rangle\}$

$$|3,4\rangle\langle 3,4|\,\hat{d}\,|1\rangle = (|3\rangle\langle 3| + |4\rangle\langle 4|)\,\hat{d}\,|1\rangle = (d_{31}|3\rangle + d_{41}|4\rangle) \tag{2.38}$$

has the exact magnitude $d_{1,34} = \sqrt{|d_{13}|^2 + |d_{14}|^2}$ regardless of how $|3\rangle$ and $|4\rangle$ was chosen. Similarly $d_{2,34} = \sqrt{|d_{23}|^2 + |d_{24}|^2}$. With that motivation, we propose the averaging formula for the operator d at each k-point

$$\bar{d}_{1,3} = \dots = \bar{d}_{2,4} \equiv d_{12,34} = \frac{1}{2}\sqrt{|d_{13}|^2 + |d_{14}|^2 + |d_{23}|^2 + |d_{24}|^2}. \tag{2.39}$$

This formula works best if the operator $\hat{d}$ cannot probe the source of degeneracy, e.g. in
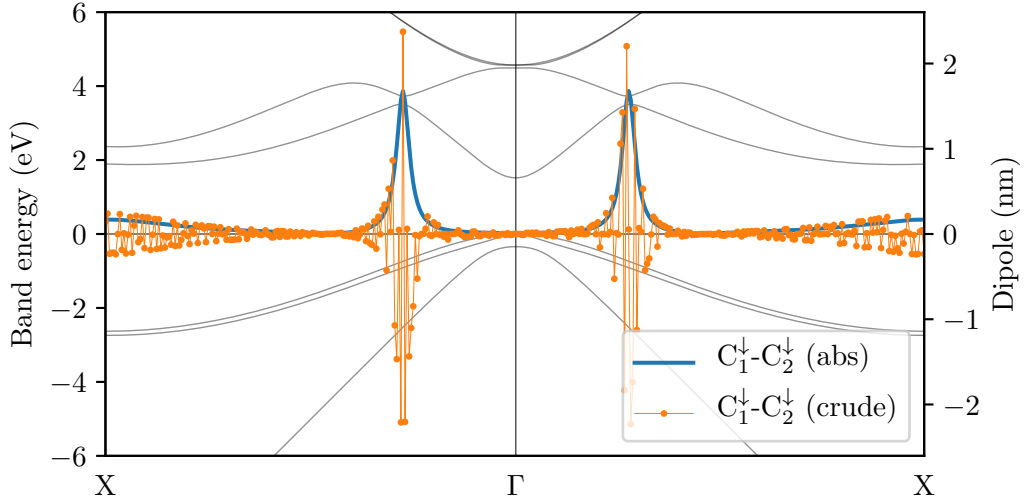
Figure 2.2: The average magnitude of interblock dipole between C1 and C2 bands, compared with results calculated directly after numerical diagonalization. ($\boldsymbol{\xi}^{\mathbf{k}}_{\lambda\lambda'}$ is purely imaginary in this direction.)

the case of spin-dengereracy and the position operator. Interestingly, in such cases, $d_{1,34}$ and $d_{2,34}$ is the same, that is, each state in the space $\{|1\rangle, |2\rangle\}$ has the same charateristics w.r.t. the operator $\hat{d}$.

The newly obtained transition dipole is shown in figure 2.2, which is smooth enough to solve the SBE. However, it can seen that taking the amplitude sometimes results in unphysical kinks, when the function reaches zero.*This can be improved by attaching suitable sign to the dipole when its derivative w.r.t. $\mathbf{k}$ jumps over a certain threshold. Another drawback is the bias toward positive values, while we have no sensible criteria to

attach the minus sign. These effects will be discussed in our results.

2.3.2 The parallel transport gauge

The general method for obtaining a smooth gauge for Blochs functions is presented in the work by Virk and Sipe (2007) [28]. The gauge obtained is called a parallel transport gauge, in which the Berry connection[*] $\boldsymbol{\xi}_{\lambda\lambda}^{\mathbf{k}}$ vanishes.[†] Here we just summarize the main procedures performed in the method. The result of this method, subordinated by the SVD procedure presented below, is illustrated in figure 2.3.
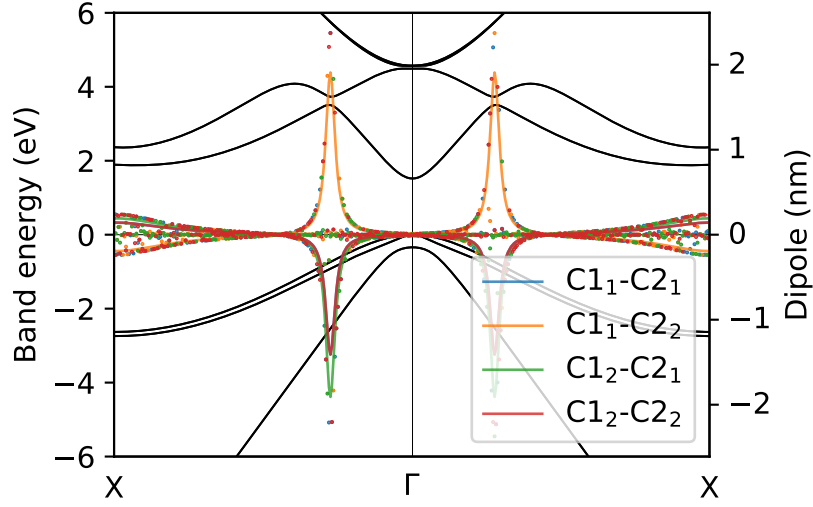
Figure 2.3: The transition dipole (imaginary part) in a parallel transport gauge.

To transform the Bloch functions between gauges, all we need to do is applying a unitary rotation among the states. In our case, such an operation has to counter-balance the effects caused by numerical diagonalization. The ultimate transformation would have the form

$$\boldsymbol{\xi}^{\mathbf{k}} = W^{\mathbf{k}_0,\mathbf{k}} \tilde{\boldsymbol{\xi}}^{\mathbf{k}} (W^{\mathbf{k}_0,\mathbf{k}})^\dagger \qquad (2.40)$$

where $W^{\mathbf{k}_0,\mathbf{k}}$ is what we need to construct. In the above formula, $\mathbf{k}_0$ is the pivot point, with which Bloch functions at all other k-points will be aligned. Usually, $\mathbf{k}_0$ is chosen to lie at the BZ's boundary.

Let us define the overlap matrix between the Bloch states at two adjacent k-points

$$S_{\lambda'\lambda}^{\mathbf{k},\mathbf{k}+\Delta\mathbf{k}} \equiv \left\langle \tilde{u}_{\lambda'}^{\mathbf{k}} \middle| \tilde{u}_{\lambda}^{\mathbf{k}+\Delta\mathbf{k}} \right\rangle \qquad (2.41)$$

whose intrablock[‡] part is named $g^{\mathbf{k},\mathbf{k}+\Delta\mathbf{k}}$. It is this portion of $S^{\mathbf{k},\mathbf{k}+\Delta\mathbf{k}}$ that constructs

---

[*]Compare the results in figure 2.2 and 2.3
[*]See section 2.4.2 for the definition of Berry connection.
[†]See, for example [8], chapter 3.

$W^{\mathbf{k}_0, \mathbf{k}}$

$$W^{\mathbf{k}_0, \mathbf{k}} = g^{\mathbf{k}_0, \mathbf{k}_0 + \Delta \mathbf{k}} ... g^{\mathbf{k} - \Delta \mathbf{k}, \mathbf{k}}. \tag{2.42}$$

Singular value decomposition

Singular value decomposition[*](SVD) take its origin from the fact that any rectangular matrix S can be decomposed into

$$S = U \Sigma V^\dagger, \tag{2.43}$$

where U and V are unitary matrices, while Σ is a diagonal matrix with real, positive elements (so-called singular values). The deviations of these singular values from unity indicate how far the matrix S is from unitarity. To unitarize a matrix, one may exclude the singular values (if they are close to 1) to get the approximation $S \approx UV^\dagger$.

In formula (2.42) since $W^{\mathbf{k}_0, \mathbf{k}}$ is constructed by multiplying a sequence of $S_{\text{intra}}^{\mathbf{k}, \mathbf{k} + \Delta \mathbf{k}}$, the first few k-points on the aligned k-line are still unitary at order $\mathcal{O}(\Delta k)$, while the last at order $\mathcal{O}(1)$ due to errors building up. This would cause false asymmetries in our band structure (figure 2.4). Therefore, we need to apply SVD to $W^{\mathbf{k}_0, \mathbf{k}}$.
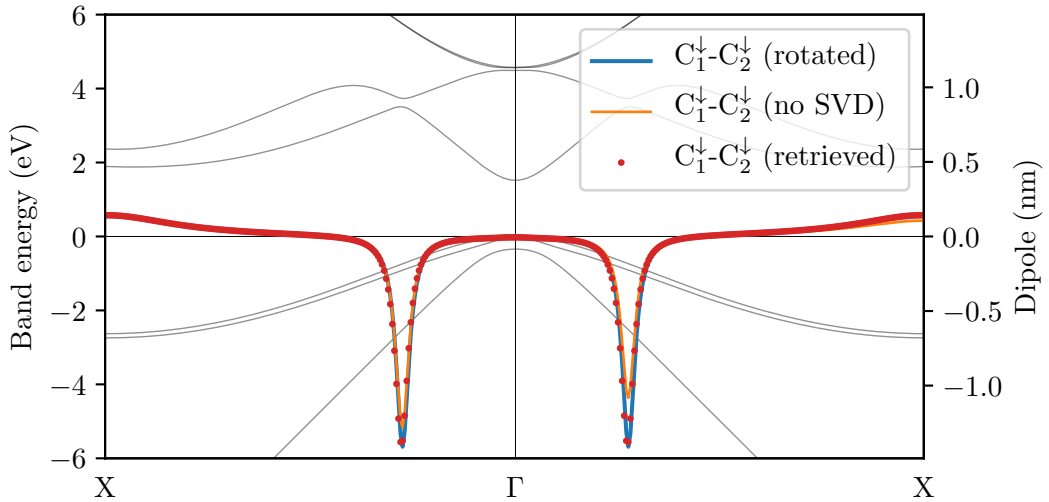
Figure 2.4: The dipole matrix element (imaginary part) between the first two conduction bands, using a grid of 400 k-points with the pivot at the left boundary. The first two lines uses the formula (2.40), with and without the SVD procedure. The *retrieved* result is calculated from formula (2.45), showing that the dipole $\boldsymbol{\xi}_{\lambda \lambda'}^{\mathbf{k}}$ can be retrieved with high precision.

[‡]A block of bands is defined to have no degeneracy point with another block. For example the four bands of light hole and heavy hole (including spin) is such a block.

[*]A nice and brief overview on the technique can be found in [8, appendix B]

2.3.3 Another way to calculate the dipole

With the 30-band $\mathbf{k} \cdot \mathbf{p}$ Hamiltonian at hand, we can evaluate the interband dipole directly via (2.29)

$$\boldsymbol{\xi}^{\mathbf{k}}_{\lambda\lambda'} = -\frac{\langle u_{\lambda\mathbf{k}} | \, i \, (\nabla_{\mathbf{k}} H_{\mathbf{k}}) \, | u_{\lambda'\mathbf{k}} \rangle}{\varepsilon_{\lambda\mathbf{k}} - \varepsilon_{\lambda'\mathbf{k}}} = -\frac{\langle u_{\lambda\mathbf{k}} | \, i\hbar\mathbf{v} \, | u_{\lambda'\mathbf{k}} \rangle}{\varepsilon_{\lambda\mathbf{k}} - \varepsilon_{\lambda'\mathbf{k}}}. \tag{2.44}$$

For other band structures, where me may only know the eigenvectors $|u_{\lambda\mathbf{k}}\rangle$, the dipole $\boldsymbol{\xi}^{\mathbf{k}}_{\lambda\lambda'}$ can be extracted from the just overlap matrix. We give here an improved version of the retrieving formula for $\boldsymbol{\xi}^{\mathbf{k}}_{\lambda\lambda'}$, compared to the one proposed in [28]

$$\boldsymbol{\xi}'^{\mathbf{k}_\nu} = \frac{i}{2\Delta\mathbf{k}_\nu} W^{\mathbf{k}_0,\mathbf{k}} \left[S^{\mathbf{k},\mathbf{k}+\Delta\mathbf{k}}_{\text{inter}} \left(S^{\mathbf{k},\mathbf{k}+\Delta\mathbf{k}}_{\text{intra}} \right)^\dagger - \left(S^{\mathbf{k}-\Delta\mathbf{k},\mathbf{k}}_{\text{inter}} \right)^\dagger S^{\mathbf{k}-\Delta\mathbf{k},\mathbf{k}}_{\text{intra}} \right] \left(W^{\mathbf{k}_0,\mathbf{k}} \right)^\dagger. \tag{2.45}$$

This formula's is more precise with a denser k-grid, and in excellent agreement with the analytical formula (2.44), as illustrated in figure 2.4. This method is based on perturbation theory and correct to first order of $\Delta\mathbf{k}$. It is worth emphasizing that the full dipole is computable, even though its interblock part may be null due to gauge-choice. It is at our disposal to construct another gauge with non zero intrablock dipole from the parallel transport gauge.

2.4 Berry curvature of Bloch states

Band structures, in terms of energy levels, for a long time have successfully described various electronic properties of materials. However, recent progress in the field has been made thanks to a more subtle aspect of electrons in crystals, the Berry curvature of Bloch states. The concept of Berry phase and curvature has been systematized since the paper by Micheal Berry (1984) and has been proven to be useful in many fields of physics. So much so that its derivation can be found in an elementary text such as Griffiths' [4] and Sakurai [7]. The main references for this section are a recent book by Vanderbilt (2018) [8] and the pedagogical review by Xiao (2010) [31].

2.4.1 Adiabatic evolution

For a quantum system that depends on the parameters $\boldsymbol{\mathcal{R}} = \{\mathcal{R}_1, \mathcal{R}_2, ...\}$.Let us introduce the notion of instantaneous eigenstate $|n(\boldsymbol{\mathcal{R}})\rangle$

$$H(\boldsymbol{\mathcal{R}}) \, |n(\boldsymbol{\mathcal{R}})\rangle = \varepsilon_n(\boldsymbol{\mathcal{R}}) \, |n(\boldsymbol{\mathcal{R}})\rangle \tag{2.46}$$

If the Hamiltonian varies slowly enough*, the adiabatic theorem says (to zero order of $\dot{\mathcal{R}}$) that: The system initially in one of its eigenstates will remain in the corresponding instantaneous eigenstate forever, albeit with an attached phase factor.

$$|\psi_n(t)\rangle = e^{i\gamma_n} \exp\left\{-\frac{i}{\hbar}\int \mathcal{R}(t)dt\right\}|n(\mathcal{R})\rangle. \tag{2.47}$$

where

$$\gamma_n = \int \mathcal{A}_n \cdot d\mathcal{R} \tag{2.48}$$

with $\mathcal{A}_n(\mathcal{R}) = \langle n(\mathcal{R})|\, i\frac{\partial}{\partial \mathcal{R}}\, |n(\mathcal{R})\rangle$. The vector $\mathcal{A}_n(\mathcal{R})$ is called *Berry connection*, which depends on the gauge of $|n(\mathcal{R})\rangle$. The time-independent phase angle γ_n is the *Berry phase*, which also bears the name *geometric phase* since it only depends on the geometry of the path in parameter space $\mathcal{R}$, not on how fast or slow $\mathcal{R}(t)$ evolves with time.

While Berry connection is clearly gauge-dependent, Berry phase is invariant along a closed path in $\mathcal{R}$ and could be observed. If we change (2.48) to a surface integral, another useful quantity is introduced: the Berry curvature tensor.

$$\gamma_n = \int \frac{1}{2}\Omega^n_{\mu\nu}(\mathcal{R})d\mathcal{R}^\mu \wedge d\mathcal{R}^\nu \tag{2.49}$$

$$\Omega^n_{\mu\nu} = \frac{\partial}{\partial\mathcal{R}^\mu}\mathcal{A}^n_\nu - \frac{\partial}{\partial\mathcal{R}^\nu}\mathcal{A}^n_\mu = i\left[\langle\partial_\mu n|\partial_\nu n\rangle - \langle\partial_\nu n|\partial_\mu n\rangle\right]. \tag{2.50}$$

Berry curvature is also gauge-invariant and therefore observable. There exists the resemblance of $\mathcal{A}_n(\mathcal{R})$ with EM potential and $\Omega^n_{\mu\nu}$ to EM field strength. In 3D parameter space, as in 3D crystals where the parameter is $\mathbf{k}$, the relation becomes

$$\gamma_n = \int \mathbf{\Omega}_n \cdot d\mathbf{\mathcal{S}} \tag{2.51}$$

$$\mathbf{\Omega}_n = \nabla_{\mathcal{R}} \times \mathcal{A}_\lambda. \tag{2.52}$$

2.4.2 Berry curvature in crystals

As for periodic systems, we have been dealing with the effective Hamiltonian $H(\mathbf{k}) = e^{-i\mathbf{k}\cdot\mathbf{r}}He^{i\mathbf{k}\cdot\mathbf{r}}$ and the states $|u_{\lambda\mathbf{k}}\rangle$. Hence, the parameter space coincides with the reciprocal lattice. Our system now lives in a closed manifold - the Brillouin zone. Berry connection and Berry curvature could be defined similarly

$$\mathbf{A}_\lambda(\mathbf{k}) = \langle u_{\lambda\mathbf{k}}|\, i\nabla_{\mathbf{k}}\, |u_{\lambda\mathbf{k}}\rangle \tag{2.53}$$

$$\mathbf{\Omega}_\lambda(\mathbf{k}) = \nabla_{\mathbf{k}} \times \mathbf{A}_\lambda = i\langle\nabla_{\mathbf{k}}u_{\lambda\mathbf{k}}| \times |\nabla_{\mathbf{k}}u_{\lambda\mathbf{k}}\rangle. \tag{2.54}$$

---

*The validity condition requires $i\hbar\dot{H}$ be small compared to energy level separation of the system.

The Berry curvature can be evaluated directly from $H^{\mathbf{k}}$ and $\varepsilon_{\lambda\mathbf{k}}$, emphasizing its gauge-independence

$$\begin{aligned}\boldsymbol{\Omega}_\lambda(\mathbf{k}) &= i\sum_{\mu\neq\lambda}\langle\nabla_{\mathbf{k}}u_{\lambda\mathbf{k}}|u_{\mu\mathbf{k}}\rangle\times\langle u_{\mu\mathbf{k}}|\nabla_{\mathbf{k}}u_{\lambda\mathbf{k}}\rangle \\ &= i\sum_{\mu\neq\lambda}\frac{\langle u_{\lambda\mathbf{k}}|\nabla_{\mathbf{k}}H^{\mathbf{k}}|u_{\mu\mathbf{k}}\rangle\times\langle u_{\mu\mathbf{k}}|\nabla_{\mathbf{k}}H^{\mathbf{k}}|u_{\lambda\mathbf{k}}\rangle}{(\varepsilon_{\lambda\mathbf{k}}-\varepsilon_{\mu\mathbf{k}})^2},\end{aligned} \tag{2.55}$$

where we have applied the familiar relation (2.44). This is called the Kubo formula for Berry curvature [16].

Non-Abelian Berry curvature
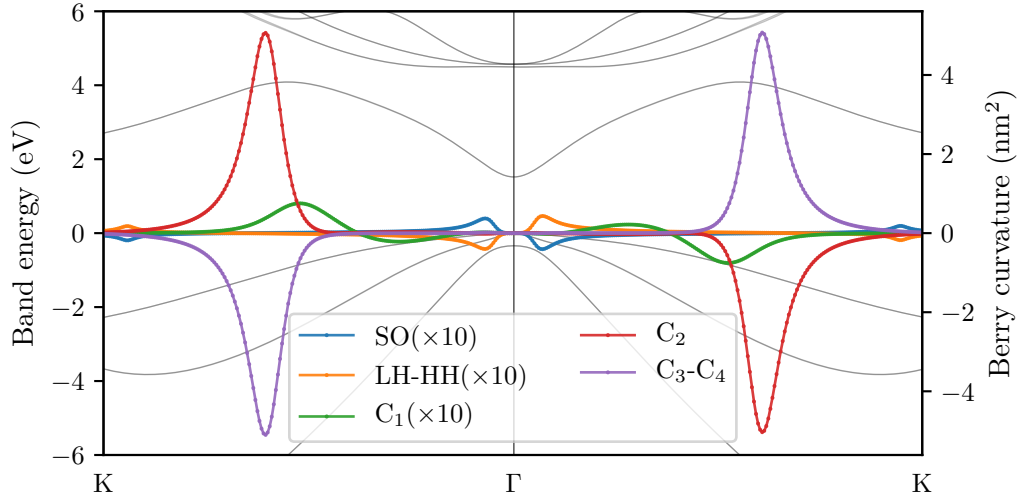
Figure 2.5: Multiband Berry curvature in the ΓK direction (it is zero along ΓX and ΓL). Plotted are the traces of the x-component of Berry curvature matrix. The y-component shows similar characteristic, while the z-component vanishes. Together, these indicate that GaAs' Berry curvature is non-zero near the ΓK line and points towards direction $[1\bar{1}0]$. Further, in a system broken inversion while time-reversal symmetry is preserved, like GaAs, Berry curvature is indeed an odd function in k-space [31].

In case of degeneracy, typically spin degeneracy of energy bands, we have to modified the above definition, working with a non-Abelian gauge field in each subspace [8, 31].

$$\mathbf{A}_{\lambda\lambda'} = \langle u_{\lambda\mathbf{k}}|i\nabla_{\mathbf{k}}|u_{\lambda'\mathbf{k}}\rangle \equiv \boldsymbol{\xi}_{\lambda\lambda'} \tag{2.56}$$

$$\boldsymbol{\Omega} = \nabla_{\mathbf{k}}\times\mathbf{A} - i\mathbf{A}\times\mathbf{A} \tag{2.57}$$

which in explicit form reads

$$\mathbf{A}^\mu_{\lambda\lambda'} = \langle u_{\lambda\mathbf{k}}|i\partial^\mu|u_{\lambda'\mathbf{k}}\rangle \tag{2.58}$$

$$\boldsymbol{\Omega}^{\mu\nu}_{\lambda\lambda'} = \partial^\mu\mathbf{A}^\nu_{\lambda\lambda'} - \partial^\nu\mathbf{A}^\mu_{\lambda\lambda'} - i[\mathbf{A}^\mu,\mathbf{A}^\nu]_{\lambda\lambda'} \tag{2.59}$$

where λ, λ' belong to the same block of bands and μ, ν are directions in k-space. Then the Berry curvature is gauge-covariant and give physical observables after tracing over occupied bands. The invariant traces are illustrated in figure 2.5. Besides, this newly defined Berry connection coincides with the dipole $\boldsymbol{\xi}_{\lambda\lambda'}(\mathbf{k})$.

2.4.3 Adiabatic electronic transport

When Bloch electrons move in EM fields, a semi-classical picture of the electron wave packet with position $\mathbf{r}$ and wave vector $\mathbf{k}$ is represented via[*]

$$\mathbf{v}_n = \dot{\mathbf{r}}_n = \frac{1}{\hbar}\nabla_\mathbf{k}\varepsilon_{\lambda\mathbf{k}}, \quad \hbar\dot{\mathbf{k}} = e\mathbf{E} + e\dot{\mathbf{r}} \times \mathbf{B}, \tag{2.60}$$

with the validity condition requiring, among others that there is no transition between energy bands.[†]However such a simple account cannot describe effects up to first order of the field strength. The improvement is made via the so-called anomalous velocity formula [26, 31]

$$\mathbf{v}_n^\mathbf{k} = \frac{1}{\hbar}\nabla_\mathbf{k}\varepsilon_{\lambda\mathbf{k}} - \dot{\mathbf{k}} \times \boldsymbol{\Omega}_n^\mathbf{k} = \frac{1}{\hbar}\nabla_\mathbf{k}\varepsilon_{\lambda\mathbf{k}} - \frac{e}{\hbar}\mathbf{E} \times \boldsymbol{\Omega}_n^\mathbf{k}. \tag{2.61}$$

The second term is known as anomalous velocity, which is perpendicular to the electric field and proportional to the crystal's Berry curvature.[‡]

Another explanation for this term is based on the quantum operator $\mathbf{v}^\mathbf{k}$'s off-diagonal matrix elements. It is the electric field cause the density matrix $\rho_{\lambda\lambda'}^\mathbf{k}$ to be mixed between bands, as can be seen from the SBE (2.17). Therefore, the semiclassical picture should be reinforced with a contribution to first order in the field. Later, our results indeed show that this anomalous term is mainly responsible for the HHG spectrum whose polarization is perpendicular to the laser's. Indeed, that signal originates almost entirely from the off-diagonal elements of $\mathbf{v}^\mathbf{k}$.

---

[*]See [1], chapter 12.

[†]The word **adiabatic** dates back to the 19th century: from Greek adiabatos 'impassable'(a 'not' + dia 'through' + batos 'passable').

[‡]Where we have ignore the magnetic field $\mathbf{B}$, since in a light wave, its effect is neglegible compared to the electric field $\mathbf{E}$.

Chapter 3

Results and discussion

3.1 Ordinary HHG

3.1.1 Compare with experiment

This section is devoted to the verification of our theoretical model. The HHG experiment in GaAs was recently reported in 2018 [30]. The paper investigated propagation effects by comparing reflected and transmitted HHG signals. Therefore, we can take the reflected one as a benchmark for theoretical results. The experimental setup was described via

- $E_{\text{gap}} = 1.42$ eV, corresponding to $T = 300$ K.

- The driving laser pulse is 60 fs (5 cycles).

- Wavelength $= 3.5$ μm, corresponding to $\varepsilon_{\text{photon}} = \mathcal{E}_{\text{gap}}/4$ [11].

- Maximum effective field strength $E \approx 1$ V/nm.

These conditions are translated to numerical implementation as follows

- E_{gap} is set at 1.519 eV, since we have accessed to GaAs's band structure only at $T = 0$ K.

- The laser pulse take the Gaussian form $E(t) = E_0 e^{-2\ln(2)t^2/\tau^2} \cos(\omega t)$, where τ is called FWHM (full width at half maximum).

- Laser duration of five cycles corresponds to $\tau = 5\dfrac{2\pi}{\omega}$.

- $\hbar\omega = \varepsilon_{\text{photon}} = \mathcal{E}_{\text{gap}}/4$.

- $E_0 = 1$ V/nm.

The energy levels of GaAs, obtained by numerically diagonalizing the 30-band $\mathbf{k} \cdot \mathbf{p}$ Hamiltonian, are shown in figure 2.1. After transforming into the parallel transport gauge of Bloch vectors, as presented in section 2.3.2, the operators $\boldsymbol{\xi}^{\mathbf{k}}$ becomes smooth and is used to solve the SBE. The important matrix elements of $\boldsymbol{\xi}^{\mathbf{k}}_{\lambda\lambda'}$ in direction ΓK and ΓL are shown in figures E.1 and E.2.

To study HHG, the SBE equation*

$$\frac{d\rho^{\mathbf{k}}}{dt} = -\frac{i}{\hbar}\left[H^{\mathbf{k}}, \rho^{\mathbf{k}}\right] - \frac{1}{\hbar}e\mathbf{E}(t) \cdot \nabla_{\mathbf{k}}\rho^{\mathbf{k}} - \frac{i}{\hbar}e\mathbf{E}(t) \cdot \left[\rho^{\mathbf{k}}, \boldsymbol{\xi}^{\mathbf{k}}\right] \tag{3.1}$$

is solved with relaxation-time approximation for Coulomb and phonon effects described by

$$\frac{\mathrm{d}\rho_{\lambda\lambda'}}{\mathrm{d}t}\bigg|_{\text{scatt}} = -\frac{\rho_{\lambda\lambda'}}{T_2} \tag{3.2}$$

with $T_2 = 2 \pm 0.5$ fs to produce suitable results with experiment in [30]. T_2 is the only fitting parameter in our model, which in the results below was set to 2fs. As in the experiment, we study excitations in the two highly symmetric directions ΓK and ΓL, with the 1-D k-grid is chosen to include both the Γ point and one of BZ's boundary. The results are illustrated below, where we have considered 14 most relevant bands (6 valence and 8 conduction) near the band gap region.

Densities

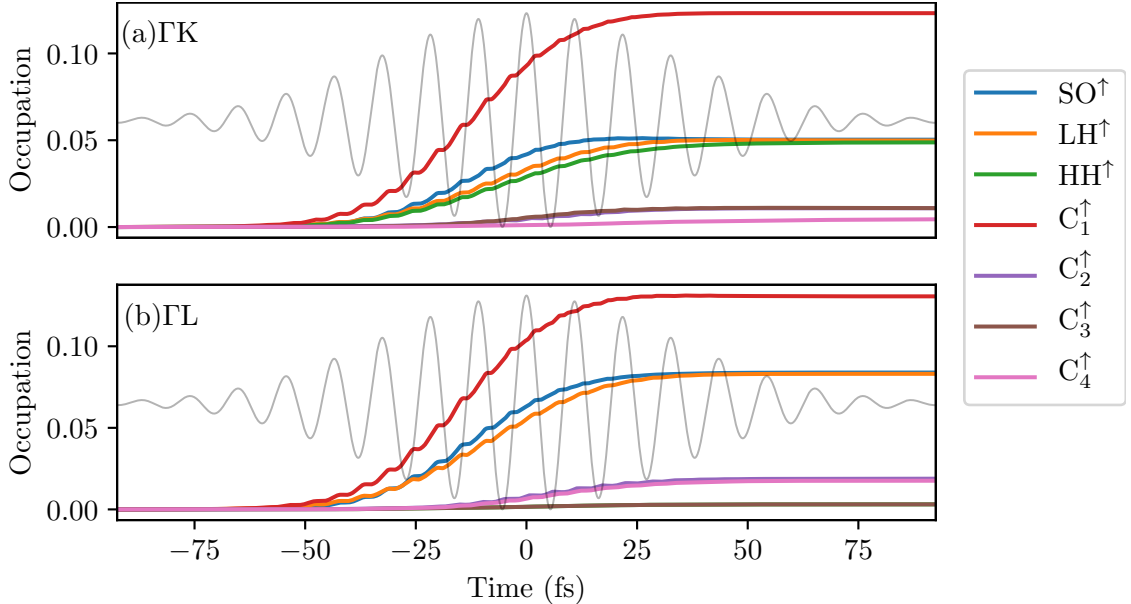Figure 3.1: The total occupation of holes in valence bands and electrons in conduction bands in (a) ΓK and (b) ΓL directions. Two spin-degenerate bands have nearly the same occupation, only one of which is plotted. The grey lines show the laser pulse's shape.

---

*Both $H^{\mathbf{k}}$ and $\boldsymbol{\xi}^{\mathbf{k}}$ has been rotated by the transformation $W^{\mathbf{k}}$ in the equation (2.40).

The initial condition for $\rho_{\lambda\lambda'}^{\mathbf{k}}$ is set such that all valence bands are filled and all conduction bands are empty. In figure 3.1, it can be seen that the first conduction band is where most electrons are excited to, in both directions. When the driving field is turned off, occupations on each band remain constant, since the time scale considered here is too short for recombination effects to take hold. On all bands, the pattern is clear that electrons'
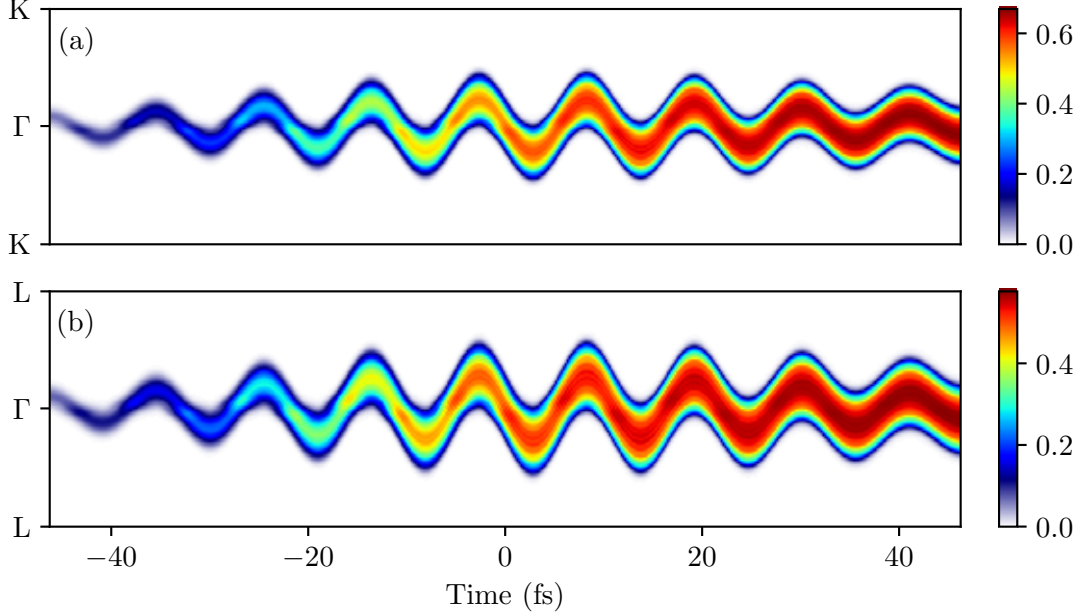
Figure 3.2: Occupation number of the lowest valence band (C_1) in (a) ΓK and (b) ΓL directions. Note that at $t = 0$, the wavepacket returns to Γ ($\mathbf{k} = 0$), while the electric field reaches maximum, which shows a phase difference of $\dfrac{\pi}{2}$.

wavepacket in reciprocal space follows the electric field's sinusoidal pattern, with a phase difference of $\dfrac{\pi}{2}$, as in figure 3.2. This is explained by the semi-classical equation $\hbar\dot{\mathbf{k}} = e\mathbf{E}$ in section 2.4.3. Furthermore, electrons undergo transition mostly at the Γ region, where the relevant matrix elements $\boldsymbol{\xi}_{\lambda\lambda'}^{\mathbf{k}}$ are dominantly large.[*]

Currents

After obtaining the evolution of $\rho^{\mathbf{k}}(t)$, the photoexcited current density is calculated via

$$\mathbf{j} = e\operatorname{Tr}[\mathbf{v}\rho] = e\sum_{\lambda}(\mathbf{v}^{\mathbf{k}}\rho^{\mathbf{k}})_{\lambda\lambda} = e\sum_{\lambda\lambda'}\mathbf{v}_{\lambda\lambda'}^{\mathbf{k}}\rho_{\lambda'\lambda}^{\mathbf{k}}.$$

The current is usually divided into two components and analyzed separately

$$\mathbf{j}_{\text{intra}} = e\sum_{\lambda}\mathbf{v}_{\lambda\lambda}^{\mathbf{k}}\rho_{\lambda\lambda}^{\mathbf{k}}, \quad \mathbf{j}_{\text{inter}} = e\sum_{\lambda\neq\lambda'}\mathbf{v}_{\lambda\lambda'}^{\mathbf{k}}\rho_{\lambda'\lambda}^{\mathbf{k}}, \tag{3.3}$$

where $\mathbf{j}_{\text{intra}}$ represents the ballistic transport, caused by electron traversing on the energy bands and $\mathbf{j}_{\text{inter}}$ interpreted as originating from the transition between bands. Both of

---

[*]See figures E.1 and E.2.
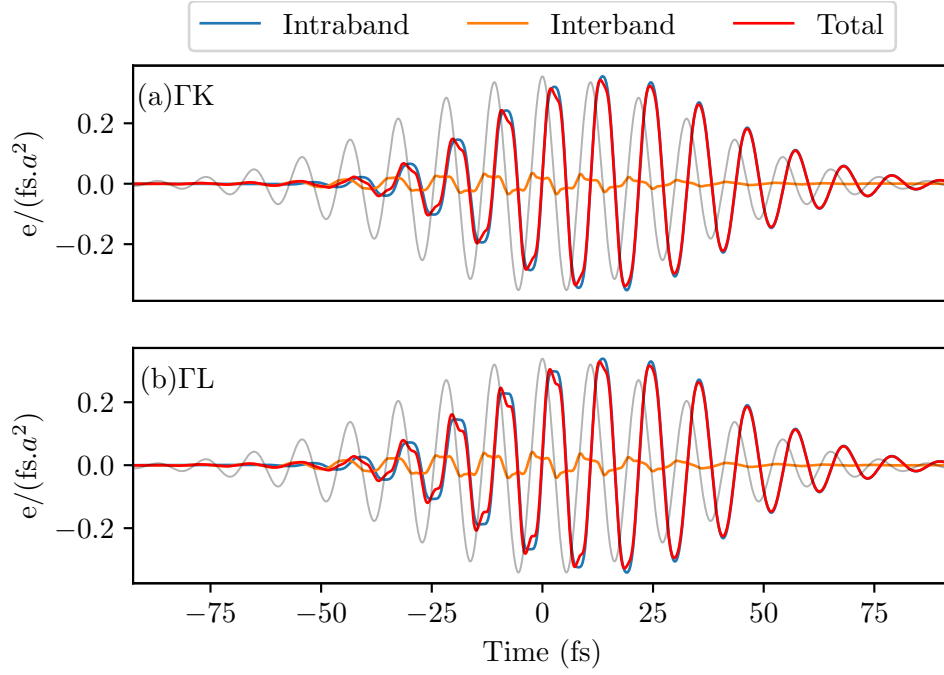
Figure 3.3: Temporal profile of HHG currents in the direction (a) ΓK and (b) ΓL. The parameters is described in figure 3.5. The intraband current lags a phase of $\pi/2$ behind the laser, similar to the wavepacket's dynamics. whereas interband current just follows the electric field. In the current's unit, a is the Bravais primitive cell's side ($2a = 0.565$ nm), and electron's charge e is understood as positive. The grey line indicates the driving laser field.

them are illustrated in figure 3.3. As the wavepacket lags a phase $\pi/2$ after the laser field, intraband current exhibits the same pattern, which validates its origin as the wavepacket's motion in k-space. On the other hand, the interband component just follows the driving field. This is the visualization of the last term in equation (3.1), in which the transition dipole couple the electric field into density matrix's dynamics.

Spectral profile

The photoexcited current oscillates rapidly and emits HHG radiation. The spectral intensity is calculated via

$$I_{\mathrm{HHG}}(\omega) \propto |\mathbf{j}(\omega)|^2.$$

In the spectra in figure 3.4, the pattern is that intraband contribution dominates in the below-band-gap region, while higher frequencies are dominated by the interband component.[*] The peaks match very well integral harmonic orders, with even harmonics show up only in ΓL direction. Moreover, a plateau can be seen in the above band gap region, in which intensities are kept constant from the 9th to the 17th harmonics (figure 3.4.b).

Finally, our result is compared with the experimental data in [30], as shown in figures 3.5.a and 3.5.c. The agreement is generally good, with even harmonics appearing only in

---

[*]This still holds when the laser frequency is varied, see figure ... for an example.
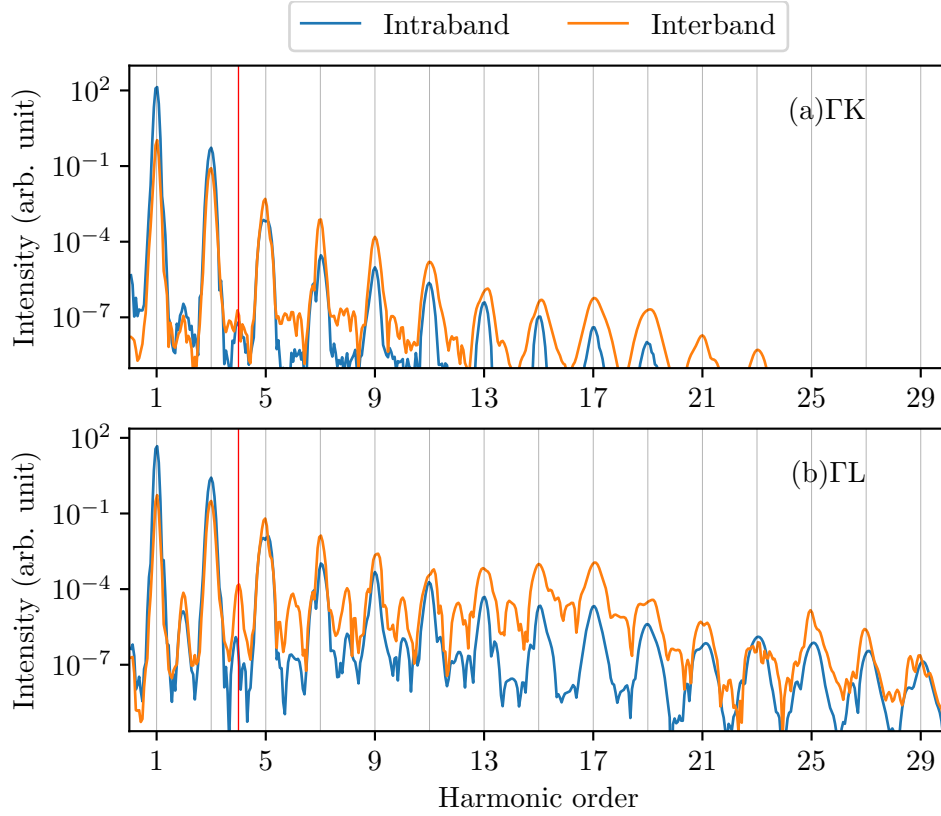
Figure 3.4: Spectral profile of HHG currents, devided into intraband and interband components, in (a)ΓK and (b)ΓL directions. The parameters is described in figure 3.5 and the red line indicates band gap position. It is seen that the interplay between intraband and interband contribution changes below and above the band gap. Note that in logarithm scale, the total spectral almost coincide with the larger component's line, hence need not be plotted.

the ΓL direction.* The difference between theory and experiment could be attributed to the following reasons.

- The SBE was only solved in one dimension, along the laser's polarization. While this direction is where most electrons are excited, the adjacent states may produce some effects, especially at low intensity region of the spectrum.

- As for even harmonics caused by broken inversion symmetry, the 30-band $\mathbf{k} \cdot \mathbf{p}$ Hamiltonian for GaAs uses only one parameter (P') to describe the effect, which is regarded as controversial by its own author, being far too small when compared with other models [23]. Indeed, by doubling P', ,without much alteration to the relevant band energies†, the even order peaks match very well, as in figures 3.5.b and 3.5.d.

- The experiment reported a band gap of 1.42 eV, suggesting a temperature around 300 K [11]. What we did is just imitating the experimental set up, by scale the

---

*Nevertheless, it should be noted that excitation in the ΓK direction also produces even harmonics with polarization along [001], which will be analyzed in the next section. However, the experiment used a GaAs layer perpendicular to that direction, hence could not observe the effects.

†See figure E.5
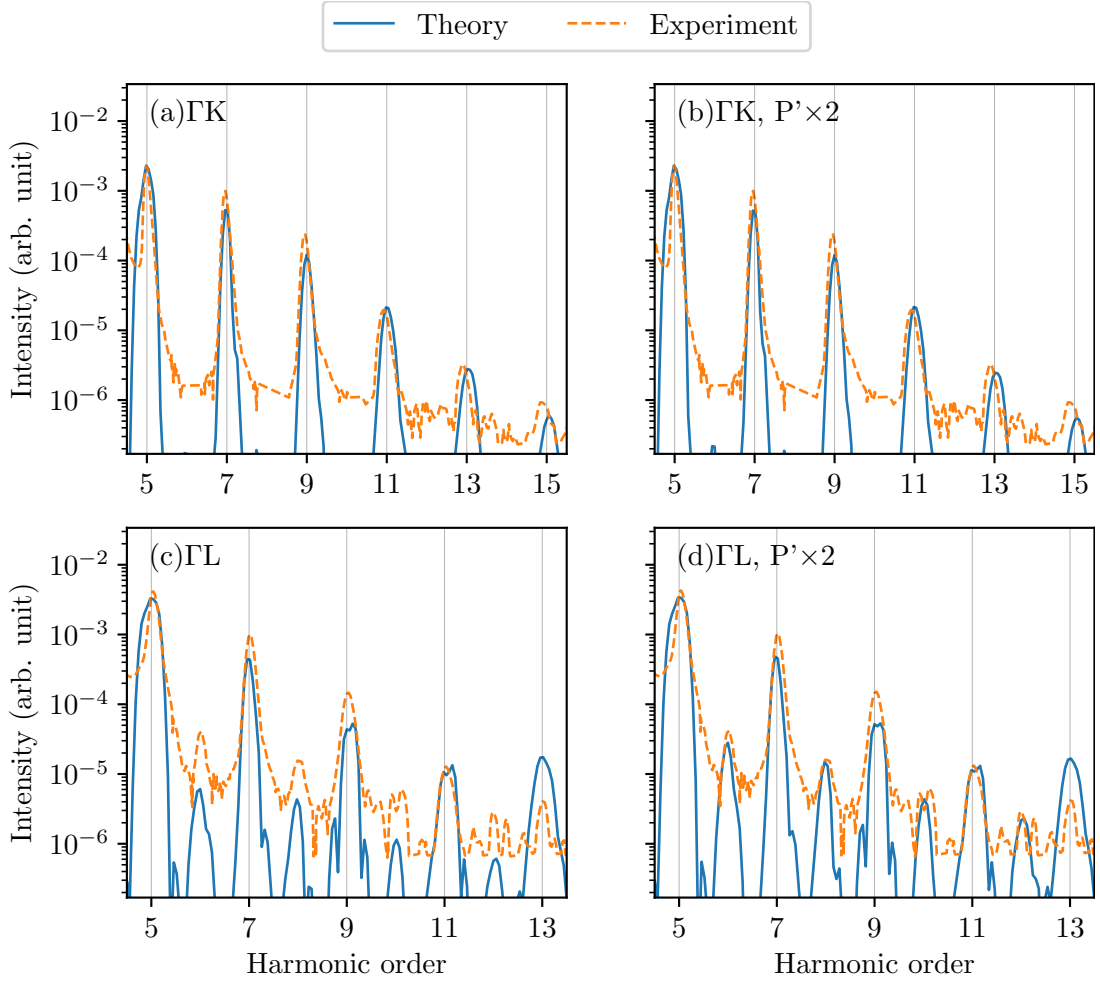
Figure 3.5: The calculated HHG signal in directions ΓK (a,b) and ΓL (c,d), compared with the experiment in [30]. (a) and (b) use the original 30-band $\mathbf{k} \cdot \mathbf{p}$ Hamiltonian, while (c) and (d) use the doubly larger P' parameter. The laser pulse has maximum strength $E_0 = 1$ V/nm, with FWHM of 5 cycles, $\varepsilon_{\text{photon}} = \mathcal{E}_{\text{gap}}/4$. The dephasing time is kept constant at $T_2 = 2$ fs.

photon energy to match with $\mathcal{E}_{\text{gap}}/4$.

- The Coulomb and phonon effects may have not been addressed properly. The relaxation time approximation is too simple to describe these subtle effects.

- The main object of study in the experiment [30] was the difference between reflected and transmitted HHG, not the absolute value of the HHG signal. Further, while the ΓK direction was clearly specified, the ΓL may be just approximate, as the paper didn't make it clear anyway.

3.1.2 The role of transition dipole's phase

Our model with complex-valued dipole has proven itself to be so successful and therefore can be used as a benchmark to assess other relevant approaches. If a smooth gauge for Bloch functions had not been obtained, we are forced to take the averaged absolute value of the transition dipole via formula (2.39). In that case, the result is presented in figure
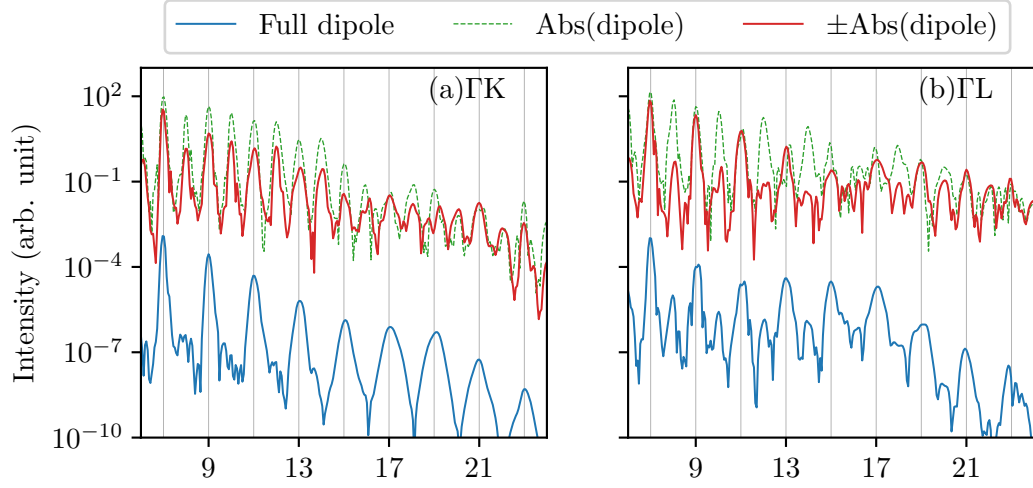
Figure 3.6: The HHG signal calculated with and without transition dipole's phase in (a) ΓK and (b) ΓL directions, with parameters the same as in figure 3.5. The absolute values of dipole matrix elements used to solve the SBE is shown in figure E.4

3.6. The downside of that procedure includes

- The photoexcited current and hence the HHG signal is predicted to be too large.

- The intraband current does not decay correctly. To remove that non-decay component, we had to resort to the technique $I_{\text{HHG}}(\omega) \propto |\mathbf{j}(\omega)|^2 \mapsto \frac{1}{\omega^2}\left|\frac{d\mathbf{j}}{dt}(\omega)\right|^2$.

- The worst failure is the erroneous prediction of even harmonics in directions ΓK and ΓX.[*] That is, without the dipole's phase we cannot distinguish different crystal symmetries.

There are two main reasons causing these inadequacies:

- First, all the dipole's matrix elements are biased towards positive values. Since $\boldsymbol{\xi}^{\mathbf{k}}$ couples the the electric field and $\rho^{\mathbf{k}}$, the density matrix is subjected to the same biasing. Normally, both negative and positive values are present, and are able to cancel each other. Here, all these positive values add up, thus result in such a large current.

- Second, taking the amplitude alone bring unphysical kinks to the dipole $\boldsymbol{\xi}^{\mathbf{k}}_{\lambda\lambda'}$ as a function of $\mathbf{k}$, which mistakenly intensifies even harmonics' strength. The remedy is to attach suitable signs to $\boldsymbol{\xi}_{\lambda\lambda'}$ so that it becomes smooth. This gives somewhat better relative yield between odd and even peaks in ΓL direction (figure 3.6.b).

---

[*]See figure ... for the spectra in direction ΓX.

3.2 Transverse HHG caused by Berry curvature

In the last section, the experiment and theoretical result showed that even-order harmonics only appear when excitation is along ΓL. However, the ΓK direction also has broken inversion symmetry and exhibit even harmonics, albeit with polarization perpendicular to the driving field, which was not observed for geometrical reason. In this section, we investigate that transverse signal, showing that it indeed originates from the crystal's Berry curvature. The contribution caused by Berry curvature is calculated from the second term in the anomalous velocity formula (2.61) [*]

$$\mathbf{v}_\perp = -\dot{\mathbf{k}} \times \boldsymbol{\Omega} = \frac{-e}{\hbar}\mathbf{E} \times \boldsymbol{\Omega}.$$

Where the macroscopic $\boldsymbol{\Omega}$ was obtained by tracing with the density matrix $\boldsymbol{\Omega} = \sum_{\mathbf{k}\lambda\lambda'} \rho^{\mathbf{k}}_{\lambda\lambda'}\boldsymbol{\Omega}^{\mathbf{k}}_{\lambda'\lambda}$.

Although we have solved the SBE in just one dimension, the photocurrent in other directions can still be extracted thanks to the 3D velocity operator $\mathbf{v}^{\mathbf{k}}$. When excitation is along [110], the transverse HHG shows up with polarization [001]. This is predictable since the anomalous current $\mathbf{v}_\perp \propto \mathbf{E} \times \boldsymbol{\Omega}$ oscillates in direction $[110] \times [1\bar{1}0] = [001]$.[†]

The results are shown in figure 3.7, showing that Berry curvature's contribution dominate the spectral region below the band gap. On the other hand, this again confirms the validity of our theoretical method. The temporal profile is given in figure 3.8.

The reason why transverse HHG is dominated by even harmonics is attributed to the Berry curvature being an odd function in k-space $\boldsymbol{\Omega}(-\mathbf{k}) = -\boldsymbol{\Omega}(\mathbf{k})$.[‡]This is simply illustrated in the long pulse limit, in which the driving field takes sinusoidal form [20, 22]. Then the following identities hold, where T is the period of the light wave.

$$\begin{cases} \mathbf{k}(t + T/2) = -\mathbf{k}(t), & \text{since } \dot{\mathbf{k}} \propto \mathbf{E}, \\ \dot{\mathbf{k}}(t + T/2) = -\dot{\mathbf{k}}(t). \end{cases} \tag{3.4}$$

That leads to

$$\mathbf{v}_\perp(t + T/2) \propto \dot{\mathbf{k}}(t + T/2) \times \boldsymbol{\Omega}[\mathbf{k}(t + T/2)] \tag{3.5}$$

$$= -\dot{\mathbf{k}}(t)\boldsymbol{\Omega}[-\mathbf{k}(t)] \tag{3.6}$$

$$= \dot{\mathbf{k}}(t)\boldsymbol{\Omega}[\mathbf{k}(t)] = \mathbf{v}_\perp(t), \tag{3.7}$$

---

[*]The first term in (2.61) was also calculated but just has negligible effect in the direction perperdicular to $\mathbf{E}$.

[†]Since GaAs's Berry curvature is dominantly large along [110] and points towards $[1\bar{1}1]$, see figure 2.5.

[‡]This must be satisfied in a system with broken inversion symmetry while time reversal symmetry is preserved. If both symmetries are present, Berry curvature vanishes. These are proved by requiring the formula $\mathbf{v}^{\mathbf{k}} = \frac{1}{\hbar}\nabla_{\mathbf{k}}\varepsilon_{\mathbf{k}} - \frac{e}{\hbar}\mathbf{E} \times \boldsymbol{\Omega}^{\mathbf{k}}$ invariant under the two symmetry operations.
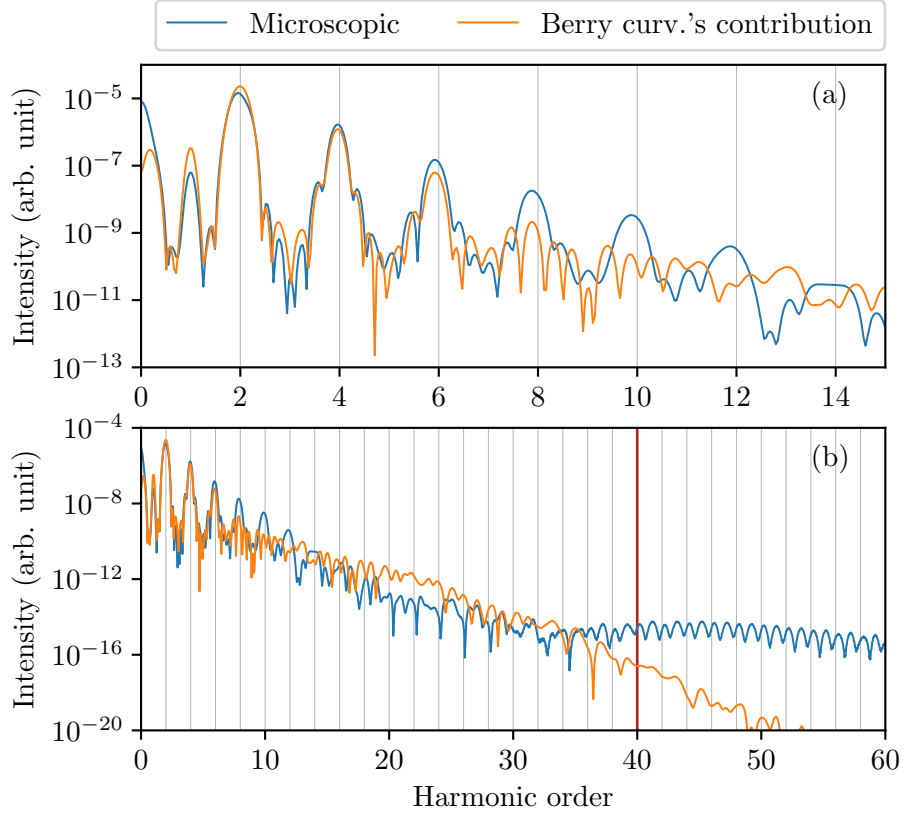
Figure 3.7: Transverse HHG signal caused by Berry curvature, where (b) is (a) replotted on a larger spectral region. The parameters used are: $\varepsilon_{\text{photon}} = \mathcal{E}_{\text{gap}}/4$, $E_0 = 0.2\text{V/nm}$ and $\parallel [110]$, $T_2 = 3.5$ fs. The value of T_2 was estimated via formula (2.23), with $\{T_2 = 300 \text{ fs}, T_2' = 1 \text{ fs}\}$, which is consistent with the value used when comparing with experiment. Nevertheless, changing T_2 the range [3,9] fs does not affect much the transverse spectral. The red line indicates band gap position and grey ones mark even=order harmonics.

showing that the tranverse HHG caused by anomalous current has a fundamental period of $2T$, and thus a fundamental frequency doubling the laser's. For that reason, the contribution by Berry curvature contains only even-order hamonics.

In the figures above, one may ask what is the source for the difference between Berry curvature's contribution and the total current. This could be explained as follows.

- The validity condition of the anomalous velocity formula (2.61) requires no interband transitions, but in fact, lots of transitions occur when the wave packet crosses the Γ region (figure 3.8.b).

- As can be see from figure 3.8.b, for most of the time, electrons traverse on its band, to the region where Berry curvature is large.* So much so that the contribution caused by Berry curvature dominates, while interband transitions can be considered as perturbation to the adiabatic transport.

- If we lower the field strength, so that the wave packet oscillates only around the

---

*See figure 2.5 C1's Berry curvature.
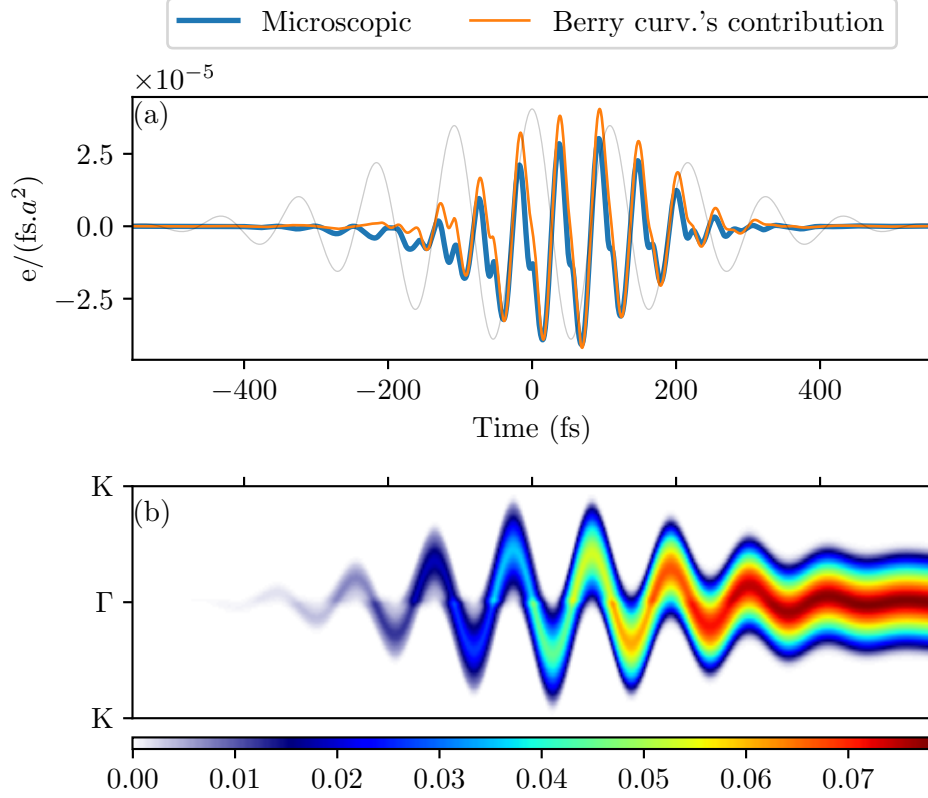
Figure 3.8: Temporal profile of (a) anomalous current radiating transverse HHG and (b) C_1's occupation number. The grey line is the laser field's shape. The spectral profile was shown in figure 3.7.

Γ region and undergoes lots of transition, the difference is indeed magnified, as in figures E.6 and E.7 (to be compared with figure 3.9).

- From the band structure (figure 2.1), it can be seen that the energy difference between C_2, C_3 and C_4 bands are very small compared to the fundamental band gap. Therefore, transitions between these bands may contribute high proportion to the HHG spectral at low-order harmonics. If we remove bands C_3 and C_4, the contribution from Berry-curvature would, as expected, dominate over a longer spectral range (figure 3.9).[*]

For these reasons, we conclude that interband transition is the source for the difference between Berry's contribution and the total current.[†]

---

[*]The justification here is that the occupation on C_2, C_3 and C_4 are small compared to that of C_1, similar to the case in figure 3.1. Further, for applications, one may choose materials that do not have such tiny gaps to study Berry curvature's effects.

[†]We noticed that the transverse HHG comes all from interband component. Moreover, the anomalous velocity cannot explain the zero-frequency part of the total current. These suggests that the difference could be related to the concept of shift vector in periodic systems [15].
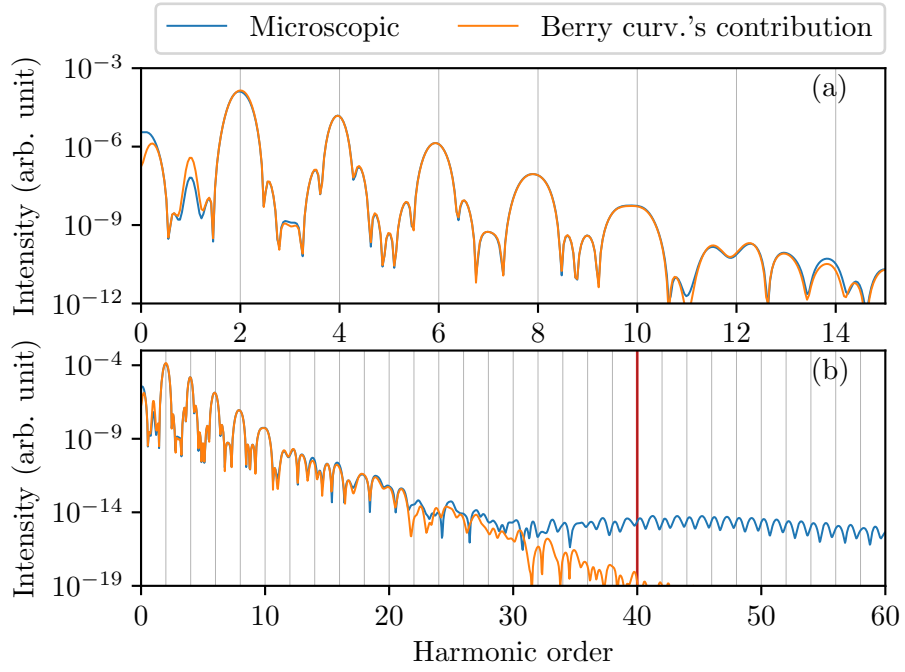
Figure 3.9: The same as figure 3.7, but with C_3 and C_4 bands removed to reduce transition with small energies. (b) is the same as (a) but replotted on a wider spectral region. The corresponding temporal profile is given in figure E.8.

Chapter 4

Conclusion and outlook

This thesis focuses on a microscopic approach to high harmonics generation in periodic systems, with a rather complete description of electronic transitions obtained via a smooth gauge of Bloch functions. The method is general can be applied to other realistic band structures, bringing about the capabilities of deeper studies into other electronic and optical properties of solids, especially under strong excitation.

To calculate HHG signals, we have solved the SBE equation, using 14 selected bands from the 30-band $\mathbf{k} \cdot \mathbf{p}$ method, and achieved good agreement with experiments. Specifically, our results leave two important remarks

- The transition dipole's phase is shown to be indispensable when dealing with subtle effects such as even harmonics, and we believe that its inclusion, thanks to the generality of our method, would make further progress to the studies of HHG and a large spectrum of other phenomena.[*]

- Crystals' Berry curvature is the source of transverse HHG in the spectral region below the band gap, especially the first few even harmonics. This result would motivate experimentalists to probe materials' Berry curvature through HHG signals, which may contribute to the studies of topological materials.

Further developments to this thesis include

- Analyze the possible relations between the non-Berry contribution and the shift current [15].

- Increase the field strength to study effects when electrons pass through the BZ boundary (Bloch oscillation).

- Investigate new schemes of excitation to increase harmonic yield.

---

[*]Even though the paper [19] has arrived at a similar conclusion, it is less general and their method cannot be applied to arbitrary band structures, since they only analyzed a simplified, analytical model.

- Upgrade the SBE to 2D and 3D k-grids.

- Describe Coulomb and phonon interactions beyond the relaxation-time approximation.

- Apply the parallel transport gauge to DFT band structures, where we have access to a large number of materials, to study both HHG and other related phenomena.

Appendix A

The Bloch basis

Electrons in solids is a truly complicated system, to which special techniques must be applied to circumvent the difficulties and extract the fundamental nature of each physical process. Bloch's theorem, which utilizes the power of symmetry, along with elementary approximations, tremendously simplifies the problem of electrons in solid.

While the ideas presented in this section maybe present in most standard books, I think they deserve to be made explicit at the undergraduate level. The main references for this section are [1] and [8]. The latter provides modern perspectives on the subject.

A.1 Discrete translational symmetry

In crystalline solids, an electron can be considered to move in a periodic potential $U(\mathbf{r})$ caused by both the array of positive ions and the average interaction with other electrons. The single particle Hamiltonian then has the form

$$H = \frac{\mathbf{p}^2}{2m} + U(\mathbf{r}), \quad U(\mathbf{r} + \mathbf{R}) = U(\mathbf{r}), \tag{A.1}$$

with $\mathbf{R}$ an arbitrary lattice vector. In an **infinite lattice**, this Hamiltonian commutes, and thus can be simultaneously diagonalized*, with all lattice translation operators $T_{\mathbf{R}}$[†]:

$[H, T_{\mathbf{R}}] = 0 \Leftrightarrow T_{\mathbf{R}}^\dagger H T_{\mathbf{R}} = H$. Therefore, we can choose the eigenstates of H to be also eigenstates of $T_{\mathbf{R}}$.

First, we diagonalize all $T_{\mathbf{R}}$ simultaneously to obtain common eigenstates $\psi_{\mathbf{k}}(\mathbf{r})$ called **Bloch waves**, each of which has the special property

---

[†]The spectral theorem states that commuting normal operators can be simultaneously diagonalized. A normal operator is one which commutes with its adjoint $[M, M^\dagger] = 0$. They comprise both unitary and hermitian operators.

[†]A translation operator (in real space), which translates a quantum state by a vector $\mathbf{r}$, is defined $\hat{T}_{\mathbf{r}} = e^{-\frac{i}{\hbar}\mathbf{r}\cdot\hat{\mathbf{p}}}$. It is clear that such operators are unitary and commute with one another.

$$\psi_{\mathbf{k}}(\mathbf{r} + \mathbf{R}) = e^{i\mathbf{k}\cdot\mathbf{R}}\psi_{\mathbf{k}}(\mathbf{r}), \tag{A.2}$$

where $\mathbf{k}$ is the quantum number labeling the obtained eigenstates. In particular, the proof below shows that $e^{i\mathbf{k}\cdot\mathbf{R}}$ is just the eigenvalue of $T_{\mathbf{R}}$.

Proof. (based only on $T_{\mathbf{R}}$'s properties.) Let $\psi_{\mathbf{k}}(\mathbf{r} + \mathbf{R})$ be an eigenstate of all $T_{\mathbf{R}}$. Since $T_{\mathbf{R}}$ is unitary, its eigenvalue has unit norm. We thus have

$$T_{\mathbf{R}}\psi(\mathbf{r}) = \psi(\mathbf{r} + \mathbf{R}) = e^{i\Phi_{\mathbf{R}}}\psi(\mathbf{r}), \quad \Phi_{\mathbf{R}} \in \mathbb{R}. \tag{A.3}$$

Due to the commutativity of $T_{\mathbf{R}}$, we have $\Phi_{\mathbf{R}} = n_i\Phi_{\mathbf{a}_i}$, with $\mathbf{R} = n_i\mathbf{a}_i$. That is, $\Phi_{\mathbf{R}}$ is proportional to $\mathbf{R}$ and can be written $\Phi_{\mathbf{R}} = \mathbf{k} \cdot \mathbf{R}$, where $\mathbf{k}$ is the the state ψ's quantum number with dimension of a wave vector. Therefore $\psi(\mathbf{r} + \mathbf{R}) = e^{i\mathbf{k}\cdot\mathbf{R}}\psi(\mathbf{r})$. $\qquad\square$

Next, we diagonalize H within the subspaces labeled by $\mathbf{k}$. That is, at each value of $\mathbf{k}$, there may exist energy degeneracy. Denoting the energy quantum number by λ, it is rewritten

$$\begin{cases} T_{\mathbf{R}}\psi_{\lambda\mathbf{k}}(\mathbf{r}) = \psi_{\lambda\mathbf{k}}(\mathbf{r} + \mathbf{R}) = e^{i\mathbf{k}\cdot\mathbf{R}}\psi_{\lambda\mathbf{k}}(\mathbf{r}) \\ H\psi_{\lambda\mathbf{k}}(\mathbf{r}) = \varepsilon_{\lambda\mathbf{k}}\psi_{\lambda\mathbf{k}}(\mathbf{r}). \end{cases} \tag{A.4}$$

A.2 Bloch waves' properties

The Bloch waves can be written as a product of a plane wave and a cell-periodic function:

$$\psi_{\lambda\mathbf{k}}(\mathbf{r}) = e^{i\mathbf{k}\mathbf{r}}u_{\lambda\mathbf{k}}(\mathbf{r}) \tag{A.5}$$

Proof. By definition, $u_{\mathbf{k}}(\mathbf{r}) = e^{-i\mathbf{k}\mathbf{r}}\psi_{\mathbf{k}}(\mathbf{r})$.

$$u_{\mathbf{k}}(\mathbf{r} + \mathbf{R}) = e^{-i\mathbf{k}\mathbf{r}}e^{-i\mathbf{k}\mathbf{R}}\psi_{\mathbf{k}}(\mathbf{r} + \mathbf{R}) = e^{-i\mathbf{k}\mathbf{r}}e^{-i\mathbf{k}\mathbf{R}}e^{i\mathbf{k}\mathbf{R}}\psi_{\mathbf{k}}(\mathbf{r}) = e^{-i\mathbf{k}\mathbf{r}}\psi_{\mathbf{k}}(\mathbf{r}) = u_{\mathbf{k}}(\mathbf{r}). \tag{A.6}$$

Therefore $u_{\mathbf{k}}(\mathbf{r} + \mathbf{R}) = u_{\mathbf{k}}(\mathbf{r})$. $\qquad\square$

The Hamiltonian equation for $u_{\mathbf{k}}(\mathbf{r})$ has the same form as that for $\psi_{\mathbf{k}}(\mathbf{r})$, except that it is reduced to the space of cell-periodic functions.

$$H_{\mathbf{k}}u_{\lambda\mathbf{k}}(\mathbf{r}) = \varepsilon_{\lambda\mathbf{k}}u_{\lambda\mathbf{k}}(\mathbf{r}), \quad H_{\mathbf{k}} \equiv e^{-i\mathbf{k}\mathbf{r}}He^{i\mathbf{k}\mathbf{r}}. \tag{A.7}$$

Considering the pair of eigenstates

$$
\begin{cases}
\psi_{\lambda,\mathbf{k}}(\mathbf{r}) = e^{i(\mathbf{k})\mathbf{r}} u_{\lambda,\mathbf{k}}(\mathbf{r}) \\
\psi_{\lambda,\mathbf{k}+\mathbf{G}}(\mathbf{r}) = e^{i(\mathbf{k}+\mathbf{G})\mathbf{r}} u_{\lambda,\mathbf{k}+\mathbf{G}}(\mathbf{r}) = e^{i\mathbf{k}\mathbf{r}} \tilde{u}_{\lambda,\mathbf{k}}(\mathbf{r}),
\end{cases}
\tag{A.8}
$$

where $\tilde{u}_{\lambda,\mathbf{k}}(\mathbf{r}) \equiv e^{i\mathbf{G}\mathbf{r}} u_{\lambda,\mathbf{k}+\mathbf{G}}(\mathbf{r})$ is still a cell-periodic function. It is seen that $u_{\lambda,\mathbf{k}+\mathbf{G}}(\mathbf{r})$ and $\tilde{u}_{\lambda,\mathbf{k}}(\mathbf{r})$ are respectively eigenvectors of $H_{\mathbf{k}+\mathbf{G}}$ and $H_{\mathbf{k}}$ with the same eigenvalue $\varepsilon_{\lambda,\mathbf{k}+\mathbf{G}}$. In other words, $H_{\mathbf{k}+\mathbf{G}}$ and $H_{\mathbf{k}}$ have the same set of eigenvalues and are thus unitarily equivalent under the transformation $U_{\mathbf{k}+\mathbf{G},\mathbf{k}} = e^{-i\mathbf{G}\mathbf{r}}$. It is interesting to note that the periodicity of H in the real lattice is inherited by $H_{\mathbf{k}}$ in the reciprocal.

Since $\{u_{\lambda,\mathbf{k}}(\mathbf{r})\}$ and $\{\tilde{u}_{\lambda,\mathbf{k}}(\mathbf{r})\}$ are both eigensystem of $H_{\mathbf{k}}$, their elements differ only by unitary phase factors and degenerate-subspace mixing. However we can fix that gauge freedom by requiring $u_{\lambda,\mathbf{k}}(\mathbf{r}) = \tilde{u}_{\lambda,\mathbf{k}}(\mathbf{r})$, with λ be consistent with that of ε_λ. This condition, which leads to

$$
\psi_{\lambda,\mathbf{k}+\mathbf{G}}(\mathbf{r}) = \psi_{\lambda,\mathbf{k}}(\mathbf{r}),
\tag{A.9}
$$

is called the **periodic gauge**. Note that this is a gauge in $\mathbf{k}$-space, and is not unique. There remains lot of gauge freedom, such as whether to require $\psi_{\lambda,\mathbf{k}}(\mathbf{r})$ be a continuous function w.r.t $\mathbf{k}$.

In summary, we have shown that $\psi_{\lambda,\mathbf{k}}(\mathbf{r})$ and $\psi_{\lambda,\mathbf{k}+\mathbf{G}}(\mathbf{r})$ represent the same physical state and can be chosen to be equal. Therefore, to obtain all energy eigenstates, we only need to solve the equation $H_{\mathbf{k}} u_{\lambda\mathbf{k}}(\mathbf{r}) = \varepsilon_{\lambda\mathbf{k}} u_{\lambda\mathbf{k}}(\mathbf{r})$ with $\mathbf{k}$-points in the first Brillouin zone. If we are in a periodic gauge, the following equalities hold

$$
\begin{cases}
\psi_{\lambda,\mathbf{k}}(\mathbf{r})) = \psi_{\lambda,\mathbf{k}+\mathbf{G}}(\mathbf{r}) \\
u_{\lambda,\mathbf{k}}(\mathbf{r}) = e^{i\mathbf{G}\mathbf{r}} u_{\lambda,\mathbf{k}+\mathbf{G}}(\mathbf{r}) \\
\varepsilon_{\lambda,\mathbf{k}+\mathbf{G}} = \varepsilon_{\lambda,\mathbf{k}}.
\end{cases}
\tag{A.10}
$$

The Hamiltonian equation can be written in terms of states (or vectors) (with $\mathbf{r}$ as operator and $\mathbf{k}$ as c-number). Without ambiguity, we will use "eigenstates" to denote both $|\psi_{\lambda\mathbf{k}}\rangle$ and its periodic part $|u_{\lambda\mathbf{k}}\rangle$.

$$
H |\psi_{\lambda\mathbf{k}}\rangle = \varepsilon_{\lambda\mathbf{k}} |\psi_{\lambda\mathbf{k}}\rangle, \quad |\psi_{\lambda\mathbf{k}}\rangle = e^{i\mathbf{k}\cdot\mathbf{r}} |u_{\lambda\mathbf{k}}\rangle
\tag{A.11}
$$

$$
H_{\mathbf{k}} |u_{\lambda\mathbf{k}}\rangle = \varepsilon_{\lambda\mathbf{k}} |u_{\lambda\mathbf{k}}\rangle, \quad H_{\mathbf{k}} \equiv e^{-i\mathbf{k}\cdot\mathbf{r}} H e^{i\mathbf{k}\cdot\mathbf{r}}.
\tag{A.12}
$$

A.3 Boundary condition

While Bloch's theorem was proved for an infinite periodic lattice, any real material we are going to deal with is finite-sized and the electronic wave function necessarily vanishes

beyond the boundary. Nonetheless, with the assumption that bulk properties of a large crystal are not affected much by the surface, we impose the Born-von Karman boundary condition on the wavefunctions

$$\psi(\mathbf{r} + N_i\mathbf{a}_i) = \psi(\mathbf{r}), \quad \forall i = 1, 2, 3 \tag{A.13}$$

where $N_i\mathbf{a}_i$ is the size of macroscopic crystal. Under this condition, the lattice has the geometry of a 3-torus. In another perspective, it can be still considered infinite, with supercells of size $N_i\mathbf{a}_i$ stacked up. This allows Bloch's theorem to be applicable to finite-sized systems.

It is worth noting that the boundary condition of the equation $H_\mathbf{k}u_{\lambda\mathbf{k}}(\mathbf{r}) = \varepsilon_{\lambda\mathbf{k}}u_{\lambda\mathbf{k}}(\mathbf{r})$ causes the energy levels become discrete. In the same manner, Born-von Karman condition restricts the values of $\mathbf{k}$ quantum number. Consider the eigenstate $\psi_\mathbf{k}(\mathbf{r})$, Bloch's theorem gives

$$\psi_\mathbf{k}(\mathbf{r} + N_i\mathbf{a}_i) = e^{iN_i\mathbf{k}\cdot\mathbf{a}_i}\psi_\mathbf{k}(\mathbf{r}) = \psi_\mathbf{k}(\mathbf{r}), \quad \forall i = 1, 2, 3 \tag{A.14}$$

$$\Leftrightarrow e^{iN_i\mathbf{k}\cdot\mathbf{a}_i} = 1 \Leftrightarrow N_i\mathbf{k}\cdot\mathbf{a}_i = m_i2\pi, \quad \forall i = 1, 2, 3 \tag{A.15}$$

Thus the allowed values for $\mathbf{k}$:

$$\mathbf{k} = \sum_i \frac{m_i}{N_i}\mathbf{G}_i, m_i \in \mathbb{Z}, m_i < N_i \tag{A.16}$$

In summary, the discreteness of energy index λ is due to the periodicity of the lattice, while that of $\mathbf{k}$ is due to the finite size of the crystal. Furthermore, since we have shown that $\mathbf{k}$ and $\mathbf{k} + \mathbf{G}$ represent the same physical state, the number of allowed values for $\mathbf{k}$ in the BZ equals to that of unit cells of the finite crystal.

A.4   Normalization convention

In this thesis, Bloch waves $\psi_{\lambda\mathbf{k}}(\mathbf{r}) = e^{i\mathbf{k}\cdot\mathbf{r}}u_{\lambda\mathbf{k}}(\mathbf{r})$ are defined with dimension $[\text{length}]^{-3/2}$.

$$\begin{cases} \langle u_{\lambda\mathbf{k}}|u_{\lambda'\mathbf{k}'}\rangle \equiv \int_\mathbf{\Omega} u^*_{\lambda\mathbf{k}}u_{\lambda'\mathbf{k}'}d\mathbf{r} \\ \langle \psi_{\lambda\mathbf{k}}|\psi_{\lambda'\mathbf{k}'}\rangle \equiv \int_\text{all} \psi^*_{\lambda\mathbf{k}}(\mathbf{r})\psi_{\lambda'\mathbf{k}'}(\mathbf{r})d\mathbf{r}. \end{cases} \tag{A.17}$$

Because the set $\{u_{\lambda\mathbf{k}}\}$ at each k-point can be made to be orthonormal, we set

$$\langle u_{\lambda\mathbf{k}}|u_{\lambda'\mathbf{k}}\rangle = \delta_{\lambda\lambda'}, \tag{A.18}$$

which leads to*

$$\langle\psi_{\lambda\mathbf{k}}|\psi_{\lambda'\mathbf{k}'}\rangle = \int_{\text{all}} u^*_{\lambda\mathbf{k}} u_{\lambda'\mathbf{k}'} e^{i(\mathbf{k}'-\mathbf{k})\cdot\mathbf{r}} d\mathbf{r} = \sum_n^\infty e^{i(\mathbf{k}'-\mathbf{k})\cdot\mathbf{R}_n} \int_{\boldsymbol{\Omega}} u^*_{\lambda\mathbf{k}} u_{\lambda'\mathbf{k}'} e^{i(\mathbf{k}'-\mathbf{k})\cdot\mathbf{r}} d\mathbf{r}$$

$$= \frac{(2\pi)^3}{\boldsymbol{\Omega}} \delta(\mathbf{k}'-\mathbf{k}) \langle u_{\lambda\mathbf{k}}|u_{\lambda'\mathbf{k}'}\rangle = \frac{(2\pi)^3}{\boldsymbol{\Omega}} \delta(\mathbf{k}'-\mathbf{k})\delta_{\lambda\lambda'}. \tag{A.19}$$

---

*Actually, $\sum_n^\infty e^{i\mathbf{k}\cdot\mathbf{R}_n} = \dfrac{(2\pi)^3}{\boldsymbol{\Omega}} \sum_{\mathbf{G}} \delta(\mathbf{k}-\mathbf{G})$ (Appendix F, [1]). However, since we are considering only

$\mathbf{k}$ inside the BZ, it is rewritten $\sum_n^\infty e^{i\mathbf{k}\cdot\mathbf{R}_n} = \dfrac{(2\pi)^3}{\boldsymbol{\Omega}} \delta(\mathbf{k})$.

Appendix B

Electromagnetic gauge in quantum mechanics

From two of Maxwell's equations, an electromagnetic field $(\mathbf{E}, \mathbf{B})$ is represented by field and the gauge potentials, which are related by (in SI units)

$$
\begin{cases}
\boldsymbol{\nabla} \cdot \mathbf{B} = 0 \\
\boldsymbol{\nabla} \times \mathbf{E} = -\dfrac{\partial \mathbf{B}}{\partial t}
\end{cases}
\Rightarrow
\begin{cases}
\mathbf{B} \equiv \boldsymbol{\nabla} \times \mathbf{A} \\
\boldsymbol{\nabla} \times \mathbf{E} = -\boldsymbol{\nabla} \times \left(\dfrac{\partial \mathbf{A}}{\partial t} \right)
\end{cases}
\Rightarrow
\begin{cases}
\mathbf{B} \equiv \boldsymbol{\nabla} \times \mathbf{A} \\
\mathbf{E} = -\boldsymbol{\nabla}\phi - \dfrac{\partial \mathbf{A}}{\partial t}
\end{cases}
\tag{B.1}
$$

The Lagrangian of a charged particle in an electromagnetic field is

$$
\mathcal{L} = \frac{1}{2} m\dot{\mathbf{r}}^2 + q\dot{\mathbf{r}} \cdot \mathbf{A} - q\phi,
\tag{B.2}
$$

which correctly reproduces the Lorentz-force equation

$$
\frac{\mathrm{d}}{\mathrm{d}t} \frac{\partial \mathcal{L}}{\partial \dot{\mathbf{r}}} = \frac{\partial \mathcal{L}}{\partial \mathbf{r}}
\tag{B.3}
$$

$$
\Rightarrow \frac{\mathrm{d}}{\mathrm{d}t} \left(m\dot{\mathbf{r}} + q\mathbf{A} \right) = q \frac{\partial}{\partial \mathbf{r}} \left(\dot{\mathbf{r}} \cdot \mathbf{A} \right) - q \frac{\partial \phi}{\partial \mathbf{r}}
\tag{B.4}
$$

$$
\Rightarrow m\ddot{\mathbf{r}} + q \left[\frac{\partial \mathbf{A}}{\partial t} + \left(\frac{\partial \mathbf{r}}{\partial t} \cdot \frac{\partial}{\partial \mathbf{r}} \right) \mathbf{A} \right] = q \frac{\partial}{\partial \mathbf{r}} \left(\dot{\mathbf{r}} \cdot \mathbf{A} \right) - q \frac{\partial \phi}{\partial \mathbf{r}}
\tag{B.5}
$$

$$
\Rightarrow m\ddot{\mathbf{r}}_i + q \left[\frac{\partial \mathbf{A}_i}{\partial t} + \left(\frac{\partial \mathbf{r}_j}{\partial t} \frac{\partial}{\partial \mathbf{r}_j} \right) \mathbf{A}_i \right] = q \frac{\partial}{\partial \mathbf{r}_i} \left(\dot{\mathbf{r}}_j \mathbf{A}_j \right) - q \frac{\partial \phi}{\partial \mathbf{r}_i}
\tag{B.6}
$$

$$
\Rightarrow m\ddot{\mathbf{r}}_i = q \left(-\frac{\partial \phi}{\partial \mathbf{r}_i} - \frac{\partial \mathbf{A}_i}{\partial t} \right) + q \frac{\partial \mathbf{r}_j}{\partial t} \left(\frac{\partial \mathbf{A}_j}{\partial \mathbf{r}_i} - \frac{\partial \mathbf{A}_i}{\partial \mathbf{r}_j} \right)
\tag{B.7}
$$

$$
\Rightarrow m\ddot{\mathbf{r}}_i = q\mathbf{E}_i + q \left(\dot{\mathbf{r}} \times \mathbf{B} \right)_i.
\tag{B.8}
$$

Where we have used

$$
\frac{\mathrm{d}}{\mathrm{d}t} \mathbf{A} = \frac{\partial}{\partial t} \mathbf{A} + \left(\frac{\partial \mathbf{r}}{\partial t} \cdot \frac{\partial}{\partial \mathbf{r}} \right) \mathbf{A}
\tag{B.9}
$$

which is due to $\mathbf{A} = \mathbf{A}(\mathbf{r}(t), t)$ being the potential felt by a moving particle; and

$$(\dot{\mathbf{r}} \times \mathbf{B})_i = \epsilon_{ijk}\dot{\mathbf{r}}_j\mathbf{B}_k = \epsilon_{ijk}\epsilon_{mnk}\dot{\mathbf{r}}_j\frac{\partial}{\partial\dot{\mathbf{r}}_m}\mathbf{B}_n = (\delta_{im}\delta_{jn} - \delta_{in}\delta_{jm})\,\dot{\mathbf{r}}_j\frac{\partial}{\partial\dot{\mathbf{r}}_m}\mathbf{B}_n \tag{B.10}$$

$$= \dot{\mathbf{r}}_j\left(\frac{\partial}{\partial\dot{\mathbf{r}}_i}\mathbf{A}_j - \frac{\partial}{\partial\dot{\mathbf{r}}_j}\mathbf{A}_i\right). \tag{B.11}$$

By definition, the canonical momentum

$$\mathbf{p} \equiv \frac{\partial\mathcal{L}}{\partial\dot{\mathbf{r}}} = m\dot{\mathbf{r}} + q\mathbf{A}, \tag{B.12}$$

Then, the Hamiltonian

$$\mathcal{H} = \dot{\mathbf{r}}\mathbf{p} - \mathcal{L} = \frac{1}{2}m\dot{\mathbf{r}}^2 + q\phi = \frac{1}{2m}(\mathbf{p} - q\mathbf{A})^2 + q\phi. \tag{B.13}$$

While all of the above are classical notion, the Hamiltonian keeps the same structure when transferred into quantum mechanics, plus the canonical commutation $[\mathbf{r}, \mathbf{p}] = \sum_i [\mathbf{r}_i, \mathbf{p}_i] = 3i\hbar$ (that is, $\mathbf{p} = -i\hbar\boldsymbol{\nabla}_{\mathbf{r}}$).

B.1   Classical EM gauge freedom

It is known that for the same EM field can be represented by multiple potential, all of which are related by an Abelian gauge transformation

$$\begin{cases} \mathbf{A} \to \mathbf{A}' = \mathbf{A} + \boldsymbol{\nabla}\Lambda \\ \phi \to \phi' = \phi - \dfrac{\partial\Lambda}{\partial t} \end{cases} \tag{B.14}$$

, where $\Lambda = \Lambda(\mathbf{r}, t)$ is a differentiable function, which is sometimes called "generating function" or "gauge function".

There are some common gauge conditions that in this case or another can help simplify physical equations:

- Lorenz condition: $\boldsymbol{\nabla} \cdot \mathbf{A} + \dfrac{1}{c^2}\dfrac{\mathrm{d}\phi}{\mathrm{d}t} = 0$. This gauge is Lorentz covariant and leads to

$$\begin{cases} \Box\mathbf{A} = -\mu_0\mathbf{J} \\ \Box\phi = -\rho/\epsilon_0 \end{cases} , \quad \Box \equiv \boldsymbol{\nabla}^2 - \frac{1}{c^2}\frac{\partial^2}{\partial t^2}. \tag{B.15}$$

There still remains some gauge freedom in this condition, the generating function between Lorenz gauges satisfies $\Box\Lambda = 0$.

- Coulomb gauge: $\boldsymbol{\nabla} \cdot \mathbf{A} = 0$. The potential in this gauge are

$$
\begin{cases}
\Box \mathbf{A} = -\mu_0 \mathbf{J} + \dfrac{1}{c^2} \boldsymbol{\nabla} \dot{\phi}, \quad \mathbf{A}(\mathbf{r}, t) = \boldsymbol{\nabla} \times \displaystyle\int \dfrac{\mathbf{B}(\mathbf{r}', t)}{4\pi |\mathbf{r}' - \mathbf{r}|} d\mathbf{r}' \\[4mm]
\boldsymbol{\nabla}\phi = -\rho/\epsilon_0, \quad \phi(\mathbf{r}, t) = \displaystyle\int \dfrac{\rho(\mathbf{r}', t)}{4\pi\epsilon_0 |\mathbf{r}' - \mathbf{r}|} d\mathbf{r}'.
\end{cases}
\tag{B.16}
$$

The generating function between Coulomb gauges satisfies $\nabla^2 \Lambda = 0$. However, since there is only one bounded solution for this equation, $\Lambda = 0$, the Coulomb gauge is said to be complete.

B.2 EM gauge freedom in quantum mechanics

In quantum mechanics, to keep the Schrödinger equation

$$
i\hbar \frac{d\Psi(\mathbf{r}, t)}{dt} = H\Psi(\mathbf{r}, t) = \left[\frac{1}{2m} (\mathbf{p} - q\mathbf{A})^2 + q\phi \right] \Psi(\mathbf{r}, t)
\tag{B.17}
$$

covariant under EM gauges, the wave function must transform accordingly

$$
\Psi \to \Psi' = U(\Lambda)\Psi = e^{iq\Lambda/\hbar}\Psi.
\tag{B.18}
$$

That is, the intrinsic gauge-freedom in wave function's phase is connected with that of the EM potential.

The gauge covariance is verified after some algebra

$$
\begin{cases}
\left[i\hbar \dfrac{d}{dt}, U(\Lambda) \right] = -q\dot{\Lambda} U(\Lambda) \\[4mm]
[\mathbf{p}, U(\Lambda)] = [-i\hbar\boldsymbol{\nabla}, U(\Lambda)] = q\boldsymbol{\nabla}\Lambda
\end{cases}
\tag{B.19}
$$

$$
i\hbar \frac{d\Psi'}{dt} = H'\Psi = \left[\frac{1}{2m} (\mathbf{p} - q\mathbf{A}')^2 + q\phi' \right] \Psi'
\tag{B.20}
$$

$$
\Leftrightarrow i\hbar \frac{d}{dt} [U(\Lambda)\Psi] = \left[\frac{1}{2m} (\mathbf{p} - q\mathbf{A} - q\boldsymbol{\nabla}\Lambda)^2 + q\phi - q\dot{\Lambda} \right] U(\Lambda)\Psi
\tag{B.21}
$$

$$
\Leftrightarrow i\hbar U(\Lambda) \frac{d}{dt}\Psi - q\dot{\Lambda} U(\Lambda)\Psi = U(\Lambda)\left[\frac{1}{2m} (\mathbf{p} + q\boldsymbol{\nabla}\Lambda - q\mathbf{A} - q\boldsymbol{\nabla}\Lambda)^2 + q\phi - q\dot{\Lambda} \right] \Psi
\tag{B.22}
$$

$$
\Leftrightarrow i\hbar \frac{d}{dt}\Psi = \left[\frac{1}{2m} (\mathbf{p} - q\mathbf{A})^2 + q\phi \right] \Psi.
\tag{B.23}
$$

B.3 EM gauges for light-matter interaction

B.3.1 Velocity gauge

The velocity gauge is based on Coulomb gauge $\boldsymbol{\nabla}\cdot\mathbf{A} = 0$, along with some approximations.

- Long wavelength approximation: assuming the light field's wavelength is much larger and the length scale of the system. Hence, it is safe to ignore the spatial dependence $\mathbf{A}(\mathbf{r}, t) = \mathbf{A}(t)$.

- External field approximation: assuming the light field's source is far from the system, giving vanishing scalar potential $\phi = 0$.

Therefore, one particle Hamiltonian in the velocity gauge

$$
\begin{aligned}
H &= \frac{1}{2m}[\mathbf{p} - q\mathbf{A}]^2 + U(\mathbf{r}) \\
&= \frac{1}{2m}[\mathbf{p}^2 - 2q\mathbf{A}\cdot\mathbf{p} - i\hbar q\boldsymbol{\nabla}\cdot\mathbf{A} + q^2\mathbf{A}^2] + U(\mathbf{r}) \\
&= \frac{1}{2m}[\mathbf{p}^2 - 2q\mathbf{A}\cdot\mathbf{p} + q^2\mathbf{A}^2] + U(\mathbf{r}),
\end{aligned} \tag{B.24}
$$

where $U(\mathbf{r})$ is the periodic potential within the crystal.

B.3.2 Length gauge

From the velocity gauge defined above, implement the gauge transformation with $\Lambda = -\mathbf{r}\cdot\mathbf{A}$.

$$
\begin{cases}
\mathbf{A}' = \mathbf{A} - \boldsymbol{\nabla}(\mathbf{r}\cdot\mathbf{A}) \\
\phi' = \dfrac{\mathrm{d}(\mathbf{r}\cdot\mathbf{A})}{\mathrm{d}t} = \mathbf{r}\cdot\dot{\mathbf{A}}.
\end{cases} \tag{B.25}
$$

Note that

$$
\begin{aligned}
\boldsymbol{\nabla}(\mathbf{r}\cdot\mathbf{A}) &= (\mathbf{r}\cdot\boldsymbol{\nabla})\mathbf{A} + (\mathbf{A}\cdot\boldsymbol{\nabla})\mathbf{r} + \mathbf{r}\times(\boldsymbol{\nabla}\times\mathbf{A}) + \mathbf{A}\times(\boldsymbol{\nabla}\times\mathbf{r}) \\
&= (\mathbf{r}\cdot\boldsymbol{\nabla})\mathbf{A} + \mathbf{A} + \mathbf{r}\times\mathbf{B}
\end{aligned} \tag{B.26}
$$

$$
\boldsymbol{\nabla}_i(\mathbf{r}\cdot\mathbf{A}) = \mathbf{r}_j\partial_j\mathbf{A}_i + \mathbf{A}_i + \mathbf{r}_j\partial_i\mathbf{A}_j - \mathbf{r}_j\partial_j\mathbf{A}_i = \mathbf{A}_i + \mathbf{r}_j\partial_i\mathbf{A}_j \approx \mathbf{A}_i. \tag{B.27}
$$

The Hamiltonian in length gauge

$$
\begin{aligned}
H &= \frac{1}{2m}[\mathbf{p} - q(\mathbf{r}\cdot\boldsymbol{\nabla})\mathbf{A} - q\mathbf{r}\times\mathbf{B}]^2 + q\mathbf{r}\cdot\dot{\mathbf{A}} + U(\mathbf{r}) \\
&= \frac{1}{2m}[\mathbf{p} - q\mathbf{r}_j\partial_i\mathbf{A}_j\hat{\mathbf{r}}_i]^2 - q\mathbf{r}\cdot\mathbf{E} + U(\mathbf{r}) \\
&\approx \frac{\mathbf{p}^2}{2m} - q\mathbf{r}\cdot\mathbf{E} + U(\mathbf{r}).
\end{aligned} \tag{B.28}
$$

Appendix C

Some commutation relations

Here we apply the Heisenberg equation

$$\frac{d}{dt}\left\langle a_{\lambda\mathbf{k}}^{\dagger}a_{\lambda'\mathbf{k}}\right\rangle = \frac{-i}{\hbar}\left\langle\left[a_{\lambda\mathbf{k}}^{\dagger}a_{\lambda'\mathbf{k}},H\right]\right\rangle, \tag{C.1}$$

with the canonical commutation relation

$$\{a_{\lambda\mathbf{k}}^{\dagger}a_{\lambda'\mathbf{k}'}\} = \delta_{\lambda\lambda'}\delta_{\mathbf{k}\mathbf{k}'} \tag{C.2}$$

to derive intermediate steps for the SBE equation (2.17).

We have

$$\begin{aligned}
\left[a_{\lambda\mathbf{k}}^{\dagger}a_{\lambda'\mathbf{k}},a_{\lambda_1\mathbf{k}_1}^{\dagger}a_{\lambda_1\mathbf{k}_1}\right] &= a_{\lambda\mathbf{k}}^{\dagger}a_{\lambda_1\mathbf{k}_1}\delta_{\lambda'\lambda_1}\delta_{\mathbf{k}\mathbf{k}_1} - a_{\lambda\mathbf{k}}^{\dagger}a_{\lambda'\mathbf{k}}a_{\lambda_1\mathbf{k}_1}^{\dagger}a_{\lambda_1\mathbf{k}_1} \\
&\quad - a_{\lambda_1}^{\dagger}a_{\lambda'\mathbf{k}}\delta_{\lambda_1\lambda}\delta_{\mathbf{k}_1\mathbf{k}} + a_{\lambda_1\mathbf{k}_1}^{\dagger}a_{\lambda_1\mathbf{k}_1}a_{\lambda\mathbf{k}}^{\dagger}a_{\lambda'\mathbf{k}} \\
&= a_{\lambda\mathbf{k}}^{\dagger}a_{\lambda_1\mathbf{k}_1}\delta_{\lambda'\lambda_1}\delta_{\mathbf{k}\mathbf{k}_1} - a_{\lambda_1}^{\dagger}a_{\lambda'\mathbf{k}}\delta_{\lambda_1\lambda}\delta_{\mathbf{k}_1\mathbf{k}} \tag{C.3}
\end{aligned}$$

$$\begin{aligned}
\Rightarrow \left[a_{\lambda\mathbf{k}}^{\dagger}a_{\lambda'\mathbf{k}},H^0\right] &= \left[a_{\lambda\mathbf{k}}^{\dagger}a_{\lambda'\mathbf{k}},\sum_{\lambda_1\mathbf{k}_1}\varepsilon_{\lambda_1\mathbf{k}_1}a_{\lambda_1\mathbf{k}_1}^{\dagger}a_{\lambda_1\mathbf{k}_1}\right] \\
&= -(\varepsilon_{\lambda\mathbf{k}}-\varepsilon_{\lambda'\mathbf{k}})a_{\lambda\mathbf{k}}^{\dagger}a_{\lambda'\mathbf{k}}, \tag{C.4}
\end{aligned}$$

and

$$\begin{aligned}
\left[a_{\lambda\mathbf{k}}^{\dagger}a_{\lambda'\mathbf{k}},a_{\lambda_1\mathbf{k}_1}^{\dagger}\nabla_{\mathbf{k}_1}a_{\lambda_1\mathbf{k}_1}\right] &= \sum_{\mathbf{k}_2}\delta_{\mathbf{k}_2\mathbf{k}_1}\nabla_{\mathbf{k}_1}\left[a_{\lambda\mathbf{k}}^{\dagger}a_{\lambda'\mathbf{k}},a_{\lambda_1\mathbf{k}_2}^{\dagger}a_{\lambda_1\mathbf{k}_1}\right] \\
&= \sum_{\mathbf{k}_2}\delta_{\mathbf{k}_2\mathbf{k}_1}\nabla_{\mathbf{k}_1}\left(a_{\lambda\mathbf{k}}^{\dagger}a_{\lambda_1\mathbf{k}_1}\delta_{\lambda'\lambda_1}\delta_{\mathbf{k}\mathbf{k}_2} - a_{\lambda_1\mathbf{k}_2}^{\dagger}a_{\lambda'\mathbf{k}}\delta_{\lambda_1\lambda}\delta_{\mathbf{k}_1\mathbf{k}}\right) \\
&= a_{\lambda\mathbf{k}}^{\dagger}\nabla_{\mathbf{k}_1}\left(a_{\lambda_1\mathbf{k}_1}\right)\delta_{\lambda'\lambda_1}\delta_{\mathbf{k}\mathbf{k}_1} - a_{\lambda_1\mathbf{k}_1}^{\dagger}a_{\lambda'\mathbf{k}}\delta_{\lambda_1\lambda}\nabla_{\mathbf{k}_1}\left(\delta_{\mathbf{k}_1\mathbf{k}}\right) \\
&= a_{\lambda\mathbf{k}}^{\dagger}\nabla_{\mathbf{k}_1}\left(a_{\lambda_1\mathbf{k}_1}\right)\delta_{\lambda'\lambda_1}\delta_{\mathbf{k}\mathbf{k}_1} + \nabla_{\mathbf{k}_1}\left(a_{\lambda_1\mathbf{k}_1}^{\dagger}\right)a_{\lambda'\mathbf{k}}\delta_{\lambda_1\lambda}\delta_{\mathbf{k}_1\mathbf{k}} \tag{C.5}
\end{aligned}$$

$$\Rightarrow \left[a^\dagger_{\lambda\mathbf{k}} a_{\lambda'\mathbf{k}}, \sum_{\lambda_1 \mathbf{k}_1} a^\dagger_{\lambda_1 \mathbf{k}_1} \nabla_{\mathbf{k}_1} a_{\lambda_1 \mathbf{k}_1} \right] = a^\dagger_{\lambda\mathbf{k}} \nabla_{\mathbf{k}} \left(a_{\lambda'\mathbf{k}} \right) + \nabla_{\mathbf{k}} \left(a^\dagger_{\lambda\mathbf{k}} \right) a_{\lambda'\mathbf{k}} = \nabla_{\mathbf{k}} \left(a^\dagger_{\lambda\mathbf{k}} a_{\lambda'\mathbf{k}} \right), \quad (C.6)$$

where we should have used the continuous form for the commutator instead

$$\left\{ a^\dagger_{\lambda\mathbf{k}}, a_{\lambda'\mathbf{k}'} \right\} = \delta_{\lambda\lambda'} \frac{(2\pi)^3 \delta(\mathbf{k} - \mathbf{k}')}{\Omega}. \quad (C.7)$$

Next,

$$\left[a^\dagger_{\lambda\mathbf{k}} a_{\lambda'\mathbf{k}}, a^\dagger_{\lambda_1 \mathbf{k}_1} a_{\lambda_2 \mathbf{k}_1} \right] = a^\dagger_{\lambda\mathbf{k}} a_{\lambda_2 \mathbf{k}_1} \delta_{\lambda'\lambda_1} \delta_{\mathbf{k}\mathbf{k}_1} - a^\dagger_{\lambda_1 \mathbf{k}_1} a_{\lambda'\mathbf{k}} \delta_{\lambda_2 \lambda} \delta_{\mathbf{k}_1 \mathbf{k}}$$

$$\Rightarrow \left[a^\dagger_{\lambda\mathbf{k}} a_{\lambda'\mathbf{k}}, \sum_{\lambda_1 \lambda_2 \mathbf{k}_1} \boldsymbol{\xi}^{\mathbf{k}_1}_{\lambda_1 \lambda_2} a^\dagger_{\lambda_1 \mathbf{k}_1} a_{\lambda_2 \mathbf{k}_1} \right] = \sum_{\lambda_2} a^\dagger_{\lambda\mathbf{k}} a_{\lambda_2 \mathbf{k}} \boldsymbol{\xi}^{\mathbf{k}}_{\lambda'\lambda_2} - \sum_{\lambda_1} a^\dagger_{\lambda_1 \mathbf{k}} a_{\lambda'\mathbf{k}} \boldsymbol{\xi}^{\mathbf{k}}_{\lambda_1 \lambda}$$

$$= \sum_{\mu} \left(a^\dagger_{\lambda\mathbf{k}} a_{\mu\mathbf{k}} \boldsymbol{\xi}^{\mathbf{k}}_{\lambda'\mu} - a^\dagger_{\mu\mathbf{k}} a_{\lambda'\mathbf{k}} \boldsymbol{\xi}^{\mathbf{k}}_{\mu\lambda} \right) \quad (C.8)$$

Therefore,

$$\left[a^\dagger_{\lambda\mathbf{k}} a_{\lambda'\mathbf{k}}, H \right] = -\left(\varepsilon_{\lambda\mathbf{k}} - \varepsilon_{\lambda'\mathbf{k}} \right) a^\dagger_{\lambda\mathbf{k}} a_{\lambda'\mathbf{k}}$$

$$- e\mathbf{E}(t) \cdot i\nabla_{\mathbf{k}} \left(a^\dagger_{\lambda\mathbf{k}} a_{\lambda'\mathbf{k}} \right)$$

$$- e\mathbf{E}(t) \cdot \sum_{\mu} \left(a^\dagger_{\lambda\mathbf{k}} a_{\mu\mathbf{k}} \boldsymbol{\xi}^{\mathbf{k}}_{\lambda'\mu} - a^\dagger_{\mu\mathbf{k}} a_{\lambda'\mathbf{k}} \boldsymbol{\xi}^{\mathbf{k}}_{\mu\lambda} \right). \quad (C.9)$$

Appendix D

Explicit 30-band $\mathbf{k} \cdot \mathbf{p}$ Hamiltonian

Table D.1: The 30-band $\mathbf{k} \cdot \mathbf{p}$ parameters for GaAs, taken from [23]. The P parameters are converted to eV by $E_P = 2mP^2/\hbar^2$.

	E_{6v}	E_{7v}	E_{8v}	E_{6c}	E_{7c}	E_{8c}	E_{6u}	E_{3d}	E_{7d}	E_{8d}	E_{6q}
eV	-12.55	-0.314	0	1.519	4.488	4.569	8.56	10.17	11.89	11.89	13.64
	P	P_X	P_{3X}	P_{qX}	P_{vc}	P'	P_{sd}	P_{dc}	P_{3d}	P_{qd}	P_{uc}
eV	22.37	16.79	4.916	6.280	2.434	0.0656	0.010	4.344	8.888	23.15	19.63

Table D.2: Upper left corner of 30-band $\mathbf{k} \cdot \mathbf{p}$ Hamiltonian

$$
\begin{array}{c|cccccccccccccc}
 & |S_q\uparrow\rangle & |S_q\downarrow\rangle & |d_{3/2}\rangle & |d_{1/2}\rangle & |d_{-1/2}\rangle & |d_{-3/2}\rangle & |d'_{1/2}\rangle & |d'_{-1/2}\rangle & |D_z\uparrow\rangle & |D_z\uparrow\rangle & |D_x\uparrow\rangle & |D_x\uparrow\rangle & |S_u\uparrow\rangle & |S_u\downarrow\rangle \\
\hline
\langle S_q\uparrow| & E_q^k & 0 & -\sqrt{\tfrac{1}{2}}P_{qd}^+ & \sqrt{\tfrac{2}{3}}P_{qd}^z & \sqrt{\tfrac{1}{6}}P_{qd}^- & 0 & \sqrt{\tfrac{1}{3}}P_{qd}^z & \sqrt{\tfrac{1}{3}}P_{qd}^- & 0 & 0 & 0 & 0 & 0 & 0 \\
\langle S_q\downarrow| & & E_q^k & 0 & -\sqrt{\tfrac{1}{6}}P_{qd}^+ & \sqrt{\tfrac{2}{3}}P_{qd}^z & \sqrt{\tfrac{1}{2}}P_{qd}^- & \sqrt{\tfrac{1}{3}}P_{qd}^+ & -\sqrt{\tfrac{1}{3}}P_{qd}^z & 0 & 0 & 0 & 0 & 0 & 0 \\
\langle d_{3/2}| & & & E_{8d}^k & 0 & 0 & 0 & 0 & 0 & -\sqrt{\tfrac{1}{2}}P_{3d}^- & \tfrac{-\Delta'_{3d}}{2} & \sqrt{\tfrac{3}{2}}P_{3d}^+ & 0 & -\sqrt{\tfrac{1}{2}}P'^{-}_{ud} & 0 \\
\langle d_{1/2}| & & & & E_{8d}^k & 0 & 0 & 0 & 0 & -\sqrt{\tfrac{8}{3}}P_{3d}^z & -\sqrt{\tfrac{1}{6}}P_{3d}^- & \tfrac{-\Delta'_{3d}}{2} & \sqrt{\tfrac{1}{3}}P_{3d}^+ & \sqrt{\tfrac{2}{3}}P'^{z}_{ud} & \sqrt{\tfrac{1}{6}}P'^{-}_{ud} \\
\langle d_{-1/2}| & & & & & E_{8d}^k & 0 & 0 & 0 & \sqrt{\tfrac{1}{6}}P_{3d}^+ & -\sqrt{\tfrac{8}{3}}P_{3d}^z & -\sqrt{\tfrac{1}{2}}P_{3d}^- & \tfrac{\Delta'_{3d}}{2} & \sqrt{\tfrac{1}{6}}P'^{+}_{ud} & \sqrt{\tfrac{2}{3}}P'^{z}_{ud} \\
\langle d_{-3/2}| & & & & & & E_{8d}^k & 0 & 0 & \tfrac{\Delta'_{3d}}{2} & \sqrt{\tfrac{1}{2}}P_{3d}^+ & 0 & -\sqrt{\tfrac{3}{2}}P_{3d}^- & 0 & \sqrt{\tfrac{1}{2}}P'^{+}_{ud} \\
\langle d'_{1/2}| & & & & & & & E_{7d}^k & 0 & -\sqrt{\tfrac{4}{3}}P_{3d}^z & \sqrt{\tfrac{1}{3}}P_{3d}^- & 0 & -P_{3d}^+ & \sqrt{\tfrac{1}{3}}P'^{z}_{ud} & \sqrt{\tfrac{1}{3}}P'^{-}_{ud} \\
\langle d'_{-1/2}| & & & & & & & & E_{7d}^k & \sqrt{\tfrac{1}{3}}P_{3d}^+ & \sqrt{\tfrac{4}{3}}P_{3d}^z & -P_{3d}^- & 0 & \sqrt{\tfrac{1}{3}}P'^{+}_{ud} & -\sqrt{\tfrac{1}{3}}P'^{z}_{ud} \\
\langle D_z\uparrow| & & & & & & & & & E_3^k & 0 & 0 & 0 & 0 & 0 \\
\langle D_z\downarrow| & & & & & & & & & & E_3^k & 0 & 0 & 0 & 0 \\
\langle D_x\uparrow| & & & & & & & & & & & E_3^k & 0 & 0 & 0 \\
\langle D_x\downarrow| & & & & & & & & & & & & E_3^k & 0 & 0 \\
\langle S_u\uparrow| & & & & & & & & & & & & & E_u^k & 0 \\
\langle S_u\downarrow| & & & & & & & & & & & & & & E_u^k \\
\end{array}
$$

Table D.3: Upper right corner of 30-band $\mathbf{k}\cdot\mathbf{p}$ Hamiltonian

	$\lvert c_{3/2}\rangle$	$\lvert c_{1/2}\rangle$	$\lvert c_{-1/2}\rangle$	$\lvert c_{-3/2}\rangle$	$\lvert c'_{1/2}\rangle$	$\lvert c'_{-1/2}\rangle$	$\lvert S\uparrow\rangle$	$\lvert S\downarrow\rangle$	$\lvert v_{3/2}\rangle$	$\lvert v_{1/2}\rangle$	$\lvert v_{-1/2}\rangle$	$\lvert v_{-3/2}\rangle$	$\lvert v'_{1/2}\rangle$	$\lvert v'_{-1/2}\rangle$	$\lvert S_v\uparrow\rangle$	$\lvert S_v\downarrow\rangle$
$\langle S_q\uparrow\rvert$	$-\sqrt{\tfrac12}P'^+_{qc}$	$\sqrt{\tfrac23}P'^z_{qc}$	$\sqrt{\tfrac16}P'^-_{qc}$	0	$\sqrt{\tfrac13}P'^z_{qc}$	$\sqrt{\tfrac12}P'^-_{qc}$	0	0	$-\sqrt{\tfrac12}P^+_{qX}$	$\sqrt{\tfrac23}P^z_{qX}$	$\sqrt{\tfrac16}P^-_{qX}$	0	$\sqrt{\tfrac13}P^z_{qX}$	$\sqrt{\tfrac13}P^-_{qX}$	0	0
$\langle S_q\downarrow\rvert$	0	$-\sqrt{\tfrac16}P'^+_{qc}$	$\sqrt{\tfrac23}P'^z_{qc}$	$\sqrt{\tfrac12}P'^-_{qc}$	$\sqrt{\tfrac13}P'^+_{qc}$	$-\sqrt{\tfrac13}P'^z_{qc}$	0	0	0	$-\sqrt{\tfrac16}P^+_{qX}$	$\sqrt{\tfrac23}P^z_{qX}$	$\sqrt{\tfrac12}P^-_{qX}$	$\sqrt{\tfrac13}P^+_{qX}$	$-\sqrt{\tfrac13}P^z_{qX}$	0	0
$\langle d_{3/2}\rvert$	$\tfrac{\Delta'_{dc}}{3}$	$\sqrt{\tfrac13}P'^+_{dc}$	$\sqrt{\tfrac13}P'^z_{dc}$	0	$\sqrt{\tfrac16}P'^+_{dc}$	$\sqrt{\tfrac23}P'^z_{dc}$	$-\sqrt{\tfrac12}P^-_{sd}$	0	$\tfrac{\Delta_{dZ}}{3}$	$\sqrt{\tfrac13}P'^+_{dZ}$	$\sqrt{\tfrac13}P'^z_{dZ}$	0	$\sqrt{\tfrac16}P^+_{dZ}$	$\sqrt{\tfrac23}P^z_{dZ}$	$-\sqrt{\tfrac12}P'^-_{vd}$	0
$\langle d_{1/2}\rvert$	$-\sqrt{\tfrac13}P'^-_{dc}$	$\tfrac{\Delta'_{dc}}{3}$	0	$\sqrt{\tfrac13}P'^z_{dc}$	0	$-\sqrt{\tfrac12}P'^+_{dc}$	$\sqrt{\tfrac23}P^z_{sd}$	$-\sqrt{\tfrac16}P^-_{sd}$	$-\sqrt{\tfrac13}P^-_{dZ}$	$\tfrac{\Delta_{dZ}}{3}$	0	$\sqrt{\tfrac13}P'^z_{dZ}$	0	$-\sqrt{\tfrac12}P^+_{dZ}$	$\sqrt{\tfrac23}P'^z_{vd}$	$-\sqrt{\tfrac16}P'^-_{vd}$
$\langle d_{-1/2}\rvert$	$-\sqrt{\tfrac13}P'^z_{dc}$	0	$\tfrac{\Delta'_{dc}}{3}$	$-\sqrt{\tfrac13}P'^+_{dc}$	$\sqrt{\tfrac12}P'^-_{dc}$	0	$\sqrt{\tfrac16}P^+_{sd}$	$-\sqrt{\tfrac23}P^z_{sd}$	$-\sqrt{\tfrac13}P'^z_{dZ}$	0	$\tfrac{\Delta_{dZ}}{3}$	$-\sqrt{\tfrac13}P'^+_{dZ}$	$\sqrt{\tfrac12}P^-_{dZ}$	0	$\sqrt{\tfrac16}P'^+_{vd}$	$-\sqrt{\tfrac23}P'^z_{vd}$
$\langle d_{-3/2}\rvert$	0	$-\sqrt{\tfrac13}P'^z_{dc}$	$\sqrt{\tfrac13}P'^-_{dc}$	$\tfrac{\Delta'_{dc}}{3}$	$\sqrt{\tfrac23}P'^z_{dc}$	$-\sqrt{\tfrac16}P'^-_{dc}$	0	$\sqrt{\tfrac12}P^+_{sd}$	0	$-\sqrt{\tfrac13}P'^z_{dZ}$	$\sqrt{\tfrac13}P'^-_{dZ}$	$\tfrac{\Delta_{dZ}}{3}$	$\sqrt{\tfrac23}P^z_{dZ}$	$-\sqrt{\tfrac16}P^-_{dZ}$	0	$\sqrt{\tfrac12}P'^+_{vd}$
$\langle d'_{1/2}\rvert$	$-\sqrt{\tfrac13}P'^-_{dc}$	0	$-\sqrt{\tfrac12}P'^+_{dc}$	$-\sqrt{\tfrac23}P'^z_{dc}$	$-\tfrac{2\Delta'_{dc}}{3}$	0	$\sqrt{\tfrac13}P^z_{sd}$	$\sqrt{\tfrac13}P^z_{sd}$	$-\sqrt{\tfrac16}P'^-_{dZ}$	0	$-\sqrt{\tfrac12}P'^+_{dZ}$	$-\sqrt{\tfrac23}P'^z_{dZ}$	$-\tfrac{2\Delta_{dZ}}{3}$	0	$\sqrt{\tfrac13}P'^z_{vd}$	$\sqrt{\tfrac13}P'^z_{vd}$
$\langle d'_{-1/2}\rvert$	$-\sqrt{\tfrac23}P'^z_{dc}$	$-\sqrt{\tfrac12}P'^-_{dc}$	0	$\sqrt{\tfrac16}P'^+_{dc}$	0	$-\tfrac{2\Delta'_{dc}}{3}$	$\sqrt{\tfrac13}P^+_{sd}$	$-\sqrt{\tfrac23}P^z_{sd}$	$-\sqrt{\tfrac23}P'^z_{dZ}$	$-\sqrt{\tfrac12}P'^-_{dZ}$	0	$\sqrt{\tfrac16}P'^+_{dZ}$	0	$-\tfrac{2\Delta_{dZ}}{3}$	$\sqrt{\tfrac13}P'^+_{vd}$	$-\sqrt{\tfrac23}P'^z_{vd}$
$\langle D_z\uparrow\rvert$	$-\sqrt{\tfrac12}P'^+_{3c}$	$-\sqrt{\tfrac83}P^z_{dc}$	$-\sqrt{\tfrac83}P^z_{dc}$	$-\tfrac{\Delta'_{3c}}{2}$	$-\sqrt{\tfrac43}P^z_{dc}$	$\sqrt{\tfrac13}P'^-_{dc}$	0	0	$-\sqrt{\tfrac12}P^+_{3X}$	$-\sqrt{\tfrac83}P^z_{3X}$	$-\sqrt{\tfrac83}P^z_{3X}$	$-\tfrac{\Delta_{3X}}{2}$	$-\sqrt{\tfrac43}P^z_{3X}$	$\sqrt{\tfrac13}P^-_{3X}$	0	0
$\langle D_z\downarrow\rvert$	$-\tfrac{\Delta'_{3c}}{2}$	$-\tfrac{\Delta'_{3c}}{2}$	$\tfrac{\Delta'_{3c}}{2}$	$\sqrt{\tfrac12}P'^-_{3c}$	$\sqrt{\tfrac13}P'^+_{dc}$	$\sqrt{\tfrac43}P'^z_{dc}$	0	0	$-\tfrac{\Delta_{3X}}{2}$	$-\tfrac{\Delta_{3X}}{2}$	$\tfrac{\Delta_{3X}}{2}$	$\sqrt{\tfrac12}P'^-_{3X}$	$\sqrt{\tfrac13}P^+_{3X}$	$\sqrt{\tfrac43}P^z_{3X}$	0	0
$\langle D_x\uparrow\rvert$	$\sqrt{\tfrac32}P'^-_{dc}$	$\sqrt{\tfrac12}P'^-_{dc}$	$-\sqrt{\tfrac12}P'^-_{dc}$	0	0	$-P'^+_{dc}$	0	0	$\sqrt{\tfrac32}P^-_{3X}$	$\sqrt{\tfrac12}P'^-_{3X}$	$-\sqrt{\tfrac12}P'^-_{3X}$	0	0	$-P^+_{3X}$	0	0
$\langle D_x\downarrow\rvert$	0	0	0	$-\sqrt{\tfrac32}P'^+_{dc}$	$-P'^-_{dc}$	0	0	0	0	0	0	$-\sqrt{\tfrac32}P'^+_{3X}$	$-P^-_{3X}$	0	0	0
$\langle S_u\uparrow\rvert$	$-\sqrt{\tfrac12}P'^+_{uc}$	$\sqrt{\tfrac23}P^z_{uc}$	$\sqrt{\tfrac16}P'^-_{uc}$	0	$\sqrt{\tfrac13}P'^z_{uc}$	$\sqrt{\tfrac12}P'^-_{uc}$	0	0	$-\sqrt{\tfrac12}P'^+_{uX}$	$\sqrt{\tfrac23}P^z_{uX}$	$\sqrt{\tfrac16}P^-_{uX}$	0	$\sqrt{\tfrac13}P^z_{uX}$	$\sqrt{\tfrac13}P^z_{uX}$	0	0
$\langle S_u\downarrow\rvert$	0	$-\sqrt{\tfrac16}P'^+_{uc}$	$\sqrt{\tfrac23}P^z_{uc}$	$\sqrt{\tfrac12}P'^-_{uc}$	$\sqrt{\tfrac16}P'^+_{uc}$	$-\sqrt{\tfrac16}P^z_{uc}$	0	0	0	$-\sqrt{\tfrac16}P'^+_{uX}$	$\sqrt{\tfrac23}P^z_{uX}$	$\sqrt{\tfrac12}P^-_{uX}$	$\sqrt{\tfrac13}P^+_{uX}$	$-\sqrt{\tfrac13}P^z_{uX}$	0	0

47

Table D.4: Lower right corner of 30-band $\mathbf{k}\cdot\mathbf{p}$ Hamiltonian

	$\lvert c_{3/2}\rangle$	$\lvert c_{1/2}\rangle$	$\lvert c_{-1/2}\rangle$	$\lvert c_{-3/2}\rangle$	$\lvert c'_{1/2}\rangle$	$\lvert c'_{-1/2}\rangle$	$\lvert S\!\uparrow\rangle$	$\lvert S\!\downarrow\rangle$	$\lvert v_{3/2}\rangle$	$\lvert v_{1/2}\rangle$	$\lvert v_{-1/2}\rangle$	$\lvert v_{-3/2}\rangle$	$\lvert v'_{1/2}\rangle$	$\lvert v'_{-1/2}\rangle$	$\lvert S_v\!\uparrow\rangle$	$\lvert S_v\!\downarrow\rangle$
$\langle c_{3/2}\rvert$	E^{k}_{8c}	0	0	0	0	0	$-\sqrt{\tfrac{1}{2}}P'^{-}$	0	$\tfrac{\Delta'}{3}$	$\sqrt{\tfrac{1}{3}}P^{+}_{X}$	$\sqrt{\tfrac{1}{3}}P^{z}_{X}$	0	$\sqrt{\tfrac{1}{6}}P^{+}_{X}$	$\sqrt{\tfrac{2}{3}}P^{z}_{X}$	$-\sqrt{\tfrac{1}{2}}P'^{-}_{vc}$	0
$\langle c_{1/2}\rvert$		E^{k}_{8c}	0	0	0	0	$\sqrt{\tfrac{2}{3}}P'^{z}$	$-\sqrt{\tfrac{1}{6}}P'^{-}$	$-\sqrt{\tfrac{1}{3}}P^{-}_{X}$	$\tfrac{\Delta'}{3}$	0	$\sqrt{\tfrac{1}{3}}P^{z}_{X}$	0	$-\sqrt{\tfrac{1}{2}}P^{+}_{X}$	$\sqrt{\tfrac{2}{3}}P^{z}_{vc}$	$-\sqrt{\tfrac{1}{6}}P^{-}_{vc}$
$\langle c_{-1/2}\rvert$			E^{k}_{8c}	0	0	0	$\sqrt{\tfrac{1}{6}}P'^{+}$	$\sqrt{\tfrac{2}{3}}P'^{z}$	$-\sqrt{\tfrac{1}{3}}P^{z}_{X}$	0	$\tfrac{\Delta'}{3}$	$-\sqrt{\tfrac{1}{3}}P^{+}_{X}$	$\sqrt{\tfrac{1}{2}}P^{z}_{X}$	0	$\sqrt{\tfrac{1}{6}}P^{+}_{vc}$	$\sqrt{\tfrac{2}{3}}P^{z}_{vc}$
$\langle c_{-3/2}\rvert$				E^{k}_{8c}	0	0	0	$\sqrt{\tfrac{1}{2}}P'^{+}$	0	$-\sqrt{\tfrac{1}{3}}P^{z}_{X}$	$-\sqrt{\tfrac{1}{3}}P^{+}_{X}$	$\tfrac{\Delta'}{3}$	$\sqrt{\tfrac{2}{3}}P^{z}_{X}$	$-\sqrt{\tfrac{1}{6}}P^{-}_{X}$	0	$\sqrt{\tfrac{1}{2}}P^{-}_{vc}$
$\langle c'_{1/2}\rvert$					E^{k}_{7c}	0	$\sqrt{\tfrac{1}{3}}P'^{z}$	$-\sqrt{\tfrac{1}{3}}P'^{-}$	$-\sqrt{\tfrac{1}{6}}P^{-}_{X}$	$\sqrt{\tfrac{1}{2}}P^{z}_{X}$	$\sqrt{\tfrac{1}{6}}P^{+}_{X}$	$\sqrt{\tfrac{2}{3}}P^{z}_{X}$	$-\tfrac{2\Delta'}{3}$	0	$\sqrt{\tfrac{1}{3}}P^{z}_{vc}$	$-\sqrt{\tfrac{1}{3}}P^{z}_{vc}$
$\langle c'_{-1/2}\rvert$						E^{k}_{7c}	$\sqrt{\tfrac{1}{3}}P'^{+}$	$\sqrt{\tfrac{1}{3}}P'^{z}$	$-\sqrt{\tfrac{2}{3}}P^{z}_{X}$	$-\sqrt{\tfrac{1}{6}}P^{-}_{X}$	$\sqrt{\tfrac{1}{2}}P^{z}_{X}$	$\sqrt{\tfrac{1}{6}}P^{+}_{X}$	0	$-\tfrac{2\Delta'}{3}$	$\sqrt{\tfrac{1}{3}}P^{+}_{vc}$	$\sqrt{\tfrac{1}{3}}P^{-}_{vc}$
$\langle S\!\uparrow\rvert$							E^{k}_{6c}	0	$-\sqrt{\tfrac{1}{2}}P^{-}$	$\sqrt{\tfrac{2}{3}}P^{z}$	$\sqrt{\tfrac{1}{6}}P^{+}$	0	$\sqrt{\tfrac{1}{3}}P^{z}$	$-\sqrt{\tfrac{1}{3}}P^{-}$	0	0
$\langle S\!\downarrow\rvert$								E^{k}_{6c}	0	$\sqrt{\tfrac{1}{6}}P^{-}$	$\sqrt{\tfrac{2}{3}}P^{z}$	$\sqrt{\tfrac{1}{2}}P^{+}$	$\sqrt{\tfrac{1}{3}}P^{+}$	$-\sqrt{\tfrac{1}{3}}P^{z}$	0	0
$\langle v_{3/2}\rvert$									E^{k}_{8v}	0	0	0	0	0	0	$-\sqrt{\tfrac{1}{6}}P'^{-}_{vX}$
$\langle v_{1/2}\rvert$										E^{k}_{8v}	0	0	0	0	$\sqrt{\tfrac{2}{3}}P'^{z}_{vX}$	$\sqrt{\tfrac{2}{3}}P'^{z}_{vX}$
$\langle v_{-1/2}\rvert$											E^{k}_{8v}	0	0	0	$\sqrt{\tfrac{1}{6}}P'^{+}_{vX}$	$\sqrt{\tfrac{1}{2}}P'^{+}_{vX}$
$\langle v_{-3/2}\rvert$												E^{k}_{8v}	0	0	0	$-\sqrt{\tfrac{1}{3}}P'^{z}_{vX}$
$\langle v'_{1/2}\rvert$													E^{k}_{7v}	0	$\sqrt{\tfrac{1}{3}}P'^{z}_{vX}$	0
$\langle v'_{-1/2}\rvert$														E^{k}_{7v}	$\sqrt{\tfrac{1}{3}}P'^{+}_{vX}$	$-\sqrt{\tfrac{1}{3}}P'^{z}_{vX}$
$\langle S_v\!\uparrow\rvert$															E^{k}_{6v}	0
$\langle S_v\!\downarrow\rvert$																E^{k}_{6v}

48

Appendix E

Supplemental figures

E.1 Dipole matrix elements
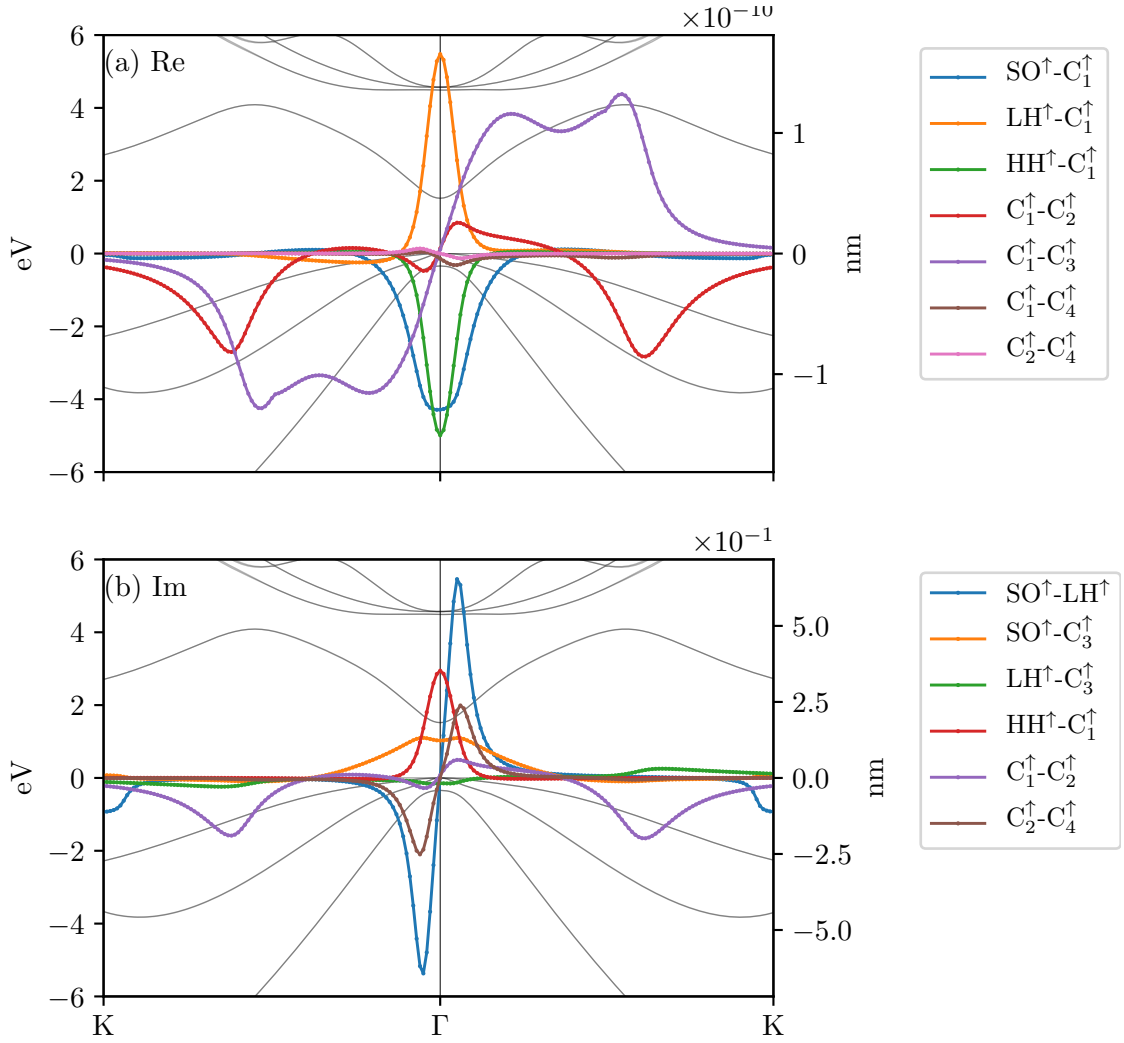
Figure E.1: Important matrix elements of $\boldsymbol{\xi}^{\mathbf{k}}_{\lambda\lambda'}$ in ΓK direction that were used to solve the SBE in section 3.1.1. (a) and (b) are respectively the real and imaginary part.
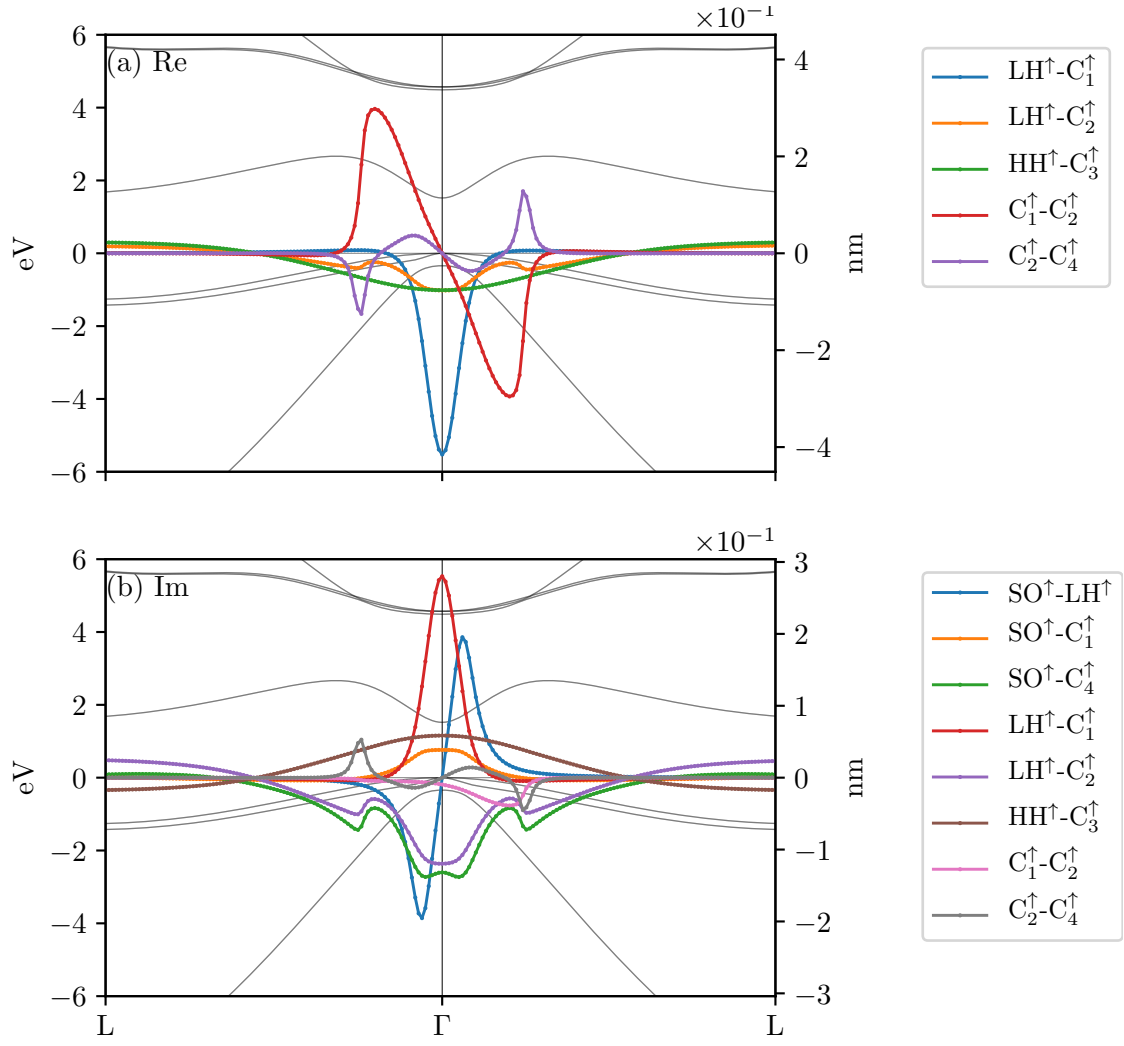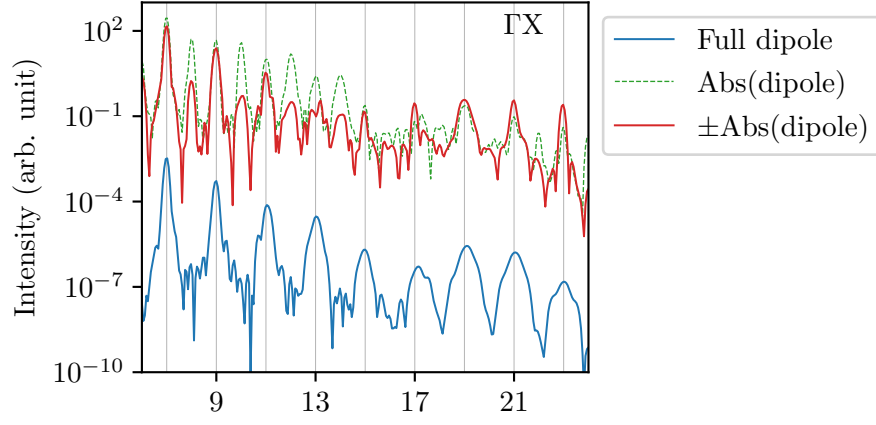
Figure E.2: Important matrix elements of $\boldsymbol{\xi}^{\mathbf{k}}_{\lambda\lambda'}$ in ΓL direction that were used to solve the SBE in section 3.1.1. (a) and (b) are respectively the real and imaginary part.

E.2 Using only dipole's amplitude

Figure E.3: The HHG signal calculated with and without transition dipole's phase in direction ΓX, similar to figure 3.6.
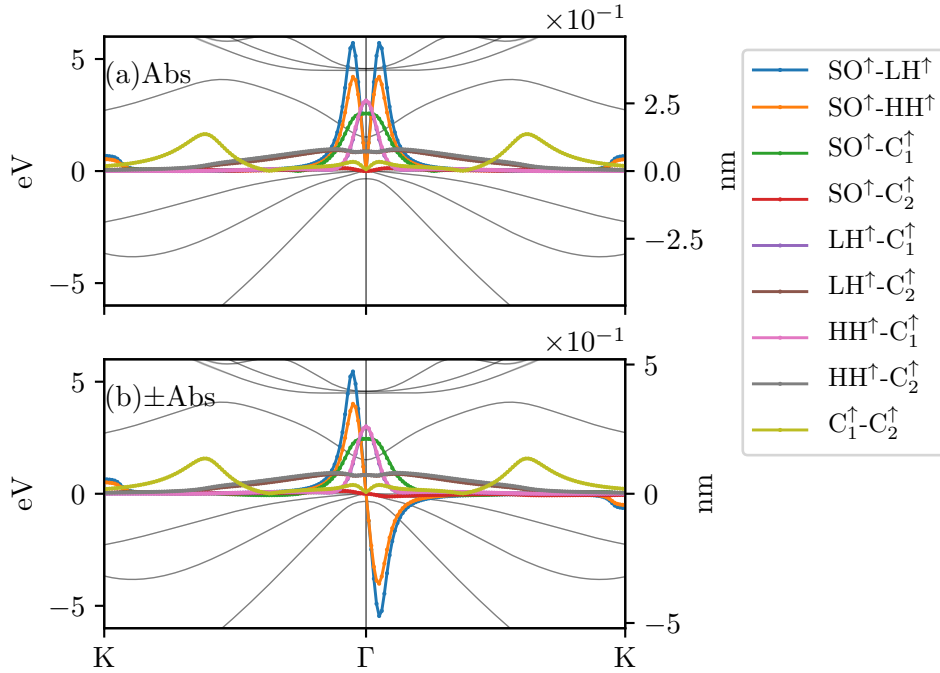

Figure E.4: The transition dipole's matrix elements used to calculate the spectra in figure 3.6. (a) was calculated via formula (2.39). (b) is similar to (a) but with a smoothing procedure: starting from the BZ's left boundary, if $\xi_{\lambda\lambda'}^{\mathbf{k}}$'s derivative jumps over a certain threshold, invert the signs of $\xi_{\lambda\lambda'}^{\mathbf{k}}$ on the right.

E.3 A nicer fit to experiment

The 30-band $\mathbf{k} \cdot \mathbf{p}$ model for GaAs uses only one parameter to describe the lack of inversion symmetry - P'. On the one hand, this makes it very easy to perform a switch-off analysis. However, by the model's own author, the fitted value for P' was by far too small compared with previous $\mathbf{k} \cdot \mathbf{p}$ methods. Specifically, $E_{P'} = 0.065\text{eV}$, while it is of 2.36, 6 or 11 eV elsewhere.[*]

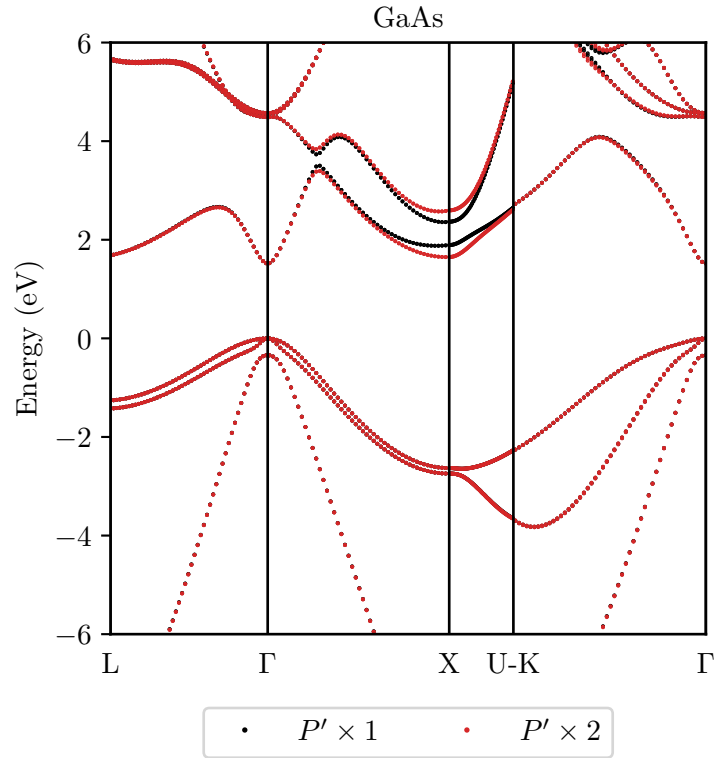
[*] $E_{P'} = 2mP'^2/\hbar^2$

Figure E.5: GaAs's band structures before and after P' is modified. The latter gives better fit to the HHG experiment.

With such deficiencies, it's worthwhile to try modifying the P' to give a better fit to the HHG experiment [30] (figure 3.5). By increase it by a factor of 2, the matching is excellent, without much alteration to the band structure, especially in the investigated directions.
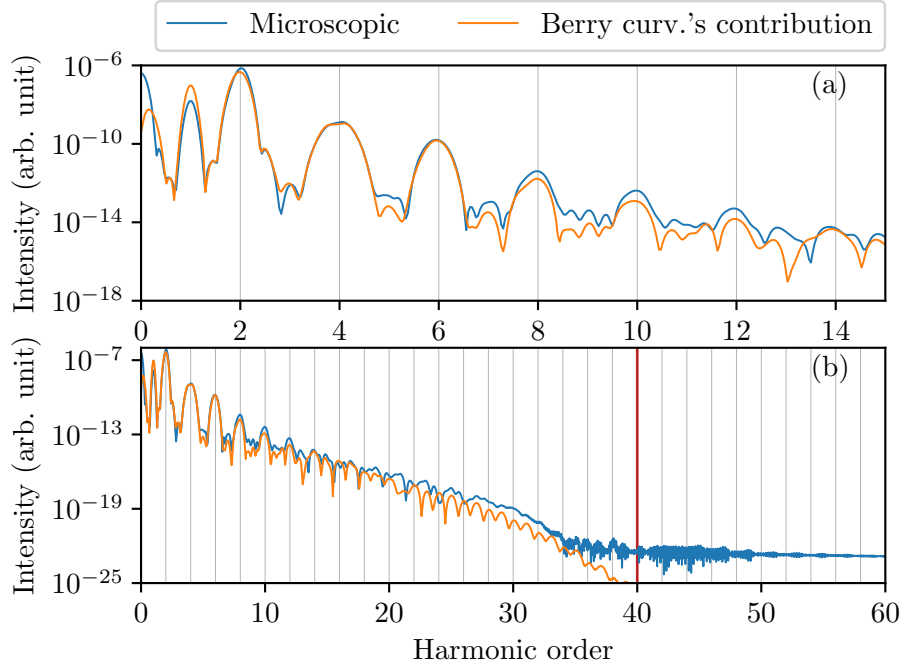
E.4 Transverse HHG

Figure E.6: The same as figure 3.7, but with C_3 and C_4 bands removed to reduce transition with small energies, and driving field strength reduced by half, to magnify interband transitions. The temporal profile is given in figure E.7.
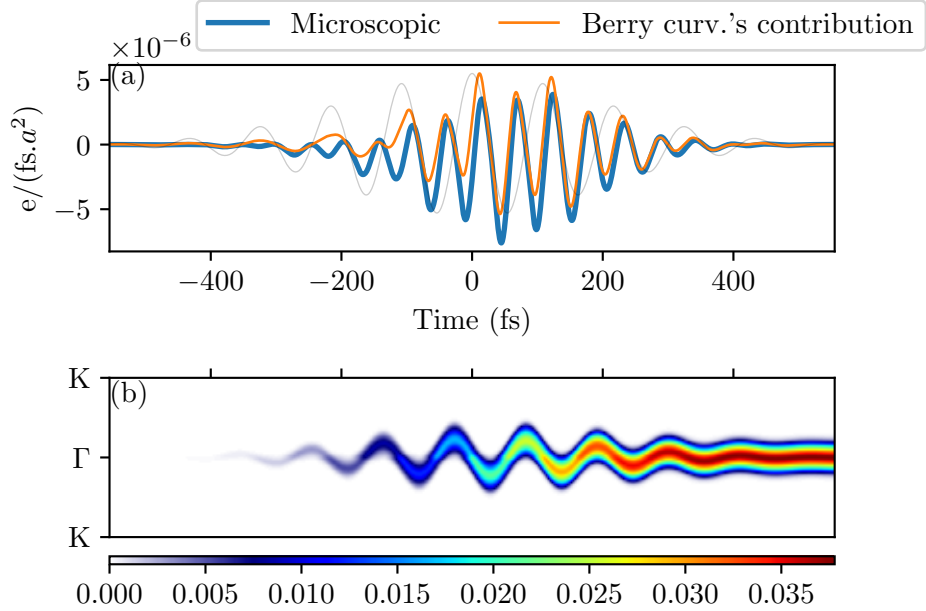

Figure E.7: The same as figure 3.8, but with C_3 and C_4 bands removed to reduce transition with small energies, and driving field strength reduced by half, to magnify interband transitions. The spectral profile is given in figure E.6.
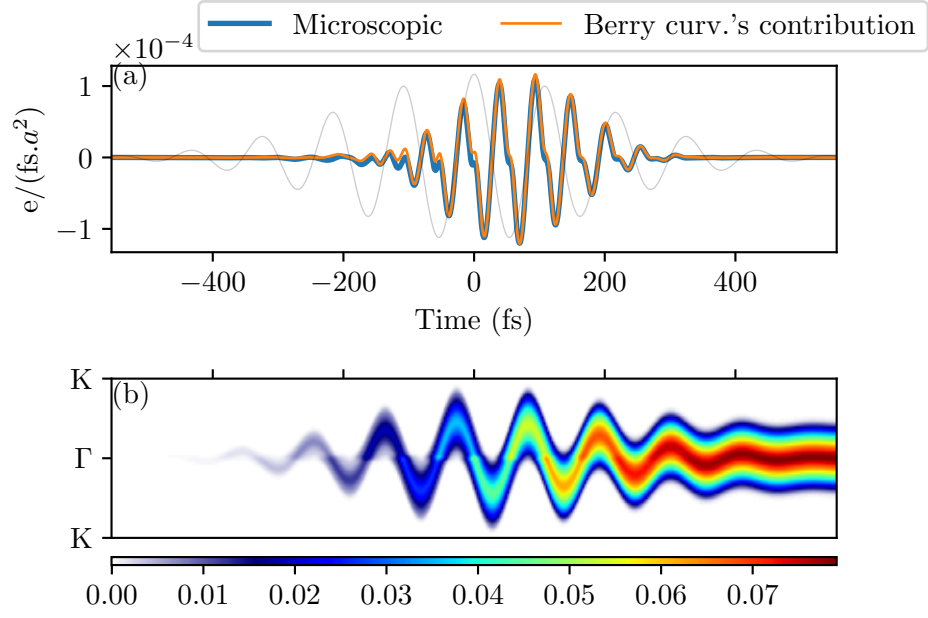
Figure E.8: The same as figure 3.8, but with C_3 and C_4 bands removed to reduce transition with small energies. This is the temporal profile for figure 3.9.

Bibliography

Books

[1]   N. Ashcroft and N. Mermin. *Solid State Physics*. HRW international editions. Holt, Rinehart and Winston, 1976.

[2]   R. W. Boyd. *Nonlinear optics*. 3rd ed. Amsterdam ; Boston: Academic Press, 2008.

[3]   G. Fishman. *Semi-conducteurs les bases de la théorie k.p*. Palaiseau: Éd. de l'École polytechnique, 2010.

[4]   D. Griffiths. *Introduction to quantum mechanics*. Upper Saddle River, NJ: Pearson Prentice Hall, 2005.

[5]   D. Griffiths. *Introduction to electrodynamics*. Boston: Pearson, 2013.

[6]   H. Haug and S. W. Koch. *Quantum theory of the optical and electronic properties of semiconductors*. 4th ed. Singapore ; River Edge, NJ: World Scientific, 2004.

[7]   J. J. Sakurai and J. Napolitano. *Modern Quantum Mechanics:* 2nd ed. Cambridge University Press, 2017.

[8]   D. Vanderbilt. *Berry Phases in Electronic Structure Theory*. Cambridge University Press, 2018.

[9]   P. Y. Yu and M. Cardona. *Fundamentals of semiconductors: physics and materials properties*. 4th ed. Graduate texts in physics. Berlin ; New York: Springer, 2010.

Articles

[10]   P. C. Becker et al. "Femtosecond Photon Echoes from Band-to-Band Transitions in GaAs". In: Phys. Rev. Lett. **61** (14 1988), 1647–1649.

[11]   J. S. Blakemore. "Semiconducting and other major properties of gallium arsenide". In: Journal of Applied Physics **53**.10 (1982), R123–R181.

[12]   M. Cardona and F. H. Pollak. "Energy-Band Structure of Germanium and Silicon: The k·p Method". In: Phys. Rev. **142** (2 1966), 530–543.

[13]   S. Ghimire and D. A. Reis. "High-harmonic generation from solids". en. In: Nature Physics **15**.1 (2019), 10–16.

[14] S. Ghimire et al. "Observation of high-order harmonic generation in a bulk crystal". en. In: Nature Physics **7**.2 (2011), 138–141.

[15] L. E. Golub and E. L. Ivchenko. "Shift photocurrent induced by two-quantum transitions". en. In: Journal of Experimental and Theoretical Physics **112**.1 (2011), 152–159.

[16] M. Gradhand et al. "First-principle calculations of the Berry curvature of Bloch states for charge and spin transport of electrons". In: Journal of Physics: Condensed Matter **24**.21 (2012), 213202.

[17] M. Hohenleutner et al. "Real-time observation of interfering crystal electrons in high-harmonic generation". en. In: Nature **523**.7562 (2015), 572–575.

[18] U. Huttner, M. Kira, and S. W. Koch. "Ultrahigh Off-Resonant Field Effects in Semiconductors". In: Laser & Photonics Reviews **11**.4 (2017), 1700049.

[19] S. Jiang et al. "Role of the Transition Dipole Amplitude and Phase on the Generation of Odd and Even High-Order Harmonics in Crystals". In: Phys. Rev. Lett. **120** (25 2018), 253201.

[20] H. Liu et al. "High-harmonic generation from an atomically thin semiconductor". en. In: Nature Physics **13**.3 (2017), 262–265.

[21] T. T. Luu and H. J. Wörner. "High-order harmonic generation in solids: A unifying approach". In: Phys. Rev. B **94** (11 2016), 115164.

[22] T. T. Luu and H. J. Wörner. "Measurement of the Berry curvature of solids using high-harmonic spectroscopy". en. In: Nature Communications **9**.1 (2018), 1–6.

[23] S. Richard, F. Aniel, and G. Fishman. "Energy-band structure of Ge, Si, and GaAs: A thirty-band $\mathbf{k} \cdot \mathbf{p}$ method". In: Phys. Rev. B **70** (23 2004), 235204.

[24] O. Schubert et al. "Sub-cycle control of terahertz high-harmonic generation by dynamical Bloch oscillations". en. In: Nature Photonics **8**.2 (2014), 119–123.

[25] J. Sjakste et al. "Energy relaxation mechanism of hot-electron ensembles in GaAs: Theoretical and experimental study of its temperature dependence". In: Phys. Rev. B **97** (6 2018), 064302.

[26] G. Sundaram and Q. Niu. "Wave-packet dynamics in slowly perturbed crystals: Gradient corrections and Berry-phase effects". In: Phys. Rev. B **59** (23 1999), 14915–14925.

[27] G. Vampa et al. "Linking high harmonics from gases and solids". en. In: Nature **522**.7557 (2015), 462–464.

[28] K. S. Virk and J. E. Sipe. "Semiconductor optics in length gauge: A general numerical approach". In: Phys. Rev. B **76** (3 2007), 035213.

[29] Q. T. Vu et al. "Light-Induced Gaps in Semiconductor Band-to-Band Transitions". In: Phys. Rev. Lett. **92** (21 2004), 217403.

[30] P. Xia et al. "Nonlinear propagation effects in high harmonic generation in reflection and transmission from gallium arsenide". en. In: Optics Express **26**.22 (2018), 29393.

[31] D. Xiao, M.-C. Chang, and Q. Niu. "Berry phase effects on electronic properties". In: Rev. Mod. Phys. **82** (3 2010), 1959–2007.

[32] C. Yu, S. Jiang, and R. Lu. "High order harmonic generation in solids: a review on recent numerical methods". en. In: Advances in Physics: X **4**.1 (2019), 1562982.